# HLA-E and NKG2A Mediate Resistance to *M. bovis* BCG Immunotherapy in Non-Muscle-Invasive Bladder Cancer

D. Ranti[1,2,3,4,5*], H. Yu[1,2,3,4,5,11*], Y.A. Wang[1,2,3,4,5], C. Bieber[1,2,3,4,5], T. Strandgaard[6,7], B. Salomé[1,2,3,4], Sean Houghton[8], J. Kim[8], H. Ravichandran[8], I. Okulate[1,2,3,4,5], E. Merritt[3,9], S. Bang[9], A. Demetriou[1,2,3,4,5], Z. Li[1,2,3,4], S. V. Lindskrog[6,7], D.F. Ruan[1,2,3,4], J. Daza[1,2,3,4,5], R. Rai[4], E. Hegewisch-Solloa[10], E.M. Mace[10], R., Fernandez-Rodriguez[2,4], S. Izadmehr[3,9], G. Doherty[11,12], A. Narasimhan[11,12], A.M. Farkas[3,4,11], P. Cruz-Encarnacion[1,2], S. Shroff[7,13], F. Patel[3,14], M. Tran[3,4,11], S.J. Park[1,2,3,4], J. Qi[15], M. Patel[15], D. Geanon[15], G. Kelly[15], R.M.de Real[15], B. Lee[15], K. Nie[15], S. Miake-Iye[15], K. Angeliadis[15], E. Radkevich[15], T.H. Thin[16], M. Garcia-Barros[16], H. Brown[16], B. Martin[16], A. Mateo[16], A. Soto[16], R. Sussman[16], S. Shiwlani[16], S. Francisco-Simon[16], K.G. Beaumont[9,13], Y. Hu[15], Y-C. Wang[7,13], L. Wang[9], R.P. Sebra[9,13,17], S. Smith[18], M. Skobe[2,4], E. Clancy-Thompson[19], D. Palmer[19], S. Hammond[19], B. D. Hopkins[15], P. Wiklund[5], J. Zhu[9,13], J.J. Bravo-Cordero[11,12], R. Brody[16], Hopkins, B., Z. Chen[1,3,15], S. Kim-Schulze[1,3,15], L. Dyrskjøt[6,7], O. Elemento[8], A. Tocheva[3,9], W-M. Song[9], N. Bhardwaj[3,4,11], M.D. Galsky[4,11], J.P. Sfakianos[5#] & A. Horowitz[1,2,3,4#]

[1]Department of Immunology and Immunotherapy, Icahn School of Medicine at Mount Sinai, New York, NY, USA
[2]Department of Oncological Sciences, Icahn School of Medicine at Mount Sinai, New York, NY, USA
[3]The Marc and Jennifer Lipschultz Precision Immunology Institute, Icahn School of Medicine at Mount Sinai, New York, NY, USA
[4]Tisch Cancer Institute, Icahn School of Medicine at Mount Sinai, New York, NY, USA
[5]Department of Urology, Icahn School of Medicine at Mount Sinai, New York, NY, USA
[6]Department of Molecular Medicine, Aarhus University Hospital, Aarhus, Denmark
[7]Department of Clinical Medicine, Aarhus University, Aarhus, Denmark
[8]Caryl and Israel Englander Institute for Precision Medicine, Weill Cornell Medicine, New York, NY, USA
[9]Department of Genetics and Genomic Sciences, Icahn School of Medicine at Mount Sinai, New York, NY, USA
[10]Department of Pediatrics, Vagelos College of Physicians and Surgeons, Columbia University, New York NY, USA
[11]Division of Hematology and Medical Oncology, Department of Medicine, Icahn School of Medicine at Mount Sinai, New York, NY, USA
[12]Microscopy and Advanced Bioimaging Core, Icahn School of Medicine at Mount Sinai, New York, NY, USA
[13]Icahn Institute for Data Science and Genomics Technology, Icahn School of Medicine at Mount Sinai, New York, NY, USA
[14]Department of Microbiology, Icahn School of Medicine at Mount Sinai, New York, NY, USA
[15]Human Immune Monitoring Center, Icahn School of Medicine at Mount Sinai, New York, NY, USA
[16]Department of Pathology, Molecular and Cell-Based Medicine, Icahn School of Medicine at Mount Sinai, New York, NY
[17]Black Family Stem Cell Institute, Icahn School of Medicine at Mount Sinai, New York, NY, USA
[18]Center for Inflammation research and Translational Medicine, Brunel University London, London, UK
[19]AstraZeneca, Oncology R & D Unit, Gaithersburg, Maryland, USA
[20]Department of Physiology and Biophysics, Weill Cornell Medicine, New York, NY, USA
* These authors contributed equally
# Co-Senior author

**Running title.** HLA-E and NKG2A in BCG Resistance

**Keywords.** Non-muscle-invasive bladder cancer; BCG-unresponsive; NK cells; Immunotherapy.

**Corresponding Author:**
Amir Horowitz, PhD
Associate Professor of Immunology & Immunotherapy and Oncological Sciences
Lipschultz Precision Immunology Institute and Tisch Cancer Institute
Icahn School of Medicine at Mount Sinai
1425 Madison Ave., Box 1630
New York, New York 10029
Tel: (212) 659-9391 | Fax: (646) 537-9577
Email: amir.horowitz@mssm.edu

John P. Sfakianos, MD
Associate Professor of Urology
Icahn School of Medicine at Mount Sinai
1425 Madison Ave., L6-58, Box 1272
New York, New York 10029
Tel: (212) 659-9375
Email: john.sfakianos@mountsinai.org

**Conflict of Interest Disclosure Statement:** The authors declare no potential conflicts of interest.

**Word Count (excluding methods and references):**
**Fig. Count: 7**
**Table Count: 1**

**Abstract:**

*Mycobacterium bovis* Bacillus Calmette-Guerin (BCG) is the primary treatment for non-muscle-invasive bladder cancer (NMIBC), known to stimulate inflammatory cytokines, notably interferon (IFN)-γ. We observed that prolonged IFN-γ exposure fosters adaptive resistance in recurrent tumors, aiding immune evasion and tumor proliferation. We identify HLA-E and NKG2A, part of a novel NK and T cell checkpoint pathway, as key mediators of resistance in BCG-unresponsive NMIBC. IFN-γ enhances HLA-E and PD-L1 expression in recurrent tumors, with an enrichment of intra-tumoral NKG2A-expressing NK and CD8 T cells. $CXCL9^{+}$ macrophages and dendritic cells and CXCL12-expressing stromal cells likely recruit CXCR3/CXCR4-expressing NK and T cells and $CXCR7^{+}$ HLA-$E^{HIGH}$ tumor cells. NK and CD8 T cells remain functional within BCG-unresponsive tumors but are inhibited by HLA-E and PD-L1, providing a framework for combined NKG2A and PD-L1 blockade strategy for bladder-sparing treatment of BCG-unresponsive NMIBC.

## Introduction

Intravesical *Mycobacterium bovis* Bacillus Calmette-Guerin (BCG) is the only FDA-approved, first-line treatment for high risk non-muscle-invasive bladder cancer (NMIBC), and is hypothesized to act in part via the release of inflammatory cytokines, notably interferon (IFN)-γ [1].Unfortunately, tumor recurrence following BCG treatment is common, with local recurrence rates between 32.6 to 42.1% and progression rates between 9.5 to 13.4% [2]. Radical cystectomy is the only definitive treatment option for BCG-unresponsive disease, leaving patients at high risk for complications and the need for urinary diversion which can lead to diminished quality of life [3,4]. Currently, there is substantial interest and numerous ongoing clinical trials to identify novel therapeutic options for BCG-unresponsive NMIBC.

Despite the use of BCG as the first-line immunotherapy for NMIBC for over 40 years, the mechanisms underlying resistance to BCG's therapeutic benefits are poorly understood. This lack of understanding has further hindered progress in developing novel approaches to treat tumors resistant to BCG. The six-dose weekly induction regimen was devised anecdotally based on rudimentary urine studies performed in the 1970's [5]. Only a single dosing study has ever been performed to assess the immunologic response with this dosing regimen, which concluded that six doses stimulated an immune response, but did not investigate the ramifications of the magnitude nor the duration of that immune response [6]. Contributing to the difficulty in predicting BCG response is the variety of immune lineages implicated in both its success and failure, including neutrophils, monocytes, macrophages, dendritic cells (DCs), T cells, and natural killer (NK) cells [7].

Adaptive immune resistance, in which cancers are recognized by immune cells, but accommodative changes prevent effective clearance, is an important mechanism of therapeutic resistance [8]. IFN-γ has been shown to have both pro- and anti-tumorigenic functions across an array of tumor types[9]. The equilibrium established by IFN-γ signaling may be critical in preventing therapeutic resistance. In melanoma and lung cancer, dysfunctional and overactive IFN-γ signaling is known to drive T cell inhibition via upregulation of PD-L1 [10]. In muscle-invasive and metastatic urothelial carcinoma, IFN-γ associates with improved as well as poor responses to PD-1/PD-L1 blockade and exists as part of a balance (coined 2IR score) between pro- and anti-tumorigenic pathways expressed in the TME [11]. The impact of long-term intravesical BCG, which drives chronic immune stimulation via IFN-γ production, and its role in immune dysregulation and exhaustion in BCG unresponsive NMIBC is emerging but still unclear [12,13].

Previous work comparing BCG-unresponsive to treatment-naïve tumors showed a significant increase in PD-L1 expression, but only in a minority of unresponsive samples [14]. Immunotherapeutic strategies, especially those engaging the PD-1/PD-L1 axis to unleash exhausted immune cells, have

142 modestly improved NMIBC treatment. Unfortunately, response rates to PD-1 blockade monotherapies in
143 NMIBC remain low, at ~19% durable response [15,16,17,18]. Further, PD-L1 expression levels alone have failed
144 to accurately predict response to immunotherapy in NMIBC, suggesting that alternative mechanisms of
145 immune suppression are engaged [19].

146 The HLA-E/NKG2A axis has been identified as a potent immune checkpoint regulating both CD8
147 T and NK cells [20,21,22,23,24]. Abrogation of HLA-E interactions with NKG2A on NK cells increased effector
148 activity against tumor cells and potentiated anti-tumor function. Further, blocking NKG2A on CD8 T cells
149 in a murine model increased tumor vaccine response, even in a PD-1 resistant setting [20,22]. Additionally, the
150 combination of anti-NKG2A antibody (monalizumab) and antiPD-L1 antibody (durvalumab) has been
151 studied in a Phase 2 clinical trial in patients with nonresectable, stage III NSCLC. The combination
152 demonstrated an objective response rate of 35% vs 17.9% with durvalumab alone, as well as improved
153 progression-free survival (PFS) with durvalumab and monalizumab (72.7%) compared to durvalumab alone
154 (33.9%) [25].

155 Most recently, BCG was shown to directly infect a proportion of bladder tumor cells in NMIBC
156 patients driving impairment in autophagy flux resulting in downregulation of HLA class I expression along
157 with a shift towards epithelial-to-mesenchymal transitioning (EMT) by BCG-infected tumor cells [26]. In a
158 cohort of BCG-treated NMIBC patients with tumor recurrence, the authors observed that abundance of
159 class I HLA-negative tumor cells associated with disease progression and metastasis and overall survival.
160 This study highlighted two different tumor cell types within BCG-unresponsive settings and suggested that
161 a tumor phenotype defined by high HLA class I expression correlated with improved long-term survival
162 post-cystectomy.

163 In this study, we confirm the presence of both tumor cell phenotypes but focus on their interactions
164 with stromal and immune cells. We present a novel mechanism of resistance, whereby HLA class I-positive
165 tumor cells are activated in response to NK and CD8 T cell-derived IFN-γ and recruited to CXCL12-
166 expressing stromal-rich regions of the tumor where myeloid cells, regulatory T cells (Tregs), and immune
167 effector cells (NK, CD8 T cells) are enriched. Consequently, class I HLA-negative tumor cells can subvert
168 immune cell trafficking. We pose a novel hypothesis that BCG more broadly induces changes in the bladder
169 tumor microenvironment (TME), promoting expression of NKG2A and PD-1 on $CD8^+$ T cells, NKG2A on
170 NK cells, and HLA-E, PD-L1, and CXCR7 on recurring, cytokine-activated tumor cells, and these
171 phenotypic changes are mechanistically linked to treatment resistance and immune evasion by recurring
172 tumors. This study investigates HLA-E and NKG2A as a novel axis of resistance induced by chronic
173 inflammation and provides a mechanistic framework for a bladder-sparing combination immunotherapy
174 strategy of NKG2A and PD-L1 blockade for overcoming resistance to BCG immunotherapy for treating
175 high-grade NMIBC.

176

177 **Results**

178

179 **Clinical cohort description.**

180 Cohort descriptions of patient samples used for the experiments below are described in Table 1.
181 Patient samples were collected and processed at The Mount Sinai Hospital, and the validation cohort was
182 collected and processed at Aarhus University Hospital, Denmark. Median patient age ranged from 64 to
183 70.7 years old; median months to recurrence ranged from 1.7 to 2.9 months; median months to progression
184 ranged from 4.43 to 23.28 (**Table 1**).

185

186 **IFN-γ initiates adaptive resistance including increased tumor expression of HLA-E and PD-L1.**

187 To investigate potential mechanisms underlying BCG resistance in NMIBC, we used tumor
188 specimens from BCG-naïve patients, prior to initiating induction intravesical BCG therapy and BCG-
189 unresponsive tumors, with a recurrence after at least an induction course of intravesical BCG, collected
190 from a prospective cohort of NMIBC patients. Targeted *in situ* hybridization and *mRNA* sequencing and
191 gene-set enrichment analysis (GSEA) comparing BCG-unresponsive tumors to pre-treatment timepoints
192 were performed (**Fig. 1A***)* [27]. Significant gene sets are shown ranked by their normalized enrichment score
193 (NES) (**Fig. 1A**, **Supplemental Table S1***)*. The top enriched gene-sets comparing BCG-unresponsive to
194 BCG-naïve tumors (n=36) included, but were not limited to, IFN-γ response, cytotoxic lymphocytes, T cell
195 checkpoint modulation, tumor inflammation, TH1 response, and lymphocyte trafficking (**Supplemental**
196 **Table S1**). Of note, the "Lymphocyte trafficking" pathway was largely driven by a combination of genes
197 encoding activating cytokines and receptors as well as inhibitory immune checkpoint genes (*PDCD1* (PD-
198 1), *CD274* (PD-L1), *PDCD1LG2* (PD-L2), *CTLA4*, *TIGIT, KLRC1* (NKG2A), *HLA-E*) indicating a balance
199 between antitumor and pro-tumorigenic features in the TME. Gene sets downregulated in the BCG-
200 unresponsive state and upregulated in the BCG naïve state included TGF beta signaling, hypoxia,
201 peroxisome, oxidative phosphorylation, P53 pathway, DNA repair, and stress toxicity (**Fig. 1A**).

202 To better understand the inflammatory state observed in BCG-unresponsive tumors, we used cell-
203 free urine supernatants from a prospective cohort of BCG-treated NMIBC patients and performed an
204 analysis using the OLINK Proteomics™ "inflammation" panel, a 92-analyte protein proximity extension
205 assay, to profile urine cytokines reflective of the urothelial microenvironment [28, 29]. Independent of clinical
206 response to BCG therapy, all patients experienced elevated cytokine levels in their urine. Significantly
207 upregulated cytokines of interest at the sixth dose compared with the BCG-naïve state included IFN-γ,
208 Flt3L, IL2RB, CCL8, CCL13, CCL19, CCL23, CXCL1, CXCL9, CXCL10, CXCL11, and TWEAK (**Fig.**

209 **1B**; all $p<0.05$). Importantly, urine cytokine levels kept increasing with each consecutive dose of BCG,
210 where even after a six-week treatment interruption (time of first cystoscopy,) urine cytokine levels never
211 equilibrated back to baseline, although the differences were not significant. The inflammatory signature
212 was validated in an independent cohort, "Aarhus" (Aarhus University Hospital, Denmark), consisting of
213 BCG-treated patients with long term clinical follow-up. Urine samples from 66 patients were collected at
214 the BCG-naïve time point and compared to patient-matched urine samples collected within four months
215 after completion of BCG induction course. CXCL9, CXCL10, CXCL11, CCL19, and CCL23 had lasting
216 upregulation at the post-BCG timepoint ($p < 0.05$) (**Fig. 1C**). Additionally, urinary protein profiles at these
217 timepoints were compared between responsive and unresponsive patients considering whether visible
218 bladder tumors were present at the time of urine sampling (**Fig. 1D**). With exception of CXCL5, when
219 assessing urine from BCG-unresponsive patients (before the start of BCG induction therapy) we identified
220 significantly elevated levels of cytokines and chemokines only when tumors were present at time of
221 sampling, where the presence of CCL3, CCL20, CXCL11, IL-8, MMP7 and MMP12 were attributable to
222 bladder tumors rather than in response to BCG. Patients unresponsive to BCG showed a distinct urinary
223 protein profile after BCG treatment with a greater magnitude of inflammatory cytokine and chemokine
224 production as well as Caspase-8 (a marker of apoptosis) and TGF-β1 in its pre-processed inactive state
225 interacting with its latency associated peptide (LAP) (**Fig. 1D**).
226 To better understand the effects of IFN-γ on recurring bladder tumors, primary tumor cells from
227 NMIBC patients (n=10) and urothelial tumor lines were cultured for 24 hours in the presence or absence of
228 recombinant human IFN-γ (**Fig. 1E**) and HLA-E and PD-L1 expression were measured via fluorescence
229 flow cytometry. Tumor cells expressed significantly higher levels of PD-L1 and HLA-E following
230 stimulation with IFN-γ, which was also observed across the collection of bladder tumor lines (n=11) **(Fig.**
231 **1E)**. We saw no effects of IFN-γ on wild type (WT) K562 tumors (lack expression of HLA class I, including
232 HLA-E). HLA-E-stably–transduced K562 cells were used as a positive control for maximal HLA-E
233 expression. Overall, these results suggest adaptive resistance by recurring tumor cells after BCG therapy
234 that respond to IFN-γ by increasing HLA-E and PD-L1 expression and in a microenvironment replete with
235 immune effector cells.
236
237 **Selective upregulation of tumor HLA-E in regions near NKG2A-expressing NK and CD8 T cells**
238 To validate *in situ* hybridization *mRNA* analyses and to better understand the spatial relationship
239 between tumor cells and tumor infiltrating lymphocytes (TILs), we performed multiplex imaging analyses
240 using both immunofluorescence (IF) as well as immunohistochemistry (IHC) with whole slide scanning for
241 targeted high-resolution analyses on a cohort BCG naïve (N=17) and BCG unresponsive (N=24) NMIBC
242 patients (**Fig. 2**). We first performed a subset analysis of NMIBC sections (N=4) using a PhenoCycler™

243 (formerly CODEX) imaging system (Akoya Biosciences). Representative imaging for one BCG-
244 unresponsive NMIBC section highlights S100A4$^{+}$ tumor cells intermixed with stroma (Vimentin) (**Fig.**
245 **2A**). We observed a large abundance of NKp46$^{+}$ NK cells and CD8 T cells with variegated expression of
246 NKG2A and/or PD-1 (**Figs. 2B** and **2C**). While the analysis was underpowered for robust analyses, the data
247 demonstrated substantially greater abundance of NKG2A-expressing NK and CD8 T cells in BCG-
248 unresponsive sections and in regions of tumor tissue with high HLA-E expression by tumor cells and
249 stroma.
250 To validate the observation, we stained the cohort of 41 NMIBC sections by multiplexed IHC for Pan-
251 cytokeratin (pan-CK), HLA-E, CD3, and NKG2A (**Fig. 2D**). Among tumors from the cohort, we analyzed
252 840,348 tumor cells in total (277,315 for BCG-naïve and 563,033 for BCG-unresponsive). We used Halo
253 digital pathology software (Indica Labs, Albuquerque, NM) to annotate cell lineages, and to measure tumor
254 HLA-E expression within the for density and spatial relationships with stromal and T/NK cell infiltration
255 and proximity (**Fig. 2E-2I**). Here, we confirmed that HLA-E$^{BRIGHT}$ tumor cells were significantly more
256 abundant in BCG-unresponsive tumors (p= 0.0002) and represented 43.6%% of total tumor cells compared
257 to 10.3% in BCG-naïve tumors (**Fig. 2G**). Further, we identified NKG2A$^{+}$ CD3$^{-}$ NK cells and NKG2A$^{+}$
258 CD3$^{+}$ T cells (**Fig. 2H**) and determined they were in significantly closer proximity to HLA-E$^{BRIGHT}$ tumor
259 cells (p<0.00001)(**Fig. 2I**). Finally, we performed a proximity ligation assay by immunofluorescence using
260 antibodies targeting HLA-E and NKG2A to quantify the numbers of interactions between NKG2A$^{+}$
261 NK/CD8 T cells and HLA-E$^{+}$ tumor cells and found a significantly greater number of interactions in BCG-
262 unresponsive tumors (p = 0.009) (**Fig. 2J** and **2K**).
263
264 **Chronic activation of tumor-infiltrating NK and CD8 T cells in BCG-unresponsive tumors**
265 To better understand the composition of the tumor microenvironment and to characterize the
266 potential drivers of adaptive resistance, single-cell RNA sequencing (scRNA-seq) of nine tumors (BCG-
267 naïve (n=3) and unresponsive (n=6)), was performed. In total, 65,324 tumor-derived cells containing 26,520
268 gene features passed quality control and were used for subsequent analyses, with a median of 958 genes
269 detected per cell.
270 Twenty-two identifiable cell populations, including CD4 and CD8A T cells, regulatory T cells
271 (Tregs), NK cells, dendritic cells (DCs), monocytes and macrophages, granulocytes, B cells, plasma cells,
272 and nonhematopoietic stromal, and tumor cells were identified after graph-based clustering (**Fig. 3A** and
273 **3B**, **Supplementary Table S3 and S4**). To identify the cell origin(s) of IFN-γ and related pro-inflammatory
274 gene signatures, we examined the expression of *IFNG* in each of the cell populations. NK cells, CD8 T
275 cells, and a subset comprised of both CD4 and CD8 T cells defined by cell cycle genes (T cell-cycle)
276 demonstrated the highest levels of *IFNG* expression among all cell clusters and had distinct IFN-γ$^{high}$ cell

277 populations (**Extended data Fig. S1A).** Additionally, we profiled the median gene expression across all
278 major canonical checkpoint receptors and observed variegated expression on T cell subsets. However,
279 tumor-derived NK cells mostly expressed *KLRC1*, and to a lesser extent *HAVCR2* (Tim3) and *TIGIT*
280 (**Extended data Fig. S1B).**

281 To better understand the functional significance associated with NKG2A expression, we stratified
282 NK cells, CD8 T and T cell-cycle cells by low and high *KLRC1* expression and performed a differential
283 expression of genes (DEG) analysis (**Fig. 3C**). Our analysis revealed a balance between cytokine and
284 cytolytic activity and expression of inhibitory checkpoint receptors. *KLRC1*$^{high}$ NK cells expressed
285 significantly higher CCL5, CSF1, *XCL2,* IL2RB, and *FCER1G*, but additionally expressed higher levels of
286 *TIGIT*. Tumor-infiltrating NK cells also expressed significantly higher levels of *CD2*, *ITGA1* (CD49a),
287 *ITGAE* (CD103) and *RGS1* suggesting they are tissue-resident. Additionally, we observed that *KLRC1*$^{high}$
288 CD8 T cells expressed elevated levels of CCL3, CSF1, *GNLY*, *GZMA*, *GZMB*, and *PRF1* (perforin), but
289 they additionally expressed higher levels of *CTLA4, ENTPD1* (CD39), *HAVCR2*, *LAG3*, *KIR2DL4* and
290 *TIGIT*. *KLRC1*$^{high}$ T cell-cycle cells showed significant upregulation in *CCL5, CSF1, CXCL13, NKG7,*
291 *GNLY*, *GZMA*, *GZMB*, but additionally expressed *LAG3*, *KIR2DL4,* and *TIGIT*. Collectively, the data
292 suggest that BCG therapy drives strong immune activation and that many repeated doses of treatment
293 sustain activation over prolonged period driving upregulation of inhibitory checkpoint pathways.
294

295 **Functionally distinct states of bladder tumor-derived NK and CD8 T cells in BCG-unresponsive**
296 **NMIBC**

297 NK cells are very heterogenous and remain poorly described in solid tumors with virtually nothing
298 known in human bladder cancer. We performed unbiased clustering on all NK cells to derive five major
299 clusters (**Fig. 3D**), which were divided across conventional definitions of CD56$^{bright}$ and CD56$^{dim}$ NK cells
300 (**Fig. 3E**). A pathway analysis revealed significant enrichment in CD56$^{bright}$ NK cells for genes involved in
301 metabolism, IL-2 signaling, and immune 'stress' (ROS and DNA repair) (**Fig. 3F**). Conversely, CD56$^{dim}$
302 NK cell enriched pathways included response to TNFα and IFNα and apoptosis, MAPK activity but also
303 reflect immune 'stress' (hypoxia, complement regulation). Building on two recent seminal resources for
304 transcriptional reference mapping of human NK cells in solid tissues[30, 31], we integrated the newly defined
305 gene signatures to annotate 'functional states' to bladder tumor-derived NK cells (**Fig. 3G**, **Extended data**
306 **Fig. S2**). Our analysis confirmed that clusters 1 and 2 are very similar to Group 2 typical CD56$^{bright}$ NK
307 cells, and cluster 5 strongly correlates with Group 1 "stressed" CD56$^{bright}$ NK cells, described by Netskar
308 et al.[30]. Collectively clusters 1,2, and 5 reflecting Groups 1 and 2 NK cells represent ~50% of the total
309 tumor-infiltrating NK cells. Additionally, the remaining fraction of CD56$^{dim}$ NK cells were distributed

among groups 3-6 NK cells, defined by effector functions (Gr. 3), adaptive NKG2C$^{+}$ NK cells (Gr. 4), activated (Gr. 5), and typical (Gr. 6) NK cells.

We similarly applied gene signatures for NK1, NK2, and NK3 subsets as recently demonstrated by Rebuffet et al[31, 32], and these definitions more closely reflect a developmental or ontogeny trajectory of NK cells across human tissues, NK1 and NK-intermediate cells represent immature CD56$^{bright}$ NK cells and NK3 cells include terminally mature and adaptive NK cells (**Extended data Fig. S2**). Our comparative analysis revealed an enrichment of NK-intermediate cells representing the original clusters 1 and 2, and NK1B cells representing the original clusters 3 and 4. Both NK1B and NK-intermediate signatures were shared among the original cluster 5 suggesting transitional properties of this NK cell subset. Finally, we profiled tumor-infiltrating NK cells according to the six functional states (Gr. 1-6) (and CD8 T cells and T cell-cycle cells according to KLRC1$^{+/-}$) for expression of tissue residency genes as well as cytokines/chemokines and cytokine/chemokine receptors to understand how NK cells and T cells are trafficking to the bladder, and we confirmed they are functionally competent (**Fig. 3H** and **3I**). We also observed clear evidence suggesting functional specialization within the NK cells and within the T cells. For instance, *KLRC1*$^{+}$ CD8 T cells express high levels of *IL2RB, TNFRFS9* (4-1BB), *CSF1 and FASLG* compared to their *KLRC1*$^{-}$ counterparts. However, *KLRC1*$^{-}$ CD8 T cells expressed higher levels of *IFNG*, and *FLT3LG* (**Fig. 3I**).

**BCG-unresponsive tumors are characterized by a segregated microenvironment, where activated HLA-E$^{HIGH}$ tumor cells are recruited to stromal regions replete with immune cells**.

We next sought to understand the composition of tumor cells in tumors from both treatment-naïve (N=14,852) and BCG-unresponsive (N=29,858) NMIBC patients. UMAP clustering of scRNAseq analysis revealed seven major subsets of tumor cells (**Fig. 4A**), where clusters B1 and B3 had significantly higher HLA-E expression (**Fig. 4B**) and were significantly more responsive to cytokines and inflammatory signals (**Fig. 4C**). We profiled tumor clusters for expression of known inhibitory and activating ligands as well as for cytokines/chemokines and cytokine/chemokine receptors (**Figs. 4D** and **4E**). Importantly, of all chemokine receptors, we observed that *HLA-E*$^{HIGH}$ bladder tumor cells had significantly higher *ACKR3* (CXCR7) expression, and pseudo-bulking the scRNAseq data revealed that HLA-E and CXCR7 tumor expression were strongly correlated (**Fig. 4F**). Additionally, we profiled the abundance of each tumor cluster according to BCG treatment status and observed cluster B2 was uniquely enriched in BCG-naïve tumors (**Fig. 4G**). The other tumor clusters were either evenly distributed between naïve and unresponsive tumors or they were disproportionately skewed towards unresponsive.

Collectively, our analyses of NK cells, T cells and tumor cells suggest immune crosstalk within the TME. Further, the data are supported by our observations that NKG2A$^{+}$ NK and CD8 T cells are

344 significantly closer in proximity to HLA-E$^{HIGH}$ tumor cells (**Fig. 2**). NK cells and T cells expressed a
345 variegated array of *CXCR3, CXCR4*, and *CCR7* (**Fig. 3I**) and *HLA-E*$^{HIGH}$ tumor cells uniquely express
346 *ACKR3* (CXCR7) (and to lesser extent *CXCR4*) (**Fig. 4E**), indicating an important axis with CXCL12.
347 Additionally, *KLRC1*-expressing NK and CD8 T cells expressed significantly higher *AREG* (amphiregulin)
348 which signals through EGFR. To test the hypothesis that chemokine signaling explains why NKG2A$^{+}$ NK
349 and CD8 T cells are biased towards HLA-E$^{HIGH}$ tumor cells, we measured across all major clusters
350 expression of chemokines and their receptors: a) CCL19, CCL21 → CCR7; b) CXCL9, CXCL10, CXCL11
351 → CXCR3; c) CXCL12 → CXCR4 and CXCR7; and d) amphiregulin → EGFR (**Fig. 4H**). We observed
352 *HLA-E*$^{HIGH}$ tumor cells expressed higher levels of EGFR compared to *HLA-E*$^{DIM/NEG}$ tumor cells, whereas
353 *AREG* was expressed by NK cells as well as dendritic cells (DCs), monocytes, mast cells, and even *HLA-*
354 *E*$^{HIGH}$ tumor cells at low levels. CXCL12 was mostly expressed by stromal cells, whereas CXCR4 was
355 expressed by NK cells, B and T cells (including Tregs), and myeloid cells. CXCR3 was mostly relegated
356 to NK and T cells and DC1 cells, and CXCL9, CXCL10, and CXCL11 were mostly expressed by
357 monocytes, macrophages and DCs. Finally, CCL19 was very specific for mregDCs and CCL21 by
358 endothelial cells suggesting important interactions with CCR7-expressing B and T cells.

359 In a recent study of BCG-unresponsive NMIBC by Rouanne et al[26], the authors demonstrated that
360 BCG can directly infect bladder tumor lines driving epithelial to mesenchymal transitioning (EMT),
361 autophagy flux impairment, a loss of class I HLA expression, and increased cell cycling. The study focused
362 on BCG-unresponsive NMIBC and found that patients with a dominant tumor phenotype showing these
363 hallmarks experienced significantly poorer metastasis-free survival. In our study, we next sought to stratify
364 tumor cells according to their HLA-E expression and measure average gene expression across the hallmark
365 pathways for EMT, autophagy, and cell cycle (**Extended data Fig. S3**). We observed a remarkably similar
366 phenotype of HLA-E-negative tumors as *in vitro* BCG-infected tumor lines showing significantly higher
367 EMT phenotype along with reduced autophagy flux genes and increased cell cycle. The data might suggest
368 that a proportion of recurring tumor cells in the face of BCG therapy, undergo *in vivo* infection rendering
369 them less sensitive to cytokine stimulation and chemokine attraction and promoting this stratification where
370 HLA-E$^{HIGH}$ tumor cells are in significantly closer proximity to CXCL12$^{+}$ stromal cells and immune cells.

371 To study the potential interactions between NK and CD8 T cells and HLA-E$^{HIGH}$ tumor cells, we
372 modeled the interactions using NicheNet, an algorithm that uses a combination of transcriptomic data,
373 known ligand-receptor interactions, and gene-gene signaling and regulatory relationships to predict
374 potential interactions between cells of interest (**Fig. 4I**) [33]. The top twelve ranked ligands from KLRC1$^{+}$
375 NK, KLRC1$^{+}$ CD8 T cells, and KLRC1$^{+}$ T cell-cycle cells predicted to interact with HLA-E$^{BRIGHT}$ tumor
376 cells were *IFNG*, *TNF, TNFSF12* (TWEAK), *APOE, TNFSF14* (LIGHT), SEMA4D, *TNFSF10* (TRAIL),
377 *AREG, GZMB, ALOX5AP, GPI, NUCB2* (**Fig. 4J**). KLRC1-expressing T cell-cycle and CD8 T cells

378 expressed the highest levels of IFNG, while *AREG* expression was highest in NK cells. Putative receptors
379 for these ligands, including *IFNGR1*, *IFNGR2*, *TNFRSF1A/10B/12A/14/21, SORL1, LDLR, AMFR,*
380 *ALOX5, EGFR, IGF2R, and PLXNB1* were most highly expressed in the BCG-unresponsive samples,
381 suggesting the presence of corresponding signaling activity by recurring tumors (**Fig. 4J**). To further
382 examine genes upregulated in the tumor as a consequence of signals from NK and T cells, a circos plot
383 revealed the ligand-target weights of the top third of predicted relationships between 'sender' or effector
384 ligands and 'receiver' or target genes, defining the 'putative effects of the HLA-E/NKG2A axis" in bladder
385 tumors as well a targeted 'IFNγ-mediated' and 'AREG-mediated' adaptive resistance signatures (**Fig. 4K**).
386

387 **Organization of the TME through immune crosstalk with stroma and HLA-E$^{bright}$ tumors**

388 To spatially resolve the relationships between tumor cells, stroma and immune infiltrates, we
389 performed spatial transcriptomics (ST-seq) analysis of bladder tumor sections from four treatment-naïve
390 and four BCG-unresponsive tumors (**Fig. 5**). Clustering analysis revealed 12 unique clusters, where cluster
391 12 remained unclassified and was removed from subsequent analyses (**Fig. 5A-5C**). Clusters were
392 annotated by their proportional composition by immune, stromal, and/or tumor cells defined using gene
393 signatures derived from scRNAseq analysis (**Figs. 3** and **4**). Clusters were defined both by the gene content
394 defining immune, stromal, and/or tumor cells but additionally integrating regional features of the tumor
395 tissue (**Fig. 5C** and **5D, Extended Figure S4**). We profiled the relative abundance of each spatial cluster
396 between BCG-naïve (pre-BCG) and BCG-unresponsive (post-BCG) tumors (**Fig. 5E**). We observed clear
397 differences, where spatial clusters #0, 3, 4, and 6 were substantially enriched in BCG-unresponsive tumors.
398 Conversely, there was a trend for enrichment of clusters # 1, 2, 5, 7, 8, and 11 in BCG-naïve tumors. Only
399 spatial cluster # 8 lacked the presence of immune cells, and cluster 10 was defined by neutrophils
400 exclusively, where they were near regions enriched with DCs, Tregs, T cell-cycle and tumor cells.

401 ST-seq Visium™ spots are 55μm in diameter and require deconvolution to understand which cell
402 lineages are represented as well as their relative abundances (**Fig. 5F**). We performed neighborhood
403 analyses to measure proximity of *HLA-E*$^{HIGH}$ and *HLA-E*$^{DIM/NEG}$ tumor Visium spots to CD8 T cells and NK
404 cells (**Fig. 5G**) as well as Tregs (**Fig. 5H**). A summary of the average distances to *HLA-E*$^{HIGH}$ and *HLA-*
405 *E*$^{DIM/NEG}$ tumor Visium spots from BCG-naïve and BCG-unresponsive tumors revealed significantly closer
406 proximity of *HLA-E*$^{HIGH}$ tumor spots to NK cells, Tregs, and CD8 T cells. This observation was restricted
407 to BCG-unresponsive tumors (**Fig. 5I**).

408 To better understand the mechanisms underlying preferential interactions of immune cells with
409 *HLA-E*$^{HIGH}$ tumor cells, we tested the hypothesis that stroma-produced CXCL12 mediates recruitment of
410 CXCR7$^{+}$ HLA-E$^{HIGH}$ tumor cells to regions where macrophages and DCs produce CXCL9, CXCL10, and/or
411 CXCL11 that mediate recruitment of NK cells and T cells (**Fig. 4H**). Spatial relationships were investigated

412 on the 'nano-environment' level, defined as a Visium spot with a radius of 2.5 adjacent Visium spots, or
413 ~138 microns. A representative BCG unresponsive tumor section with brightfield image of underlying
414 tissue is shown with *HLA-E*$^{HIGH}$ tumor/stroma Visium spots shown in blue, and *HLA-E*$^{DIM/NEG}$ Visium spots
415 shown in tan represented in **Fig. 6A**. Additional profiling of NK and CD8 T cells and Tregs revealed their
416 distribution being close in proximity to *HLA-E*$^{HIGH}$ tumor/stroma Visium spots. BCG-unresponsive tumors
417 revealed significantly higher levels of tumor/stroma spot infiltration with cytotoxic NK and CD8 T cells
418 (7.05 times closer) and regulatory T cells (Tregs, 2.66 times closer) when compared to the BCG-naïve state
419 ($p < 0.0001$ for both). Using the same representative BCG-unresponsive tumor section, a topographical
420 map of HLA-E expressing tumor/stroma spot density is shown overlaid on top of a neighborhood analysis
421 highlighting the intensity of neighboring NK and CD8 T cell infiltration (**Fig. 6B**).
422 To investigate the biased distribution of NK and T cells near *HLA-E*$^{HIGH}$ tumor-stroma spots, we
423 profiled bladder tumor-stroma spots for expression of cytokines and chemokines (**Fig. 4H**). Among the
424 chemokines with detectable gene expression by ST-seq analysis, we observed a strong correlation between
425 CXCL9 (**Fig. 6C-6E, Extended Figure S5**) and HLA-E expression as well as between CXCL12 and HLA-
426 E expression (**Fig. 6F** and **6G**). We next applied our neighborhood analysis to profile tumor expression of
427 known checkpoint ligands, HLA class I expression as well as the IFN-response pathway as a function of
428 proximity to neighboring NK cells and CD8 T cells (**Fig. 6H**). Analysis of 5,319 tumor-stroma spots
429 (defined by >95% tumor- and stroma-specific genes revealed a clear program by tumor/stroma regions
430 increasing expression of inhibitory ligands *CD47*, *CD274* (PD-L1), and *HLA-E* as a greater number of NK
431 cells and CD8 T cells were in contact with tumor-stroma spots (**Fig. 4G**). Additionally, we observed
432 increased tumor-stroma spot expression of the apoptotic genes *PDCD2* and *FAS* and the adhesion molecule
433 *CD58* (LFA-3), known to interact with CD2-expressing NK and T cells. Finally, tumor-stroma spot
434 expression of *IFNGR1* and *IFNGR2* along with *JAK1*/*JAK2*, *STAT1*, *IRF1* and *IRF9* were increased as a
435 greater number of NK and CD8 T cells were in contact. *STAT3* expression did not change as a function of
436 neighboring NK and CD8 T cells, and *SOCS1* expression was reduced with neighboring NK and CD8 T
437 cells, suggesting that tumor-stroma regions are actively responding to IFN signals. Tumor-stroma
438 expression of these genes was further stratified according to high vs dim/negative expression of *HLA-E*
439 (**Fig. 6I**).
440 To validate the ST-seq analyses, we used immunofluoresecence and the PhenoCycler/CODEX
441 platform to profile 59 antibodies (**Supplemental Table S2**) in order to better define the interactions between
442 tumor cells and multiple cell lineages. Antibodies targeted markers distinguishing tumor cells (pan-
443 cytokeratin (CK), GATA-3, S100A4) from stromal endothelial cells and fibroblasts (Collagen Type IV,
444 podoplanin, vimentin, PECAM1/CD31), and immune cells (CD45), including monocytes, macrophages,
445 dendritic cells (CD14, CD16, CD68, CD11b, CD11c, HLA-DR), neutrophils (CD66b, CD16), B cells

446 (CD20, CD138), CD4 and CD8 T cells (CD3, CD4, CD8), Tregs (CD3, CD4, FoxP3), and NK cells
447 (NKp46, Gzm.B, CD16) (**Fig. 6J** and **6K**).
448
449 **Tumor-derived NK and CD8 T cells retain functional competence at time of tumor recurrence.**
450 To better understand if an elevated expression of cytolytic genes in tumor-derived NKG2A-
451 expressing NK and CD8 T cell populations correlated with improved functional sensitivity, we used mass
452 cytometry (CyTOF) to profile the *in vitro* responsiveness of tumor-derived cells from BCG-unresponsive
453 NMIBC patients at time of tumor recurrence. We tested their ability to respond to HLA-E$^+$ PD-L1$^+$ tumors
454 in the presence/absence of durvalumab (anti-PD-L1 antibody) and/or monalizumab (anti-NKG2A
455 antibody), using an artificial K562 acute myeloid leukemia tumor model that allows for uniform HLA-E
456 and PD-L1 expression via pre-stimulation of tumor lines with exogenous recombinant IFN-γ. Briefly, after
457 24 hours incubation with recombinant IFN-γ [400ng/ml], stably transduced HLA-E$^+$ K562 cells saw 2.7-
458 fold and 2.1-fold-increase in expression of HLA-E and PD-L1, respectively, when compared with baseline
459 expression levels (**Fig. 7A**). Separately, tumor-infiltrating lymphocytes from four BCG-unresponsive
460 tumors were isolated and then expanded up to 13 days in the presence of low dose IL-2, IL-7, and IL-15 as
461 well as tetramers targeting CD3 and CD28. Finally, TGF-β, was included in the stimulation cocktail for an
462 additional three days to promote NKG2A expression by CD8 T cells [24]. Phenograph clustering analysis [34]
463 of expanded TILs revealed NK cells uniformly expressing NKG2A as well as 10 unique clusters of CD8 T
464 cells with variegated expression of inhibitory checkpoint receptors (CD161, GITR, LAG3, PD-1, TIGIT,
465 Tim-3, NKG2A) as well as markers of activation, trafficking, and tissue residence (CD25, CCR4, CCR6,
466 2B4, CD103, CXCR3) (**Fig. 7B** and **7C**). Four clusters (ID#: 2, 9, 15, 17) expressed elevated levels of
467 NKG2A, representing ~32.5% of the total CD8 TILs and reflecting the fraction of TILs predicted to react
468 to NKG2A-blockade. Additionally, ~9% (range, 3.91% - 14.04%) of all expanded TILs were comprised of
469 NK cells (CD14$^-$ CD19$^-$ CD3$^-$ CD56$^+$) and NK and CD56$^+$ CD8 T cells were strongly enriched for co-
470 expression of NKG2A. CD56 was then used as a surrogate for NKG2A as use of monalizumab precluded
471 our ability for detecting NKG2A with antibodies by CyTOF. Further, NKG2A and PD-1 expression by
472 CD8 T cells was variegated highlighting the dynamic and non-redundant mechanisms for regulating CD8
473 T cell activation [24].
474 Following expansion and characterization, we performed 6-hour co-cultures of TILs with K562
475 cells with and without HLA-E and/or PD-L1 expression (**Fig. 7D-7F**). Additionally, we measured the
476 effects of PD-L1-blockade or combined PD-L1- and NKG2A-blockade on NK and CD8 T cell
477 degranulation (CD107a) and expression of IFN-γ. WT K562 cells were used as positive control condition
478 for measuring NK and NKG2A-expressing CD8 T cell activation. We observed that NK cells and CD56$^+$
479 CD8 T cells were sensitive to HLA class I$^{-/-}$ K562 cells compared to *ex vivo* activity, and their response was

480 diminished when K562 cells stably expressed HLA-E or HLA-E and PD-L1. NK cell activation was
481 restored in response to both HLA-E$^+$ and HLA-E$^+$ PD-L1$^+$ K562 cells when pre-treated with anti-NKG2A
482 Ab alone or in combination with anti-PD-L1 Ab (CD107a: 2.1-fold increase, p=0.02; IFN-γ: 1.6-fold
483 increase, p=0.05).

484 Unlike NK cells, CD56$^+$ CD8 T cells were more dynamic in their co-expression profiles for
485 NKG2A and PD-1 staining. Similar to NK cells, untreated CD56$^+$ CD8 TILs were not reactive to HLA-E$^+$
486 K562 cells with or without co-expression of PD-L1. Activation of CD56$^+$ CD8 TILs was only significant
487 in the presence of both anti-NKG2A and anti-PD-L1 Abs (CD107a: 1.75-fold increase, p=0.02; IFN-γ: 1.8-
488 fold increase, p=0.007) (**Fig. 7F**). Collectively, the data strongly suggest sensitivity of NK and CD8 T cells
489 to combination immunotherapy strategies following tumor recurrence after failing BCG therapy.

490

491 **Discussion:**

492 Adaptive resistance can be driven by tumor-intrinsic and/or extrinsic mechanisms in overcoming
493 immune pressures [11, 12, 13, 35]. Evidence from mouse and human studies demonstrates that interferons, while
494 stimulating a robust anti-tumor response, also upregulate immune-suppressive factors in the setting of
495 prolonged activation. In melanoma, IFN-γ from CD8 T cells was shown to upregulate tumor PD-L1
496 expression and mediate infiltration of FOXP3$^+$ regulatory T cell pathways within the TME [36]. In a broader
497 meta-analysis across 18 tumor indications, including bladder cancer, inflammatory mediators including
498 IFN-γ were associated with inhibitory immune checkpoints, including PD-L1/L2 [37, 38]. Despite emerging
499 evidence positioning pro-tumorigenic roles for IFN-γ, there are well-established anti-tumor functions
500 mediated through IFN-γ that are critical for anti-PD-L1 immunotherapy [39]. Anti-tumor inflammation,
501 therefore, exists along a continuum where an equilibrium is necessary for appropriate immunotherapeutic
502 efficacy[40].

503 In a recent investigation conducted by Rouanne et al.[26], distinct patterns of disease progression after
504 BCG therapy and cystectomy were identified in the context of NMIBC. The study revealed that BCG-
505 unresponsive NMIBC patients characterized by tumors bearing a 'BCG infection' phenotype correlated
506 with poorer survival. Conversely, BCG-unresponsive patients exhibiting HLA class I proficiency in tumor
507 cells after BCG therapy (before cystectomy) demonstrated greater abundance of CD8 T cell tumor
508 infiltrates, upregulation of inflammatory cytokines, and the presence of inhibitory checkpoint molecules.
509 This latter group experienced significantly improved metastasis-free long-term survival post-cystectomy.

510 In our own investigation, we delved into the primary resistance mechanisms to BCG therapy and
511 explored the impact of BCG-induced inflammation on the dynamic interplay between tumor and immune
512 cell populations. Utilizing both prospective and retrospective NMIBC specimens collected before, during,

513 and after BCG treatment, our study uncovered a pervasive inflammatory response in both BCG responders
514 and non-responders alike. Our findings implicated IFN-γ in directly contributing to the upregulation of
515 HLA-E by approximately 43% of recurring NMIBC tumor cells, and uniquely evident in all BCG-
516 unresponsive patients. Spatial analyses of tumor cells, stratified by their proximity to infiltrated NK and T
517 cells, unveiled a program of tumor activation (and potential dysregulation) and selective recruitment to
518 stromal-rich regions replete with immune effector and regulatory cells that are responding to the same
519 collection of chemotactic signals.

520 Distinctive to BCG-unresponsive tumor cells, localized areas or 'nests' exhibiting elevated
521 expression of HLA-E were enriched for expression of CXCL9 and CXCL12. This activation correlated
522 with the infiltration of NK cells, CD8 T cells, and Tregs. Notably, even within confined regions of tumor
523 tissue featuring a mix of HLA-$E^{DIM/NEG}$ and HLA-$E^{HIGH}$ tumor cells, a significant preference was observed
524 for the proximity of NK and CD8 T cells to HLA-$E^{HIGH}$ tumor cells. These findings hint at an evasion
525 mechanism wherein HLA-$E^{HIGH}$ tumor cells (responding to stroma-derived CXCL12) appear to play a role
526 in safeguarding HLA class I negative tumor cells. The expression of the NKG2A receptor also emerged as
527 a critical factor in categorizing the anti-tumor cytolytic functions of NK and CD8 T cells. However, our
528 observations revealed that $NKG2A^{+}$ NK and CD8 T cells also expressed several well-established secondary
529 checkpoint receptors, emphasizing the necessity for a comprehensive understanding of the inhibitory
530 landscape within patients' tumors to inform effective second-line immunotherapy strategies.

531 Upon removing NK and CD8 T cells from their suppressive microenvironment, these cells
532 demonstrated retained functional capacity. Both NK and CD8 T cells, enriched for NKG2A expression,
533 exhibited highly enhanced cytolytic reactivity to HLA-$E^{+}$ PD-$L1^{+}$ K562 tumors in the presence of
534 combination NKG2A/PD-L1 blockade. Collectively, these findings portray a landscape of immune
535 dysregulation prominently characterized by elevated tumor expression of HLA-E and PD-L1 in the context
536 of BCG-induced chronic activation and inflammation. Importantly, HLA-$E^{HIGH}$ tumor cells similarly
537 expressed higher levels of CD47, Nectin-2 (CD112), Nectin-4, PVR and at higher levels compared to PD-
538 L1 expression. Further, HLA-$E^{HIGH}$ tumor cells expressed higher levels of decay accelerating factor (DAF,
539 *CD55*) and CD59, which block C3 convertase and formation of the membrane attack complex, two critical
540 steps in driving complement-mediated inflammation and phagocytosis, and apoptosis, respectively. Finally,
541 the trophoblast-2 (Trop2) antigen was highly expressed on all recurring NMIBC tumor cells. These data
542 suggest future combination immunotherapy strategies may benefit from additional targets that are strongly
543 engaged in BCG-unresponsive NMIBC patients. Emphasizing this point, antibody-drug conjugates
544 targeting Trop2 (sacituzumab govitecan)[41] and Nectin4 (enfortumab vedotin)[42] have demonstrated
545 promising improvements in patient outcomes for metastatic triple-negative breast cancers and muscle-
546 invasive bladder cancer, respectively; the latter which, when combined with pembrolizumab (PD-1

547 blockade), has recently been approved FDA clearance in an all comer population for 1st line treatment of
548 metastatic urothelial carcinoma [43].

549 Intravesical administration of BCG is initiated as adjuvant immunotherapy, as complete tumor
550 resection is the initial diagnostic and therapeutic step. Thus, initiation of standard of care (SOC) BCG
551 immunotherapy presupposes inflammation without an active tumor to clear [44]. Treatment improvements for
552 NMIBC and BCG-resistant disease have lagged. This may be, in part, because few studies have attempted
553 to understand the relationship between the timing of tumor recurrence, reasoning for the recurrence, and
554 the state of the immune system at the time of recurrence. Poor dosing study designs and lack of
555 understanding of the mechanisms underlying a therapeutic response to intravesical BCG have led to a
556 significant gap in knowledge and benefit for patients with NMIBC compared to muscle-invasive or
557 metastatic disease.

558 Our findings suggest that all NMIBC patients at the time of tumor recurrence show signs of a
559 hallmark anti-tumor immune response dominantly driven by IFN-γ. BCG-unresponsive tumors see uniform
560 increases in chemotactic cytokines and inflammatory pathways that should otherwise function to suppress
561 tumor growth. Further, increased expression of inhibitory ligands on BCG-unresponsive tumor cells was
562 observed, suggesting that inflammatory stimuli had been prolonged and triggered feedback mechanisms
563 responsible for immune evasion. These results are seen on multiple levels, including bulk and single-cell
564 RNA sequencing, spatial sequencing, multiplex imaging, and mass cytometry. This implies that when
565 tumors recur, for reasons beyond the scope of this study, they are met by an overactive status of the immune
566 system ill-equipped to combat them.

567 Previous analyses profiling urine analytes between the BCG naïve and third dose timepoints
568 demonstrated that three doses of BCG induced an inflammatory response hundreds of times above baseline
569 levels of cytokines, including but not limited to IP-10, MIP-1β, IL-8, IL-6, and TNFα [45]. Importantly, the
570 third dose-response dwarfed the magnitude of the first dose-response, suggesting that repeated exposure
571 increases the magnitude of inflammation [45]. While these data did not profile out to the time of tumor
572 recurrence, they lend credence to the theory that all patients experience a ubiquitous and increasingly
573 powerful immune response to repeated doses of BCG. Importantly, our findings confirm these previous
574 observations. Further, they demonstrate that inflammation is sustained even throughout the six-week
575 treatment interruption at time of first cystoscopy and do not equilibrate to baseline levels.

576 Novel to our study is the spatially-resolved insights into potential consequences of IFN-γ
577 dysregulation and tumor cell and immune homing patterns. Preferential trafficking of *HLA-E*$^{HIGH}$ tumor
578 cells to immune-rich regions was seen in areas of high expression of *CCL19, CCL21, CXCL9/10/11*, and
579 CXCL12, and chemokines were detected in the urine early following start of therapy and were sustained
580 throughout therapy. Further, BCG unresponsive tumor-stroma proximity to cytolytic cells and Tregs was

increased by a median of 7-fold and 2.6-fold, respectively, when comparing *CXCL9/10/11*$^{HIGH}$ to *CXCL9/10/11*$^{DIM/NEG}$ tumor nests.

Clinical efficacy in checkpoint blockade is dependent on reinvigorating effector cells expressing high levels of the targeted checkpoint(s). Congruent with analogous studies, we found that NKG2A$^{+}$ NK and CD8 T cells were enriched in BCG-unresponsive tumors and tumor-derived NK and CD8 T cell anti-tumor functions were intact at the time of tumor recurrence. Additionally, co-culture experiments with patient TILs and K562s with and without HLA-E and PD-L1 confirmed the ability of combination anti-NKG2A plus anti-PD-L1 blockade to enhance the cytolytic function of stimulated TILs from patients at time of tumor recurrence. This reinforces both the use of NKG2A to reinvigorate cytolytic effector functions by NK and CD8 T cells, as well as the potential to exploit a critical mechanism of tumor resistance, whereby chemokines lure in effector cells to take on exhausted phenotypes.

Recent clinical evidence emerging from interim results of the randomly controlled Phase II COAST trial demonstrated significantly prolonged survival in non-small cell lung cancer (NSCLC) patients treated with monalizumab combined with durvalumab compared to standard of care durvalumab alone for treatment of unresectable stage 3 NSCLC [25]. This combination is being further evaluated in a larger planned Phase III trial (PACIFIC-9, NCT05221840) following these promising early results. Collectively, our data demonstrate that elevated tumor expression of HLA-E and PD-L1 and chronic activation of NKG2A-expressing NK and CD8 T cells are hallmark features of resistance to BCG immunotherapy in NMI bladder tumors and that integrating NKG2A-blockade into combination immunotherapy strategies may prove particularly effective in settings of BCG-unresponsive, high-grade NMIBC. Based on the data generated from this study, we recently designed a Phase 2 trial of durvalumab (MEDI4736) and monalizumab in NMIBC. The Phase 2 ENHANCE (**E**levated **N**KG2A and **H**LA-E **A**mplify **N**K and **C**D8 T-cell **E**ngagers) (clinicaltrials.gov ID: NCT06503614) will investigate the effects of monalizumab (anti-NKG2A Ab) plus durvalumab (anti-PD-L1 Ab) for combination checkpoint blockade in high-grade BCG-unresponsive NMIBC as a bladder-sparing immunotherapy strategy. In this trial, an exploratory objective is to assess the relationship between baseline tumor HLA-E expression and clinical outcomes to facilitate development of HLA-E as a potential biomarker for patient selection in future clinical trials intending to target NKG2A.

Our study has notable limitations. Our sample sizes, while being the largest NMIBC spatial sequencing and single-cell RNA sequencing cohorts available, are small and present a potentially limited view of the disease. Additionally, as BCG is administered as an adjuvant therapy, we are only afforded access to bladder tissues after treatment if tumor recurs. Thus, it was not feasible to profile bladder tissues in the absence of tumor following exposure to BCG. Future studies might benefit from a neoadjuvant approach, where tumor tissue can be sampled and profiled for potential therapeutic responses to BCG.

614 Collectively, our analyses suggest that the current guidelines on immunotherapy for BCG-
615 unresponsive NMIBC could be improved via a multi-cell-targeting immunotherapy approach focused on
616 NK cells alongside T cells. Randomized trials from bladder and other tumor indications have shown that
617 PD-1/PD-L1 stratification fails to predict response to immunotherapy with anti-PD-1/PD-L1 antibodies:
618 IMvigor210, JAVELIN bladder 100, and CheckMate-275 (NCT02108652, NCT01772004, NCT02387996)
619 all saw that PD-1/PD-L1 biomarker stratification alone did not effectively stratify response rates. In
620 comparison, recent results using *KLRC1* (NKG2A) expression in the pre-treatment tumor significantly
621 improved predicted anti-PD-L1 response rates in the IMvigor210 cohort, but only in the $CD8^{HIGH}$ *PDCD1*
622 $(PD\text{-}1)^{HIGH}$ group [24]. In fact, where IHC stratification of PD-L1 expression has failed to predict
623 immunotherapeutic responses, *KLRC1* stratification in IMvigor210 showed protective effects were
624 restricted to the PD-L1 IC high group. In conclusion, while our analysis does not exclude the presence of
625 alternative checkpoints, it lends evidence to the hypothesis that combination NK and T cell
626 immunotherapeutic approaches may hold the key to improved outcomes for NMIBC patients.
627

628 **Methods**

629 **Patients and samples**

630 Patients at Mount Sinai Hospital (MSH) were enrolled in the study following Institutional Review
631 Board (IRB) approval (protocol 10-1180). 10-1180 covers the use of patient tissues in a biorepository and
632 allows for prospective collection of blood, urine, and tissue samples from enrolled patients. Formalin-fixed
633 paraffin-embedded (FFPE) blocks from BCG patients were obtained retrospectively from the biorepository
634 and prospectively for patients receiving treatment. For prospective patients, samples were collected on the
635 day of surgery and throughout BCG immunotherapy. Due to IRB limits on the collection, blood and urine
636 samples were taken at the first dose, third dose, and sixth dose of the induction cycle; at every follow-up
637 cystoscopy; and at the third maintenance cycle dose. Tumor samples were taken at every possible timepoint.
638 BCG naïve was defined as any patient who had yet to receive BCG, regardless of past treatment with other
639 chemotherapies. BCG-unresponsive was defined as any patient with recurrent tumors following at least five
640 of six induction doses of BCG at time of first evaluation.
641

642 **Sample processing**

643 Blood and urine samples from bladder cancer patients were processed to collect PBMCs, serum,
644 and cell-free urine. Blood was spun down (4C, 2000rpm, 10 min) to isolate serum, and PBMCs were
645 collected using Ficoll-Paque isolation. PBMCs were frozen down in a Mr. Frosty at -80 C for 24 hours and

646 stored at -160 C in 10% DMSO and 90% fetal bovine serum; PBMCs and cell-free urine were stored at -80
647 C.

648 Tumor tissues obtained from transurethral resections of bladder tumor (TURBT) were placed into
649 RPMI medium immediately after removal and transferred to the laboratory for additional processing.
650 Bladder and lymph nodes obtained from radical cystectomies were sent from the operating room directly
651 to the pathology suite after completion of the lymph node dissection. The bladder was bivalved; samples of
652 visible tumor were extracted and placed in RPMI medium, and the tumor was transferred to the laboratory
653 for additional processing.

654 Fresh tumor samples underwent a variety of different processing techniques based on the planned
655 experiment. Tumor used for spatial sequencing was placed in a 10 mm x 10 mm cryomold with optimal
656 cutting temperature (OCT) media and frozen down on a thermal block immersed in liquid nitrogen. Tumor
657 tissues were digested using tumor dissociation enzymes (Miltenyi, 130-095-929) and a GentleMACS
658 machine (program 37C_h_TDK_3) at 37C. Mechanically and enzymatically separated tissues were filtered
659 through a 70μM cell strainer and assessed on Countess II (ThermoFisher) for viability and cell numbers.

660

661 **In situ hybridization and targeted RNA sequencing**

662 FFPE sections from 40 retrospective NMIBC cases were obtained from the institutional
663 biorepository and used for targeted RNA sequencing. RNA was extracted from five and ten μm sections.
664 HTG EdgeSeq lysis buffer was added to lyse and permeabilize the samples. Nuclease protection probes
665 (NPPs) were added to the lysed samples and hybridized to the target mRNA. A nuclease was added to
666 digest non-hybridized mRNA and excess NPPs. The nuclease digestion reaction was finalized with a
667 termination solution followed by heat-mediated denaturation of the enzyme.

668 Each sample was used as a template for PCR reactions with specially designed primers. Each primer
669 contains a unique barcode that is used for sample identification and multiplexing. Samples were analyzed
670 simultaneously on an Illumina sequencing platform to prepare the library. All samples and controls were
671 quantified in triplicates. No template control (NTC) reactions were made for each master mix used during
672 the qPCR process to test the absence of a probe or qPCR contamination. Molecular-grade water was used
673 in place of a test sample in the NTC reactions using the same volume as the template.

674 Sufficient concentration of sample for library pooling, appropriate dilution for the library pool, and
675 volume of denaturation reagents to add to the library were determined by HTG library calculator. 2N NaOH
676 and heat (98C, 4 minutes) were used for library denaturation. The denatured library was loaded into the
677 well of the NextSeq sequencing cartridge. Sequencing was performed using an Illumina NextSeq sequencer.

678 The sequencing data on mRNA expression of target genes were imported into HTG EdgeSeq parser
679 software. HTG biostatistics department performed quality control analyses and normalized the data. Data
680 were returned from the sequencer as demultiplexed FASTQ files with four files per assay well. The HTG
681 EdgeSeq parser software aligned the FASTQ files to the probe list and collated the data.

682 Prior to any analyses, clinical data on all patients was gathered. The following items were collected
683 for all samples processed by HTG Molecular: patient date of birth; gender; age at BCG induction; BCG
684 status (unresponsive vs. naïve vs. exposed); date of sample collection; stage at collection; grade at
685 collection; recurrence date; time to recurrence; time to progression; BCG start date; BCG last exposure;
686 BCG induction cycle last dose; prior chemotherapy; cystectomy; date of cystectomy; stage at cystectomy.

687 Following clinical data collection, a gene set enrichment analysis (GSEA) was performed on the
688 targeted RNA sequencing data. Specifically, we used paired patient samples before and after BCG exposure
689 in the BCG recurrent patient population only. We used custom gene sets, as well as all Hallmark gene sets
690 from the Broad Institute's MSigDB, as inputs for the enrichment analysis [27]. Statistical significance was set
691 at $p < 0.05$, and gene sets found to be significant are listed in **Supplementary Table S1**. All gene sets found
692 to be statistically significant were evaluated for leading-edge genes, defined as the genes that contribute
693 most to the enrichment score and associated p-value.

694 The leading-edge genes from statistically significant gene sets in the GSEA were collated and used
695 to assess for group differences between the paired HTG patient samples. We performed these analyses
696 specifically on the BCG-recurrent cohort. Prior to any analyses, a Shapiro-Wilk test, chosen for suitability
697 in small sample sizes, was used to assess for normality [46]. All samples with $p < 0.05$ were considered not
698 normally distributed, and a Kruskal-Wallis test was performed to assess for group differences [47]. All other
699 samples were assessed using an independent T-test. Genes with statistically significant differences between
700 the BCG naïve and the BCG-unresponsive populations were then visualized on radar plots.

701

702 **Protein concentration measurement**

703 Cell-free urine supernatant and serum samples were randomized in a 96-well plate. Diluted samples
704 and positive and negative controls were incubated overnight with an incubation mix (incubation solution,
705 incubation stabilizer, A-probes, and B-probes) at 4°C. Samples were then incubated with an extension mix
706 (High purity water, PEA solution, PEA enzyme, PCR polymerase) for 5 min and placed on a thermal cycler.
707 Following the thermal cycler, samples were incubated with a detection mix (detection solution, High purity
708 water, detection enzyme, PCR polymerase) and transferred to a chip. Primers were loaded onto the chip,
709 and the chip was profiled using the Fluidigm IFC controller HX with the Fluidigm Biomark Reader. Data

710 were normalized using extension and interplate controls and a correction factor. The resulting data were
711 reported in normalized protein expression (NPX) units on a log2 scale.
712
713 **IFN-γ co-culture**
714 Cell lines and CD45- isolated primary tumor cells were incubated in media optimized for high
715 viability for 72 hours (RPMI-1640 supplemented with 20% fetal bovine serum). Tumor cells were expanded
716 until they were confluent in 2 T175 flasks. Following expansion, cells were culture in 100 ng / mL of IFN-
717 γ for a total of 24 hours in a 24 well plate. Following co-culture, cell lines were trypsinized (immortalized),
718 and primary tumors were gently removed from the solid phase by a cell scraper. Samples with and without
719 IFN-γ stimulation were measured for HLA-E and PD-L1 protein expression levels.
720 HLA-E and PD-L1 levels were assessed via FlowCytometry. Cells were stained in 4C FACS buffer
721 (phosphate-buffered saline (PBS) with 2% heat-inactivated FBS and EDTA 2 mM) for 30 minutes.
722 Subsequently, cells were washed in PBS, incubated for 20 minutes in a viability dye, washed again with
723 PBS, and resuspended in 2% paraformaldehyde. The experiment was performed in triplicate, with three
724 readouts per cell line per experimental condition. FlowCytometry acquisition was performed using an LRS-
725 Fortessa (BD Biosciences), and data were analyzed using the CytoBank software. When staining for HLA-
726 E, cells were first stained 20 minutes with HLA-E prior to staining with additional PD-L1. In CytoBank,
727 several gates were applied to generate the final dataset. A live/dead gate was applied, followed by a gate to
728 remove doublets and isolate singlets. Lastly, the data was arcsinh transformed prior to analysis.
729 Once the final dataset had been generated, statistical significance between unstimulated and
730 stimulated cell lines was assessed. An independent t-test was run with a significance cutoff of $p < 0.05$.
731
732 **Plasma and cell-free urine supernatant protein concentration analysis**
733 We used the OLINK Proteomics®- inflammation panel to profile cell-free urine supernatant.
734 Protein levels were visualized at BCG naïve, third dose, sixth dose, and first-cystoscopy timepoint,
735 comparing NPX values for all patients between the BCG naïve timepoint and the sixth dose timepoint.
736 Additionally, urine supernatants from a validation cohort of NMIBC patients treated with BCG were used
737 from the Aarhus University as previously described [13]. In order to determine the suitable statistical test, a
738 Shapiro-Wilk's test was used to assess for normality, and a Kruskal-Wallis test was used in every instance
739 in which one or both samples were not normally distributed. An independent T-test was used in the event
740 both samples were normally distributed. All statistically significant p values were then used to assess
741 adjusted p values via the Benjamini-Hochberg correction, with an alpha of 0.05. All statistically significant
742 genes between the BCG naïve and sixth induction dose time points are shown.
743

744 **Multiplex Immunohistochemistry:**

745 Sections of tumor for immunohistochemical (IHC) staining were taken at a thickness of 3-mm from
746 formalin fixed paraffin-embedded (FFPE) blocks. H&E-stained sections were performed every 5 - 10 slices.
747 The Ventana Discovery Ultra (Roche Diagnostics) machine was used to automatically bake, deparaffinize,
748 and condition the slices. The RUO Discovery Universal (v21.00.0019) was used to perform chromagen
749 IHC on sequential slices. Primary antibodies included (CD3, HLA-E, NKp46, and NKG2A) and were
750 utilized for staining on NMIBC tumors. All slices followed the same protocol, which included a 60 minute
751 incubation at 37°C; secondary antibodies using OmniMap HRP or NP DISCOVERY (Roche Diagnostics);
752 signal detection using Discovery OmniMap. Nuclear counterstaining with Mayer's hematoxylin; and
753 conversion to high-resolution images via the NanoZoomer S10 Digital slide scanner (Hamamatsu).

754

755 **Tumor and CD3$^+$ T cell expression and proximity analyses**

756 Prior to analysis, all slides were reviewed and regions of interest were annotated by a board-certified
757 pathologist (R.B.). Tissue artifacts, including torn, folded, and damaged tissue, were excluded from any
758 analyses. The HALO™ (Indica Labs, Inc.) digital image analysis platform, a semi-automated platform using
759 machine learning to segment and label stained sections, was utilized for quantitative analyses. Halo AI™
760 and train-by-example classification, segmentation, and random forest classification was used to separate
761 chromogenic stains and generate tabular data for downstream analysis. Slide features of each tumor,
762 including cell lineages (tumor, stroma, and immune) and slide features (such as glass) were characterized.
763 Glass was excluded from all downstream analyese. Classified cell classes were tabulated, and positive
764 staining cells were stratified into expression tertiles (dim, moderate, and bright). Calibration for intensity
765 expression was performed using tonsil tissues from healthy human tonsil. In addition to cell counts, total
766 surface area ($mm^2$) was recorded to facilitate density calculations. Statistical analyses were performed using
767 Python 3.8.1.

768

769 **Proximity Ligation Assay**

770 The NaveniFlex™ Proximity Ligation Assay (PLA) was performed according to the manufacturer's
771 instructions using NaveniFlex Tissue MR ATTO647N (Navinci, Sweden). PLA was performed on sections
772 of tumor taken at a thickness of 3-mm from formalin fixed paraffin-embedded (FFPE) blocks. H&E-stained
773 reviewed with pathologist. Briefly, after deparaffinization, rehydration, and antigen retrieval, slides were
774 blocked with Block NT blocking solution (Navinci, NT.1.100.01) for 60 min at 37 °C in a preheated
775 humidity chamber and then incubated with mouse anti-HLA-E (clone: MEM-E/02, Abcam, 1:200) and
776 rabbit anti-NKG2A (clone: EPR23737-127, Abcam, 1:2000) diluted in Diluent 1 NT solution (Navinci,

NB.1.100.02) overnight at 4°C. As negative controls, two (tonsillectomy) slides were incubated in antibody diluent with only one primary antibody each. After washing, the slides were incubated with the PLA probes corresponding to the primary antibodies using anti-mouse Navenibody M1 NT (Navinci, NB.1.100.06) and anti-rabbit Navenibody R2 NT (NB.1.100.07) in Diluent 2 NT solution (Navinci, Navinci, NF.1.100.03) for 60 min at 37 °C. Slides were then processed for ligation using reaction 1 reagent containing Buffer 1 NT (Navinci, NB.2.100.17) and Enzyme 1 NT (Navinci, NF.2.100.11) and subsequently reaction 2 reagent containing Buffer 2 NT (NT.2.100.01) and Enzyme 2 NT (Navinci, NF.2.100.15) and incubated for 30 min at 37 °C and 90 min at 37 °C, respectively. The slides were washed and incubated with post-block NT reagent (Navinci, NF.1.100.01) in post-block supplement NT (Navinci, NT.2.100.04) for 30 min at 37 °C, then processed for detection, counter-stained with DAPI, and mounted with coverslips using Prolong Gold Antifade reagent (Invitrogen, P36930).

Images were captured at the Microscopy and Advanced Bioimaging Core of the Icahn School of Medicine at Mount Sinai. A Leica DMi8 (Leica Microsystems, Germany) was equipped with a HC PL APO CS 10x/0.4 (Part Number 506285; Leica Microsystems, Germany) objective lens. A SpectraX fluorescence illuminator (Lumencor, Oregon, USA) with multiple narrow-band light emitting diodes provided illumination (LEDs used: 395/25nm for DAPI, 470/24nm for autofluorescence channel, and 640/30nm for Navinci signal). The microscope and light source were controlled by LAS X software, version 3.7.5.24914 (Leica Microsystems, Germany). For fluorescence excitation, the following illumination settings were used: a 395nm LED set to 50% (147mW at the SpectraX output port) for DAPI signal, captured at 20 milliseconds of exposure; a 470nm LED set to 44% (86mW), captured at 70 milliseconds for an autofluorescence channel; and a 640nm LED set to 100% (231mW), captured at 150 milliseconds for the target signal. A multi-band pass filter set (Part Number 11525366; Leica Microsystems, Germany) was used to separate fluorophore emission (Dichroic 415/490/570/660nm; Emission bands: 430/35, 515/40, 595/40, 720/100nm). Images were captured using a Leica DFC9000GT monochrome camera set to 12-bit depth, 2x2 (4-pixel) binning and “Low Noise” Gain mode. Images were captured in montage at 10% overlap, merged (“Smooth” blending option) and then saved in the proprietary LIF ("Leica Image File") format before being converted to IMS (Imaris) format for analysis.

Image analysis was performed using Imaris software 10.1.1 (Oxford Instruments, Concord MA). A surface for the green background channel was created using the surface creation wizard with the following parameters – Enable Region Of Interest = false, Enable Region Growing = false, Enable Tracking = false, Enable Classify = false, Enable Shortest Distance = false, Enable Smooth = true, Surface Grain Size = 2.00 $\mu$m, Enable Eliminate Background = false, Active Threshold = true, Enable Automatic Threshold = false,

811 Manual Threshold Value = 1900, Active Threshold B = false. Masked channels were created by subtracting
812 the intensities within the green surface from the blue and far-red channels: the mask intensity was set to 0
813 for inside the green surface while the outside was set to the original channel's value. A new surface was
814 created using the surface creation wizard for the masked far-red channel using the following parameters –
815 Enable Region Of Interest = false, Enable Region Growing = false, Enable Tracking = false, Enable Classify
816 = false, Enable Shortest Distance = false, Enable Smooth = true, Surface Grain Size = 2.00 $\mu$m, Enable
817 Eliminate Background = false, Active Threshold = true, Enable Automatic Threshold = false, Manual
818 Threshold Value = 1600, Active Threshold B = false. An area filter was applied to this far-red surface to
819 remove surfaces whose area was larger than 50um$^2$. A DAPI surface was created using surface creation
820 wizard with the parameters – Enable Region Of Interest = false, Enable Region Growing = true, Enable
821 Tracking = false, Enable Classify = false, Enable Shortest Distance = true, Enable Smooth = true, Surface
822 Grain Size = 2.00 $\mu$m, Enable Eliminate Background = true, Diameter Of Largest Sphere = 7.50 $\mu$m, Active
823 Threshold = true, Enable Automatic Threshold = false, Manual Threshold Value = 10, Active Threshold B
824 = false, Region Growing Estimated Diameter = 6.00 $\mu$m, Region Growing Morphological Split = false,
825 Filter Seed Points = "Quality" above 60.0, Filter Surfaces = "Number of Voxels Img=1" between 10.0 and
826 500, to obtain individual nulcei within the field of views. Finally, a fourth surface was created by applying
827 the filter – Overlapped Area to Surfaces (Minimum = 0.050 um$^2$, Maximum = false) to obtain the DAPI
828 surfaces that were in contact with the far-red channel. The counts of total number of nuclei and nuclei
829 overlapping with the masked far-red surfaces were extracted from the statistics tab of Imaris.
830
831 **Single-cell RNA sequencing:**
832 **Data preprocessing**
833 Single-cell RNA sequencing (scRNA-seq) analysis was performed using Scanpy package in Python
834 and Seurat package in R. After loading, genes expressed in fewer than three cells were excluded from later
835 analyses. Cells with < 200 or > 8000 unique genes, as well as cells containing >20% mitochondrial gene
836 transcripts, were discarded. Cells then go through scrublet to detect doublet population. Subsequent data
837 normalization was performed by dividing feature counts for each cell by total counts for that cell, scaling
838 by a factor of 10,000, and natural log transformation. Next, scvi model was set up to correct batch-effects.
839 Then we performed scaling and principal component analysis (PCA) on the batch-corrected data. Using the
840 first 50 principal components (PCs), graph-based clustering and UMAP dimensionality reduction was
841 performed to reveal 16 cell clusters. Cluster-specific marker genes were identified using the FindAllMarkers
842 function, and marker genes with a natural-log fold change (FC) > 0.25 and expressed in >= 25% of cells
843 were used to annotate cell cluster identities based on known cell type markers [48, 49, 50]: CD8 T cells (*CD8A*,
844 *CD3E*), CD8- T cells (*CD3E*), tumor cells (*MUC1*, *KRT7/8/13/17/18*), B cells (*MS4A1*, *CD79A*),

845 monocytes/macrophages (*CD14*, *LYZ*, *FCGR3A*, *MS4A7*), T regulatory cells (*CD3E*, *FOXP3*), granulocytes
846 (*C1QA/B/C*, *ITGAM*, *FCGR3A*), NK (*NKG7*, *GNLY*, *KLRD1*, *KLRF1*), fibroblasts (*COL1A1*, *SPARC*),
847 epithelium (*EMP1*), DC (*FCER1A*, *CST3*, *ITGAX*), plasma cells (*MZB1*, *JCHAIN*, *IGHG3*), and CD8 TRM
848 cells (*CD3E*, *CD8A*, *KLRD1*). Clusters 22, 24, 25, and 26 containing 224, 142, 141, and 101 cells,
849 respectively, were ultimately excluded from further analyses due to unclear cell identities. All scRNAseq
850 analyses were performed using distinct samples without repeated measurements.
851

852 **Tumor subclustering analysis**

853 We performed subclustering analysis on 18,520 bladder cancer (Blca) cells. Preprocessing steps
854 for the Blca subset included normalization, scaling, and PCA analysis. We then applied Canonical
855 Correlation Analysis (CCA) integration using the IntegrateLayers() function (dimensional reduction for
856 correction = pca) in Seurat v5 to correct batch effects [51]. Leiden clustering (resolution = 0.4) was applied to
857 the shared nearest neighbors (SNN) (dims = 1:10). This resulted in the identification of 9 heterogeneous
858 tumor subclusters, distinctly separated on the UMAP plot. Each subcluster was profiled by the expression
859 of tumor marker genes (EPCAM, UPK2) and cytokines (CXCL1, CXCL2, CXCL3, IFNGR1, etc.).
860 Subcluster B1 was removed from further analysis as it was identified as normal bladder cells with low
861 EPCAM (tumor-related marker genes) , and subcluster B8 was removed due to high PTPRC expression,
862 indicating a high presence of immune cells (CD45+). Differentially expressed gene (DEG) analysis (MAST,
863 R version 1.2.1) [52] and enrichment pathway analysis [53] further characterized the subclusters, highlighting
864 their distinct biological profiles (Figure 2).
865

866 **NicheNet Analysis**

867 We used the NicheNet R package to infer potential ligand-receptor interactions between NK and T
868 cells and tumor cells, as well as potential regulatory effects in tumor gene expression as a result of these
869 interactions [33]. We added known ligand-receptor interactions between ligands IgG1 and IgG3 and the
870 receptor CD16 (weight = 1) to NicheNet's default ligand-receptor interactions database, and also integrated
871 the Harmonizome Pathway Commons Protein-Protein Interactions database:
872 (https://maayanlab.cloud/Harmonizome/dataset/Pathway+Commons+Protein-Protein+Interactions) with
873 NicheNet's default signaling network (weight = 1) [54, 55]. We used the modified ligand-receptor interaction
874 and signaling networks for subsequent analyses. We defined the NK and T cell populations as senders and
875 tumor cells as receivers and derived a list of 92 receptors expressed in the receiver population by
876 intersecting the list of receptors from the ligand-receptor interaction network with genes expressed in at
877 least 10% of tumor cells in the RNA assay. Fifty potential ligands expressed in greater than 10% of the

878 sender NK and T cells were then derived based on their interaction with the list of 92 receptors. We then
879 calculated activity scores for each ligand based on its potential to affect the expression of Hallmark
880 interferon gamma response genes [27, 56]. Statistical analyses including Wilcoxon rank-sum tests and Pearson
881 and Spearman correlations were performed using R v4.0.3.
882
883 **Differential gene expression analysis**
884 Spatial transcriptomic data were generated by Visium Spatial Gene Expression which is a spatial
885 transcriptomics solution by 10x Genomics. We obtained eight spatial sections consisting of four preBCG
886 and four postBCG samples. Sequencing data was aligned on GRCh38 and quantified using the Space
887 Ranger Software Suite (version 1.0, 10x Genomics). We processed the ST data to characterize major cell
888 types and their spatial patterns using Giotto workflow [57]. Per section, Low quality spots (number of
889 expressed genes > 100), and lowly expressed genes (expressed in < 10 spots) were removed. The raw counts
890 were log2(x+1) transformed, followed by adjusting for batch effects and spot wise number of features using
891 Pearson residuals approach by Lause et al [58]. The spatial network of nearest spots by Delaunay triangulation
892 was calculated to identify spatially co-expressed genes in neighboring spots via BinSpect-kmeans algorithm
893 [57], and distinct spatial domains by Hidden Markov Random Field (HMRF) model [57]. Then, different sections
894 were combined into a pan-section transcriptome by Harmony to identify pan-section clusters [59]. The pan-
895 section clusters will be identified by Leiden clustering [57] to detect transcriptionally similar spots shared
896 across different sections. Subsequently, we identified 12 spatial clusters to profile the spatial transcriptomic
897 landscape. Differentially expressed genes (DEGs) between $KLRC1^+$ versus $KLRC1^-$ cells were found using
898 the FindMarkers function from the Seurat R package, where cells with KLRC1 expression greater than 0
899 in the RNA assay were labeled as $KLRC1^+$.
900
901 **Identification of HLA-E high/low tumor subsets in spatial transcriptome**
902 As HLA-E expressions are not specific to tumors and HLA-E high/low tumor markers have not been
903 established, we performed a customized cell type presence inference workflow by utilizing Cell Atlas
904 Reconstruction from Spatially mapped Data (CARD) method [60]. CARD is a computational approach that
905 reconstructs cell-type-specific expression profiles from spatially mapped transcriptomic data, facilitating
906 the estimation of cell-type proportions within tissue sections. First, we generated reference single-cell
907 transcriptomes of $HLA\text{-}E^{high}$ and $HLA\text{-}E^{low}$ tumor subsets by explicitly labeling tumors with HLA-E
908 expressions (high: HLA-E > 0, low: HLA-E=0). These tumor labels were utilized as the inputs to calculate
909 the relative abundances of the tumor subsets on the spatial voxels by CARD.

910 To further scrutinize the detection of HLA-E high tumors in the spatial transcriptome (ST) data, we
911 applied additional thresholds to require voxels with i) high HLA-E expressions, and ii) highly abundant
912 HLA-E high tumor/stromal cells as inferred by CARD [60]. Per section, high HLA-E expression voxels were
913 identified as those with HLA-E expression values greater than zero (SCT normalized assay) and a z-score
914 of inferred HLA-$E^{high}$ tumor/stromal cell abundance > 1.645 (90% confidence). Conversely, low HLA-E
915 expression voxels were identified as those with an absence of HLA-E expression (HLA-E expression equal
916 to zero) and a z-score of inferred HLA-$E^{low}$ tumor/stromal cell abundance > 1.645 (90% confidence).
917 Similarly, we detected high confidence voxels with NK cells, CD8 T-cells and Treg cells by further applying
918 the abundance z-score > 1.645 for further analyses.

919 **Proximity analysis between different cell types**

920 We evaluated the proximity between different immune subsets (NK, CD8+ T, and regulatory T (Treg)
921 cells) and HLA-$E^{high/low}$ tumor cells to observe if distinct cytotoxic immune micro-environments are present,
922 conditioned on tumoral HLA-E expression status. Upon identifying high confidence voxels with HLA-
923 $E^{high/low}$ tumor/stromal cells and the immune cell types, we calculated the pairwise Euclidean distances
924 between the tumor/stromal cells and each immune cell type. To retrieve actual distance between voxels, the
925 matrix was refined using the computeCellDistance function from the CellChat v2 library in R [61]. For each
926 voxel with HLA-$E^{high/low}$ tumor/stromal cell presence, its overall distance to an immune cell type was
927 calculated as the mean distance over the 10 nearest neighboring voxels with the respective immune cell
928 presence. These distances were summarized across each section by taking the average over all HLA-$E^{high/low}$
929 tumor/stroma voxels, yielding the overall proximity with each immune cell type per section. These overall
930 proximity values were compared between pre-BCG and post-BCG groups by Wilcoxon Rank-sum test
931 (**Figs. 5** and **6**).

932 **In-depth analysis of cell type enrichment across spatial clusters**

933 We tested if each pan-section cluster shows enriched presence of distinct cell populations and subsets
934 as characterized by the scRNA-seq. To this end, for each section, we leveraged the inferred abundances of
935 different cell types in the spatial voxels by CARD, and tested if a cell type has significantly higher
936 abundances in each pan-section cluster than the other voxels by Wilcoxon Rank-sum test. Then, the overall
937 enrichments of each cell type within pre-BCG or post-BCG group were summarized by combining the
938 Wilcoxon test p-value across the sections via aggregated Cauchy association test (ACAT). The enriched
939 cell types per pan-section cluster in pre-BCG or post-BCG group were called with ACAT summarized FDR
940 < 0.05 and number of sections with significant enrichments (Wilcoxon FDR < 0.05) > 1 (Figure 4.3).
941

942 **Mass cytometry antibody preparation and staining**

943 PBMCs from BCG-treated bladder cancer patients at the time of tumor recurrence were isolated
944 using Ficoll-Paque and resuspended in cell medium (RPMI-1640 medium supplemented with 10% heat-
945 inactivated FBS, 1% Penicillin, 1% Streptomycin and 1% L-glutamine). PBMCs were conjugated to
946 antibodies purchased from Fluidigm using the Maxpar X8 and MCP9 labeling kits. Platinum barcodes were
947 prepared as previously described. All antibodies were titrated prior to conjugation.

948 Prior to mass cytometry staining, all cells were incubated for 20 minutes at 37C in RPMI cell
949 medium (described above) and IdU (Fluidigm, t#201127), Rh103 (Fluidigm, #201103A). Following the
950 incubation, cells were centrifuged, washed with PBS and 0.2% bovine serum albumin (BSA), and incubated
951 for 3 minutes on ice with an Fc-blocking reagent. Samples were washed again with PBS and 0.2% BSA;
952 barcoded samples were pooled together and washed; finally, samples were stained with extracellular
953 antibodies for 30 minutes on ice and in PBS and 0.2% BSA.

954 When staining four samples, cells were single-barcoded using 194Pt, 195Pt, 196Pt or 198Pt. When
955 staining five or six samples, cells were stained with combination of barcodes. Cells were again washed
956 using PBS 0.2% BSA; barcoded samples were pooled together; samples were washed again and stained
957 with extracellular antibodies for 30 minutes on ice in PBS 0.2% BSA. Cells were co-cultured in the presence
958 of either WT or HLA-E-transduced K562 cells for a total of 6 hours.

959 Samples were washed with PBS 0.2% BSA and resuspended in Fixation/Perm buffer (Invitrogen,
960 #00-5523-00) for 30 minutes on ice. Cells were centrifuged and washed with Maxpar Barcode Perm Buffer
961 (Fluidigm, #201057) and barcoded using the Cell-ID 20-Plex Pd Barcoding kit (Fluidigm, #201060).
962 Barcoded samples were washed with permeabilization buffer (Invitrogen, #00-5523-00) and pooled.
963 Intracellular staining was then performed in permeabilization buffer with Heparin at a concentration of
964 100U/mL for 30 minutes on ice. Stained cells were washed with permeabilization buffer and resuspended
965 in PBS with PFA 2.4%, saponin 0.08%, Osmium tetroxide 0.075nM and Ir 0.125uM (Fluidigm, #201192A).
966 Finally, samples were washed and resuspended in PBS 0.2% BSA and data were acquired within four days,
967 or frozen in FBS/DMSO 90/10. The antibody panel in Supplemental Table S4 was used to stain bladder
968 cancer patient samples.

969

970 **Mass cytometry sample acquisition and processing:**

971 Prior to acquisition, samples were washed with cell staining buffer and acquisition solution
972 (Standard Biotools). Following washing, samples were resuspended in acquisition solution (1 million cells
973 / 1 mL) containing a 1:20 dilution of EQ normalization beads. Data were then acquired using the Standard
974 Biotools Helios mass cytometer with a wide bore injector configuration at an acquisition speed of < 400
975 cells per second. The output files were normalized and concatenated using Standard Biotools' CyTOF
976 software, and outputted as FCS files.

977 The Mount Sinai Human Immune Monitoring Core's (HIMC) pipeline for processing and cleaning
978 was used to clean the resulting FCS files. Aberrant acquisition time-windows and low DNA intensity events
979 were stripped out by the sample preprocessing pipeline. Samples were then demultiplexed via the cosine
980 similarity of the Palladium barcoding channel on a cell-by-cell basis to every possible barcode used in a
981 batch. Once the cell-barcode labeling has been established, the signal-to-noise (SNR) ratio was calculated
982 by taking the difference between the highest and second highest similarity scores. Cells with low SNR
983 ratios were flagged as multiplets and removed. Finally, acquired multiplets are removed based on the
984 Gaussian parameters residual and offset acquired by the Helios mass cytometer.
985
986 **Data processing and analysis:**
987 Data were uploaded onto Cytobank and processed for downstream analyses. Several gates were
988 applied: a live dead gate and a doublets gate in sequential order. All data were arc-sinh transformed, and
989 no batch corrections were performed given all samples were run in a single batch. NK cells and CD8 T cell
990 subsets were identified via manual gating assignment. Files were downloaded onto Mount Sinai's
991 supercomputing cluster, Minerva, concatenated into a single object, and clinical data were assigned to each
992 sample. A phenograph analysis was performed to cluster the cellular data. Wilcoxon tests were run for
993 statistical significance and the Benjamini-Hochburg correction was applied.
994
995 **Tumor Invading Lymphocyte Expansion**
996 TILs were expanded by seeding single cells tumor dissociate at $10^5$ cells/well in 48-well Costar®
997 flat-bottom plates (Corning Inc., NY) in complete TIL medium, consisting of RPMI 1640 with L-glutamine
998 (Corning Inc., NY), 10% human AB serum (MiliporeSigma, MO), 1% nonessential amino acids (Thermo
999 Fisher Scientific, MA), 1% sodium pyruvate (Thermo Fisher Scientific, MA), 1% penicillin/streptomycin
1000 (Thermo Fisher Scientific, MA), and 3000 IU/ml interleukin-2 (Proleukin®, kindly provided by Clinigen).
1001 Cells were stimulated using 25 µl ImmunoCult™ Human CD3/CD28/CD2 T Cell Activator (STEMCELL
1002 Technologies, Vancouver, BC) and seeded on 1.5 x $10^6$ feeder cells, which were derived from healthy
1003 control PBMCs (New York Blood Center, NY) and irradiated at 50 Gy. TILs were incubated at 37°C, 5%
1004 $CO_2$ and maintained by replacement with fresh complete TIL medium every 2 days. After three weeks,
1005 expanded TIL lines were frozen in 10% DMSO (MiliporeSigma, MO), 90% FBS (MiliporeSigma, MO)
1006 and stored in $LN_2$.
1007
1008 **IFN-γ Stimulation of K562 tumors**

1009 Two separate rounds of stimulation were performed on K562 tumors after reaching steady-state
1010 expansion. First, K562 tumors were co-cultured at a concentration of 0.5 X $10^6$ viable cells / mL with 200
1011 and 400 ng / mL of IFN-γ in R10 media in order to assess the induction of HLA-E and PD-L1 with high
1012 doses of IFN-γ. At every 24-hour interval, cell concentration and viability were assessed using a
1013 hemocytometer, and K562 tumors were split to a concentration of 0.5 X $10^6$ live cells / mL. At 72 hours of
1014 incubation, cells were spun at 1650 RPM, washed with FACS buffer (PBS, 5% FBS, 0.2% EDTA),
1015 resuspended in 5 mL of FACS buffer, and assessed for concentration and viability. 0.5 X $10^6$ live cells were
1016 removed, and spun to remove the FACS buffer. K562 tumors were first incubated with zombie near infrared
1017 (NIR) at a dilution of 1 in 1000 for 20 minutes at room temperature. Following the zombie stain, cells were
1018 washed in 1 mL of FACS buffer, and incubated with PD-L1 (PE; Biolegend cat #124308), and HLA-E (per-
1019 CP CY5.5; Biolegend cat #342609) antibodies in a 1:25 dilution cocktail for 30 minutes on ice in the dark.
1020 Cells were washed again in FACS buffer and suspended in 400μLof fixative buffer (2% paraformaldehyde
1021 in PBS). HLA-E and PD-L1 levels were then assessed using flow cytometry.
1022
1023 **TIL Co-culture with K562s Expressing Checkpoints**
1024 For co-culture and surface stain of PD-L1 and HLA-E, three separate K562 tumor lines of K562 cells
1025 were generated using 400 ng/ml of IFN-γ for 72 hours, as described by the protocol listed above: WT, E+,
1026 and E+/PD-L1+ lines. Tumor-infiltrating lymphocytes (TILs) from four BCG-unresponsive NMIBC
1027 patients which had been expanded using the protocol listed above were thawed and seeded at a
1028 concentration of 1 X $10^6$ live cells / mL in a stimulatory media consisting of ImmunoCult, CD3/CD28
1029 tetramer (25 uL/mL), IL-2 (10 IU/mL), IL-7 (10 ng/mL), and IL-15 (10 ng/mL). Cells were seeded and
1030 plated in a 96 round-bottom plate. At days three, five, seven, and nine, 50% of the media was aspirated and
1031 replaced with fresh media at twice the initial concentration of cytokines, without CD3/28 tetramer. At day
1032 10, TGF-β (Immunocult, IL-2 (10IU/mL), IL-7 (10ng/mL), IL-15 (10ng/mL), CD3/CD28 tetramer
1033 (25μL/mL), TGF-β (5ng/mL)) was provided to stimulate expression of NKG2A on the TILS.
1034 At day 13, the stimulation was complete, and the TILs were co-cultured with combinations of the K562
1035 cells expressing forms of PD-L1 and HLA-E. In total, 12 experimental co-culture conditions were
1036 conducted for each patients' TIL sample (n=4): two control wells (ex-vivo, and stimulated with a CD3/28
1037 spike); with K562 WT cells, HLA-$E^+$ cells, or HLA-$E^+$ PD-$L1^+$ cells without antibody; TILs in the presence
1038 of HLA-$E^+$ or HLA-$E^+$PD-$L1^+$ K562s with durvalumab alone, or both durvalumab plus monalizumab; and
1039 lastly, TILs and WT K562s in the presence of monalizumab and durvalumab.
1040 TILs were cultured in TIL medium, consisting of RPMI 1640 with L-glutamine (Corning Inc., NY),
1041 10% human AB serum (MiliporeSigma, MO), 1% nonessential amino acids (Thermo Fisher Scientific,
1042 MA), 1% sodium pyruvate (Thermo Fisher Scientific, MA), 1% penicillin, streptomycin (Thermo Fisher

1043 Scientific, MA). Cultures were performed in 96-well u-bottom plates (Corning Inc., NY). TILs were added
1044 to each well at a concentration of at 3 x$10^5$ cells/condition in TIL medium. K562s were resuspended in TIL
1045 medium and added at 5 x $10^4$ singe-cell equivalents/condition. Anti-CD28 (BioLegend, CA) was added to
1046 each well at 1 μg/ml and anti-CD107a-BV785 (BioLegend, CA) was added to each well at 0.3 μg/ml.
1047 Monalizumab was added to the TILs a final concentration of 10 μg/ml, and durvalumab was added to the
1048 K562s for a final concentration of 10 μg/ml. TILs and K562s were cultured separately for 20 minutes at
1049 37°C prior to co-culture. The K562s and TILs were then combined, thoroughly resuspended, and gently
1050 spun for 5 seconds before being returned to the incubator. Plates were incubated at 37°C and 5% $CO_2$, and
1051 after 1 hour of incubation, 0.5X Brefeldin (BioLegend, CA) and 0.5X Monensin (BioLegend, CA) was
1052 added to each tube for a final volume of 500 μl, followed by an additional 15 hours of incubation. At hour
1053 16 plates were spun and supernatant was removed; all samples were washed with 200μLof PBS. Samples
1054 were resuspended in 50μLof zombie near infrared (NIR) at a 1:3000 dilition, and incubated for 20 minutes
1055 in the dark at room temperature. Samples were washed again, spun, supernatant was removed, and
1056 incubated in 50μLof TruStain FCX, diluted 1:200, for 20 minutes in the dark at 4°C. 50μLof the surface
1057 antibody master mix was added at 20 minutes, and returned to the fridge to incubate in the dark at 4°C for
1058 30 more minutes. Plates were washed twice more in FACS buffer, and were suspended in 0.2% FBS FACS
1059 buffer for storage until intracellular staining.
1060 12 hours prior to acquisition by CyTOF, intracellular staining was performed for IFN-γ. 100 μL of
1061 intracellular staining permeabilization wash buffer (BioLegend) was added to each well, the plates were
1062 spun, and supernatant discarded. This was performed 2 additional times with 200 μL of permeabilization
1063 wash buffer. 50 μL of the intracellular staining antibody mix was added to each well, and the plates were
1064 incubated for 20 minutes at 4°C. The plates were washed in 0.2% FBS FACS buffer and resuspended for
1065 storage in 0.2% FBS FACS buffer.
1066
1067 **Data Availability Statement**: data were generated by the authors and have been uploaded to the Gene
1068 Expression Omnibus (GSE276014 and GSE276015) and will be made publicly available upon publication
1069 of this manuscript.
1070
1071 **ACKNOWLEDGMENTS**
1072 We thank Mary Anne O'Donnell (Precision Immunology Institute, Icahn School of Medicine at Mount
1073 Sinai) for critically reviewing the manuscript; Deepta Bhattacharya ´(University of Arizona) for kindly
1074 providing HLA-$E^+$ K562 tumors. We acknowledge the expertise and assistance of the Dean's Flow
1075 Cytometry Center of Research Excellence at Mount Sinai. The A.H. and J.P. labs were supported by funding

from P30CA196521, R01 CA269954-01, R21 CA274148, BCAN No. 961726, and R21AI130760A. The N.B. lab was supported by funding from the Department of Defense Peer Review Cancer Research program Translational team Award No. W81XWH1910269 and from the Parker Institute for Cancer Immunotherapy No.AGR-11611SOW1.

## AUTHOR CONTRIBUTIONS

D.R., H.Y., Y.A.W., C.B., J.D., B.S., M.G., N.B., J.P.S., and A.H. conceived the project and experiments, analyzed the data and wrote the manuscript. J.P.S., R.M., P.W., M.G., and R.B. provided access to the human samples. Additionally, L.D. provided analyses on data derived from human samples at Aarhus University Hospital. D.R., H.Y., Y.A.W., C.B., A.D., S.B.,W-M.S., J.D., B.S., D-F.R., F.P. E.M., A.T., J-A.C-F., B.D.H., T.S., S.V.L., S.H., J.K., performed the experiments or analyzed data. A.M.F, M.T., J.Z., K.G.B, L.W, R.P.S, S.S, Y-C.W, and Y.A.W. collected the RNA sequencing data. D.G., G.K., R.M.d-R, B.L., S.K-S. acquired sample data using mass cytometry and Olink proteomics. T.H.T, M.G-B, R.B., E.H-S, E.M.M, C.B., R.F-G, M.S, H.R, A.N., G.D., and J.J.B-C. performed the imaging experiments. S.S., E.C-T., D.P., and S.H. provided intellectual input.

## DECLARATION OF INTERESTS

L.W., R.P.S., and J.Z. are employees of Sema4. A.H. receives research funds from Astra Zeneca and has recently served on the advisory boards of Immunorizon, Purple BiotechUroGen, and Takeda. N.B. is an extramural member of the Parker Institute for Cancer Immunotherapy, receives research funds from Regeneron, Harbor Biomedical, DC Prime, and Dragonfly Therapeutics and is on the advisory boards of Neon Therapeutics, Novartis, Avidea, Boehringer Ingelheim, Rome Therapeutics, Rubius Therapeutics, Roswell Park Comprehensive Cancer Center, BreakBio, Carisma Therapeutics, CureVac, Genotwin, BioNTech, Gilead Therapeutics, Tempest Therapeutics, and the Cancer Research Institute.

## LEGENDS TO FIGURES

**Fig. 1: Chronic activation within the tumor microenvironment of BCG-unresponsive tumors promotes adaptive resistance**.

**A,** Targeted mRNA gene-set enrichment analysis showing statistically significant differences between BCG-naïve (N=20) and BCG-unresponsive cases (N=20). All gene sets are significant at $p<0.05$ by Kruskal-Wallis or independent two-sided t-test.

1108 **B,** Longitudinal protein analysis of urine supernatants across four timepoints in BCG-naïve patients with
1109 NMIBC (N=27) with comparisons between BCG-naïve and 6th induction dose timepoints (* $p<0.05$, **
1110 $p<0.001$).
1111 **C,** An additional validation cohort of patients with NMIBC receiving BCG therapy at Aarhus University
1112 (N=66) showing BCG-naïve vs BCG-exposed timepoints in urine samples (p-values in both cohorts
1113 assessed via independent two-sided t-test or Kruskal-Wallis with Benjamini-Hochberg correction for
1114 multiple comparisons).
1115 **D,** Differential protein expression analysis of urine before (top row) and after (bottom row) BCG exposure
1116 and sampled before (left-side) and after (right-side) transurethral resection of bladder tumors. Number of
1117 patients included in analyses: (Top-left) BCG-naïve when tumor present, non-responders, N= 47;
1118 responders, N= 60. (Top-right) BCG-naïve after tumor resection, non-responders, N= 5; responders, N= 6.
1119 (Bottom-left) BCG-exposed when tumor present, non-responders, N= 49; responders, N= 34. (Bottom-
1120 right) BCG-exposed after tumor-resection, non-responders, N= 19; responders, N= 26. P-values assessed
1121 with two-sided Wilcoxon rank sum. Proteins listed in orange text indicate unadjusted p-values <0.05. BCG-
1122 unresponsive NMIBC was defined as high-grade recurrence within two years after receiving BCG therapy.
1123 **E,** Median fluorescence intensity (MFI) for PD-L1 and HLA-E staining on primary CD45- cells from
1124 patients with NMIBC and immortalized bladder tumor lines ex vivo or after 24 hours of incubation with
1125 recombinant human (rh) IFN-g stimulation (all comparisons, $p<0.05$). All stimulation experiments were
1126 performed in triplicate.
1127
1128 **Fig: 2: HLA-E tumor expression is highest when near tumor-infiltrating NKG2A$^+$ NK and CD8 T**
1129 **cells**.
1130 **A,** Representative multiplexed immunofluorescence (IF) analysis by PhenoCycler™ (also known as
1131 CODEX) of bladder tumor sections from one patient with BCG-unresponsive NMIBC. Representative
1132 staining of the entire section is shown for presence of stroma (vimentin, blue) and tumor (S100A4, yellow).
1133 Scale bar indicates 2mm.
1134 **B,** Magnified inset from Panel A, highlighting tumor HLA-E expression of and use of digital pathology
1135 software to identify NKp46$^+$ NK and CD8 T cells with and without co-expression of NKG2A +/- PD-1.
1136 Left image scale bar indicates 400μm and right image scale bar indicates 50μm.
1137 **C,** Magnified inset from Panel B, right image, highlighting individual cells expressing CD8, PD-1, and
1138 NKG2A. Scale bars indicate 20μm.

1139 **D,** Representative multiplexed immunohistochemistry (IHC) of bladder tumor from one patient with BCG-
1140 unresponsive NMIBC measuring expression of pan-cytokeratin (pan-CK), HLA-E, CD3, and NKG2A.
1141 Scale bar indicates 100μm.
1142 **E,** Representative digital pathology analyses identifying tumor (red) and adjacent/non-tumor (green) tissue
1143 along with exposed areas of glass (yellow) to be excluded from subsequent analyses. Scale bar indicates
1144 1mm.
1145 **F,** Density map highlighting regions of high HLA-E tumor expression. Blue-red color scale indicates HLA-
1146 E expression intensity. Scale bar indicates 1mm.
1147 **G,** Summary analysis of frequency of tumor cells that are HLA-E-bright (green) and HLA-E-dim/negative
1148 (dim/neg, yellow) in BCG-naïve (N=17) and BCG-unresponsive (unresp., N=24) NMIBC tumors.
1149 **H,** Representative digital pathology analysis on one BCG-naïve (top row) and one BCG-unresponsive
1150 (bottom row) NMIBC tumor section highlighting nuclear expression of DAPI (blue) and identification of
1151 $CD3^{+}NKG2A^{+}$ CD8 T cells (black), CD3- $NKG2A^{+}$ NK cells (red), and tumor cells with bright (green) or
1152 dim/negative (yellow) expression of HLA-E.
1153 **I,** Proximity analysis (N=41) measuring cell distance (0-150μm) from HLA-E-bright and HLA-E-
1154 dim/negative tumors by NKG2A+ NK cells (left side) and NKG2A+ T cells (right side). ****, $p<0.00001$.
1155 P-values were assessed via independent two-sided t-test.
1156 **J,** Representative proximity ligation assay (PLA) using immunofluorescence to profile interactions between
1157 HLA-E and NKG2A in one BCG-naïve (top row) and one BCG-unresponsive (bottom row) patient with
1158 NMIBC.
1159 **K,** Summary analysis of PLA measuring interactions between HLA-E and NKG2A. P-values were assessed
1160 via independent two-sided t-test.
1161
1162
1163 **Fig. 3: Single-cell RNA sequencing analysis of $NKG2A^{+}$ NK and CD8 T cells from bladder tumors**
1164 **reveals strong antitumor potential but with co-expression of inhibitory receptors**.
1165 **A,** UMAP visualization of cell lineages from single-cell RNA sequencing analysis of urothelial tumor samples (N=9,
1166 65,324 cells).
1167 **B,** Heatmap summary of genes most differentially expressed on each cell lineage identified.
1168 **C,** Differentially expressed gene (DEG) analysis of bladder tumor-derived NK cells (left), CD8 T cells
1169 (center), and proliferating T cell cycle cells (right) when stratified by high versus dim/negative *KLRC1*
1170 expression.

1171 **D** and **E,** UMAP visualizations of bladder tumor-derived NK cells from unsupervised clustering revealing
1172 (**D**) five clusters or (**E**) expression of *NCAM1*/CD56 for annotation of $CD56^{BRIGHT}$ and $CD56^{DIM}$ NK cells
1173 (N=2,580 cells).
1174 **F,** Pathway analysis of Hallmark gene networks that are significantly differentially expressed (at least
1175 $p<0.05$) on bladder tumor-derived $CD56^{BRIGHT}$ and $CD56^{DIM}$ NK cells. P-values were determined using a
1176 two-sided t-test.
1177 **G** and **H,** UMAP visualization of bladder tumor-derived NK cells (**G**) clustered according to Groups 1-6
1178 defined by Netskar et al. [30] and (**H**) highlighting expression and distribution of representative tissue
1179 residency genes.
1180 **I,** Heatmap summary showing average expression for genes associated with tissue residency, chemokines,
1181 cytokines, and their receptors on bladder tumor-derived Group 1-6 NK cells (top heatmap) and CD8 T cells
1182 and T cell cycle cells when stratified according to *KLRC1* expression (bottom heatmap).
1183
1184 **Fig. 4: Single-cell RNA sequencing analysis of bladder tumor cells reveals functional differences that**
1185 **segregate the tumor microenvironment**.
1186 **A,** UMAP visualization of bladder tumor cells from unsupervised clustering revealing seven clusters (B1-
1187 B7).
1188 **B,** UMAP visualization of HLA-E expression defined by tertiles, highlighting the top tertile (red dots) as
1189 HLA-E-bright (N=5,461) and bottom tertile (blue dots) as HLA-E-dim/negative (N=9,256) tumor cells.
1190 **C,** Pathway analysis of Hallmark gene networks that are significantly differentially expressed (at least
1191 $p<0.05$) on HLA-E-bright and HLA-E-dim/negative bladder tumor cells. P-values were determined using
1192 a two-sided t-test.
1193 **D,** Bubble plot showing targeted gene expression across bladder tumor clusters B1-B7 and stratified by
1194 *HLA-E*$^{HIGH}$ or *HLA-E*$^{LOW}$ tumor clusters. Size of bubble indicates percent of cluster or group and color
1195 indicates average gene expression.
1196 **E,** Scatterplot highlighting pseudobulking of bladder tumor cells and expression of *HLA-E* and *ACKR3*
1197 (CXCR7). P-value was determined using a two-sided correlation.
1198 **F,** Stacked bar plot showing the frequency of bladder tumor clusters, B1-B7 that are identified in BCG-
1199 naïve (green) and BCG-unresponsive (grey) NMIBC tumors.
1200 **G,** Heatmap summary of average gene expression of select chemokines, chemokine receptors, amphiregulin
1201 (*AREG*) and *EGFR* across all major clusters identified by scRNAseq of bladder tumors (N=9, 65,324 cells).
1202 **H,** Ligand-receptor interaction analysis of *KLRC1*$^{HIGH}$ cells (NK cells, CD8 T cells, T cell cycle) and *HLA-*
1203 *E*-bright tumor cells (schematic diagram at top) showing the top 12 ranked ligands by KLRC1-expressing

1204 cells and cognate receptors expressed by *HLA-E*$^{HIGH}$ tumor cells. Ligand-receptor pairs were selected by
1205 rank-ordering and using cut-off weight of 0.2.
1206 **I,** Circos plot showing top ranked ligands by KLRC1-expressing cells at the bottom and significant genes
1207 expressed by *HLA-E*$^{HIGH}$ tumor cells as a result of ligand-receptor interactions highlighting putative effects
1208 of the HLA-E/NKG2A axis (top) or the *IFNG*-mediated (middle) or *AREG*-mediated (bottom) resistance
1209 signatures.
1210
1211 **Fig. 5: Spatial analysis of NMIBC tumors reveals an organization within the TME**.
1212 **A** and **B,** UMAP visualization of spatial transcriptomics sequencing (ST-seq) analysis of BCG-naïve (N=4)
1213 and BCG-unresponsive (N=4) NMIBC tumors identifying 12 ST-clusters and their distributions across
1214 NMIBC specimens.
1215 **C**, Bubble plot showing ST-clusters 1-11 (rows) and their relative composition across immune, stromal,
1216 and tumor subtypes (columns) as defined by scRNAseq analysis. Size of bubble indicates its relative
1217 enrichment and shading of surrounding boxes indicate significance by FDR (corrected p values).
1218 **D,** Representative ST-seq images showing the distribution of ST-clusters 1-11 in one BCG-naïve (left) and
1219 one BCG-unresponsive (right) NMIBC tumor specimens.
1220 **E,** Summary histogram comparing relative enrichment of each ST-cluster in BCG-naïve (grey, N=4) and
1221 BCG-unresponsive (green, N=4) NMIBC tumor specimens.
1222 **F,** Schematic diagram illustrating deconvolution of NK cells and tumor cells across 10x Visium spots.
1223 Cutoff of 20% of spot's composition was used for defining a true signal.
1224 **G** and **H,** Representative ST-seq images from one BCG-naïve (left) and one BCG-unresponsive (right)
1225 NMIBC tumor specimens showing proximity analyses of *HLA-E*$^{LOW}$ (black circles) and *HLA-E*$^{HIGH}$ (red
1226 circles) tumor cells to (**G**) NK/CD8 T cells (blue spots) or (H) NK cells, CD8 T cells, and Tregs alone or
1227 in combination (colored spots).
1228 **I,** Summary comparisons of proximity of *HLA-E*$^{HIGH}$ (red bars) and *HLA-E*$^{LOW}$ (grey bars) tumor cells to
1229 NK cells (left), Tregs (middle) and CD8 T cells (right). P-values were determined using two-sided
1230 Wilcoxon test.
1231
1232 **Fig. 6: Recruitment of *HLA-E*$^{HIGH}$ tumor cells to stromal regions replete with immune infiltration**
1233 **correlates with BCG-unresponsive NMIBC**.
1234 **A-C**, Representative ST-seq images from one BCG-unresponsive NMIBC tumor highlighting (**A**)
1235 proximity of NK cells, CD8 T cells, and Tregs to tumor and stromal cells according to *HLA-E* expression,
1236 (**B**) overlaid topographical map of *HLA-E* tumor/stromal cell expression with color indicating abundance

1237 of NK and cytolytic CD8 T cells, and (**C**) proximity of NK cells, CD8 T cells, and Tregs to myeloid cells
1238 expressing any combination of *CXCL9*, *CXCL10*, and/or *CXCL11*.
1239 **D,** Correlation analysis of Visium spots, defined as tumor cell with or without stromal cells, for co-
1240 expression of *CXCL9* and *HLA-E* expression in BCG-naïve (N=4, left) and BCG-unresponsive (N=4, right)
1241 NMIBC tumor specimens.
1242 **E,** Correlation analysis of Visium spots, defined as tumor cell with or without stromal cells, for co-
1243 expression of *CXCL12* and *HLA-E* expression in BCG-naïve (N=4, left) and BCG-unresponsive (N=4,
1244 right) NMIBC tumor specimens.
1245 **F,** Meta-analysis of all tumor/stroma-labelled Visium spots showing row-scaled expression of pertinent genes
1246 stratified by number of neighboring infiltrating NK cells and/or CD8 T-cells.
1247 **G,** Z-scored heatmap showing *HLA-E*$^{LOW}$, low-cytotoxic infiltrating tumor spots (N = 1,200 Visium spots) vs HLA-
1248 E$^{HIGH}$ and high-NK/CD8 T cell-infiltrated tumor spots (N = 242 Visium spots).
1249 **H,** Representative multiplexed IF analysis by PhenoCycler™ of bladder tumor sections from one patient
1250 with BCG-unresponsive NMIBC highlighting the presence of stroma (vimentin, blue) and tumor (S100A4,
1251 yellow). Scale bar indicates 2mm.
1252 **I,** Magnified inset from Panel H, highlighting tumor S100A4 expression of and use of digital pathology
1253 software to identify NKG2A$^{+}$ NK and CD8 T cells along FoxP3+ CD4+ Tregs, macrophages (CD68 and
1254 CD163) and dendritic cells (CD11c and/or HLA-DR). Image scale bar indicates 20μm.
1255
1256 **Fig. 7: In vitro combination NKG2A and PD-L1 blockade restores tumor-derived NK and CD8 T**
1257 **cell-mediated antitumor activity.**
1258 **A,** Median fluorescence intensity (MFI) of HLA-E and PD-L1 expression by wild-type (WT) or HLA-E$^{+}$
1259 K562 tumors cultured overnight in the presence or absence of recombinant human IFN-γ.
1260 **B and C,** Phenograph clustering meta-analysis of tumor-derived and expanded CD56$^{+}$ CD8 T cells by
1261 CyTOF before co-culture with K562 tumors showing **B,** tSNE analysis of identified CD8 T cell clusters,
1262 and **C,** expression of individual inhibitory and activating receptors by CD8 T cells and their distribution
1263 across clusters.
1264 **D,** Representative CyTOF analysis of CD56 and NKG2A expression on tumor-derived NK (top row) and
1265 CD8 T cells (bottom row) profiled before (left column) and after (right column) expansion with low dose
1266 recombinant human IL-2, IL-7, IL-15 and CD3/CD28 tetramers.
1267 **E,** Representative fluorescence flow cytometric analysis of IFN-g and CD107a expression by CD56$^{+}$ NK
1268 (top row) and CD8 T cells (bottom row) after 6-hour culture alone or in presence of K562 tumor lines with
1269 or without pre-treatment with anti-PD-L1 antibodies or with anti-PD-L1 + anti-NKG2A antibodies.

1270 **F,** Fold-change differences between the frequencies of NK and $CD56^+$ CD8 T cells when comparing
1271 between experimental conditions (defined by "+"). Individual comparisons are indicated at the bottom. *,
1272 $p< 0.05$; **, $p< 0.001$. P values determined by paired Wilcoxon matched rank test.
1273
1274

1277 **References**


1278 1. Redelman-Sidi, G., Glickman, M.S. & Bochner, B.H. The mechanism of action of BCG
1279 therapy for bladder cancer--a current perspective. *Nat Rev Urol* **11**, 153-162 (2014).
1280
1281 2. Kamat, A.M. *et al.* Predicting Response to Intravesical Bacillus Calmette-Guerin
1282 Immunotherapy: Are We There Yet? A Systematic Review. *Eur Urol* **73**, 738-748 (2018).
1283
1284 3. Müller, G. *et al.* Association between Development of Metabolic Acidosis and
1285 Improvement of Urinary Continence after Ileal Neobladder Creation. *J Urol* **203**, 585-590
1286 (2020).
1287
1288 4. Hedgepeth, R.C., Gilbert, S.M., He, C., Lee, C.T. & Wood, D.P., Jr. Body image and bladder
1289 cancer specific quality of life in patients with ileal conduit and neobladder urinary
1290 diversions. *Urology* **76**, 671-675 (2010).
1291
1292 5. Morales, A. BCG: A throwback from the stone age of vaccines opened the path for bladder
1293 cancer immunotherapy. *Can J Urol* **24**, 8788-8793 (2017).
1294
1295 6. Zlotta, A.R. *et al.* What is the optimal regimen for BCG intravesical therapy? Are six weekly
1296 instillations necessary? *Eur Urol* **37**, 470-477 (2000).
1297
1298 7. Sfakianos, J.P. *et al.* Bacillus Calmette-Guerin (BCG): Its fight against pathogens and cancer.
1299 *Urol Oncol* **39**, 121-129 (2021).
1300
1301 8. Sharma, P., Hu-Lieskovan, S., Wargo, J.A. & Ribas, A. Primary, Adaptive, and Acquired
1302 Resistance to Cancer Immunotherapy. *Cell* **168**, 707-723 (2017).
1303
1304 9. Gocher, A.M., Workman, C.J. & Vignali, D.A.A. Interferon-γ: teammate or opponent in the
1305 tumour microenvironment? *Nat Rev Immunol* (2021).
1306
1307 10. Benci, J.L. *et al.* Opposing Functions of Interferon Coordinate Adaptive and Innate Immune
1308 Responses to Cancer Immune Checkpoint Blockade. *Cell* **178**, 933-948.e914 (2019).
1309
1310 11. Wang, L. *et al.* Myeloid Cell-associated Resistance to PD-1/PD-L1 Blockade in Urothelial
1311 Cancer Revealed Through Bulk and Single-cell RNA Sequencing. *Clin Cancer Res* (2021).
1312
1313 12. Strandgaard, T. *et al.* Field Cancerization Is Associated with Tumor Development, T-cell
1314 Exhaustion, and Clinical Outcomes in Bladder Cancer. *Eur Urol* (2023).
1315
1316 13. Strandgaard, T. *et al.* Elevated T-cell Exhaustion and Urinary Tumor DNA Levels Are
1317 Associated with Bacillus Calmette-Guérin Failure in Patients with Non–muscle-invasive
1318 Bladder Cancer. *European Urology* (2022).
1319

14. Kates, M. *et al.* Adaptive Immune Resistance to Intravesical BCG in Non-Muscle Invasive Bladder Cancer: Implications for Prospective BCG-Unresponsive Trials. *Clin Cancer Res* **26**, 882-891 (2020).

15. Rosenberg, J.E. *et al.* Atezolizumab in patients with locally advanced and metastatic urothelial carcinoma who have progressed following treatment with platinum-based chemotherapy: a single-arm, multicentre, phase 2 trial. *Lancet* **387**, 1909-1920 (2016).

16. Powles, T. *et al.* Efficacy and Safety of Durvalumab in Locally Advanced or Metastatic Urothelial Carcinoma: Updated Results From a Phase 1/2 Open-label Study. *JAMA Oncol* **3**, e172411 (2017).

17. Sharma, P. *et al.* Nivolumab in metastatic urothelial carcinoma after platinum therapy (CheckMate 275): a multicentre, single-arm, phase 2 trial. *Lancet Oncol* **18**, 312-322 (2017).

18. Patel, M.R. *et al.* Avelumab in metastatic urothelial carcinoma after platinum failure (JAVELIN Solid Tumor): pooled results from two expansion cohorts of an open-label, phase 1 trial. *Lancet Oncol* **19**, 51-64 (2018).

19. Grossman, J.E., Vasudevan, D., Joyce, C.E. & Hildago, M. Is PD-L1 a consistent biomarker for anti-PD-1 therapy? The model of balstilimab in a virally-driven tumor. *Oncogene* **40**, 1393-1395 (2021).

20. Kamiya, T., Seow, S.V., Wong, D., Robinson, M. & Campana, D. Blocking expression of inhibitory receptor NKG2A overcomes tumor resistance to NK cells. *J Clin Invest* **129**, 2094-2106 (2019).

21. Pereira, B.I. *et al.* Senescent cells evade immune clearance via HLA-E-mediated NK and CD8(+) T cell inhibition. *Nat Commun* **10**, 2387 (2019).

22. van Montfoort, N. *et al.* NKG2A Blockade Potentiates CD8 T Cell Immunity Induced by Cancer Vaccines. *Cell* **175**, 1744-1755.e1715 (2018).

23. Andre, P. *et al.* Anti-NKG2A mAb Is a Checkpoint Inhibitor that Promotes Anti-tumor Immunity by Unleashing Both T and NK Cells. *Cell* **175**, 1731-1743 e1713 (2018).

24. Salomé, B. *et al.* NKG2A and HLA-E define a novel alternative immune checkpoint axis in bladder cancer. *Cancer Cell* **40**, 1-17 (2022).

25. Herbst, R.S. *et al.* COAST: An Open-Label, Phase II, Multidrug Platform Study of Durvalumab Alone or in Combination With Oleclumab or Monalizumab in Patients With Unresectable, Stage III Non-Small-Cell Lung Cancer. *J Clin Oncol*, JCO2200227 (2022).

26. Rouanne, M. *et al.* BCG therapy downregulates HLA-I on malignant cells to subvert antitumor immune responses in bladder cancer. *J Clin Invest* **132** (2022).

27. Liberzon, A. *et al.* The Molecular Signatures Database (MSigDB) hallmark gene set collection. *Cell Syst* **1**, 417-425 (2015).

28. Jiang, Y.H. *et al.* Urine cytokines as biomarkers for diagnosing interstitial cystitis/bladder pain syndrome and mapping its clinical characteristics. *Am J Physiol Renal Physiol* **318**, F1391-f1399 (2020).

29. Tyagi, P. *et al.* Urine cytokines suggest an inflammatory response in the overactive bladder: a pilot study. *Int Urol Nephrol* **42**, 629-635 (2010).

30. Netskar, H. *et al.* Pan-cancer profiling of tumor-infiltrating natural killer cells through transcriptional reference mapping. *Nat Immunol* (2024).

31. Rebuffet, L. *et al.* High-dimensional single-cell analysis of human natural killer cell heterogeneity. *Nat Immunol* (2024).

32. Vivier, E. *et al.* Natural killer cell therapies. *Nature* **626**, 727-736 (2024).

33. Browaeys, R., Saelens, W. & Saeys, Y. NicheNet: modeling intercellular communication by linking ligands to target genes. *Nat Methods* **17**, 159-162 (2020).

34. Amir el, A.D. *et al.* viSNE enables visualization of high dimensional single-cell data and reveals phenotypic heterogeneity of leukemia. *Nat Biotechnol* **31**, 545-552 (2013).

35. Cristescu, R. *et al.* Pan-tumor genomic biomarkers for PD-1 checkpoint blockade-based immunotherapy. *Science* **362** (2018).

36. Spranger, S. *et al.* Up-regulation of PD-L1, IDO, and T(regs) in the melanoma tumor microenvironment is driven by CD8(+) T cells. *Sci Transl Med* **5**, 200ra116-200ra116 (2013).

37. Rooney, M.S., Shukla, S.A., Wu, C.J., Getz, G. & Hacohen, N. Molecular and genetic properties of tumors associated with local immune cytolytic activity. *Cell* **160**, 48-61 (2015).

38. Ribas, A. Adaptive Immune Resistance: How Cancer Protects from Immune Attack. *Cancer Discov* **5**, 915-919 (2015).

39. Grasso, C.S. *et al.* Conserved Interferon-γ Signaling Drives Clinical Response to Immune Checkpoint Blockade Therapy in Melanoma. *Cancer Cell* **38**, 500-515.e503 (2020).

40. Gocher, A.M., Workman, C.J. & Vignali, D.A.A. Interferon-γ: teammate or opponent in the tumour microenvironment? *Nat Rev Immunol* **22**, 158-172 (2022).

41. Bardia, A. *et al.* Sacituzumab Govitecan in Metastatic Triple-Negative Breast Cancer. *N Engl J Med* **384**, 1529-1541 (2021).

42. Powles, T. *et al.* Enfortumab Vedotin and Pembrolizumab in Untreated Advanced Urothelial Cancer. *N Engl J Med* **390**, 875-888 (2024).

43. Heath, E.I. & Rosenberg, J.E. The biology and rationale of targeting nectin-4 in urothelial carcinoma. *Nat Rev Urol* **18**, 93-103 (2021).

44. Chang, S.S. *et al.* Diagnosis and Treatment of Non-Muscle Invasive Bladder Cancer: AUA/SUO Guideline. *J Urol* **196**, 1021-1029 (2016).

45. Bisiaux, A. *et al.* Molecular analyte profiling of the early events and tissue conditioning following intravesical bacillus calmette-guerin therapy in patients with superficial bladder cancer. *J Urol* **181**, 1571-1580 (2009).

46. Shapiro, S.S. & Wilk, M.B. An Analysis of Variance Test for Normality (Complete Samples). *Biometrika* **52**, 591-611 (1965).

47. Kruskal, W.H. & Wallis, W.A. Use of Ranks in One-Criterion Variance Analysis. *Journal of the American Statistical Association* **47**, 583-621 (1952).

48. Zhang, X. *et al.* CellMarker: a manually curated resource of cell markers in human and mouse. *Nucleic Acids Res* **47**, D721-d728 (2019).

49. Glass, D.R. *et al.* An Integrated Multi-omic Single-Cell Atlas of Human B Cell Identity. *Immunity* **53**, 217-232.e215 (2020).

50. Magri, G. *et al.* Human Secretory IgM Emerges from Plasma Cells Clonally Related to Gut Memory B Cells and Targets Highly Diverse Commensals. *Immunity* **47**, 118-134.e118 (2017).

51. Hao, Y. *et al.* Dictionary learning for integrative, multimodal and scalable single-cell analysis. *Nature biotechnology* **42**, 293-304 (2024).

52. Finak, G. *et al.* MAST: a flexible statistical framework for assessing transcriptional changes and characterizing heterogeneity in single-cell RNA sequencing data. *Genome biology* **16**, 1-13 (2015).

53. Liberzon, A. *et al.* Molecular signatures database (MSigDB) 3.0. *Bioinformatics* **27**, 1739-1740 (2011).

54. Rouillard, A.D. *et al.* The harmonizome: a collection of processed datasets gathered to serve and mine knowledge about genes and proteins. *Database (Oxford)* **2016** (2016).

55. Galon, J. *et al.* Affinity of the interaction between Fc gamma receptor type III (Fc gammaRIII) and monomeric human IgG subclasses. Role of Fc gammaRIII glycosylation. *Eur J Immunol* **27**, 1928-1932 (1997).

56. Liberzon, A. *et al.* Molecular signatures database (MSigDB) 3.0. *Bioinformatics* **27**, 1739-1740 (2011).

57. Dries, R. *et al.* Giotto: a toolbox for integrative analysis and visualization of spatial expression data. *Genome biology* **22**, 1-31 (2021).

58. Lause, J., Berens, P. & Kobak, D. Analytic Pearson residuals for normalization of single-cell RNA-seq UMI data. *Genome biology* **22**, 1-20 (2021).

59. Korsunsky, I. *et al.* Fast, sensitive and accurate integration of single-cell data with Harmony. *Nature methods* **16**, 1289-1296 (2019).

60. Ma, Y. & Zhou, X. Spatially informed cell-type deconvolution for spatial transcriptomics. *Nature biotechnology* **40**, 1349-1359 (2022).

61. Jin, S., Plikus, M.V. & Nie, Q. CellChat for systematic analysis of cell-cell communication from single-cell and spatially resolved transcriptomics. *BioRxiv*, 2023.2011. 2005.565674 (2023).

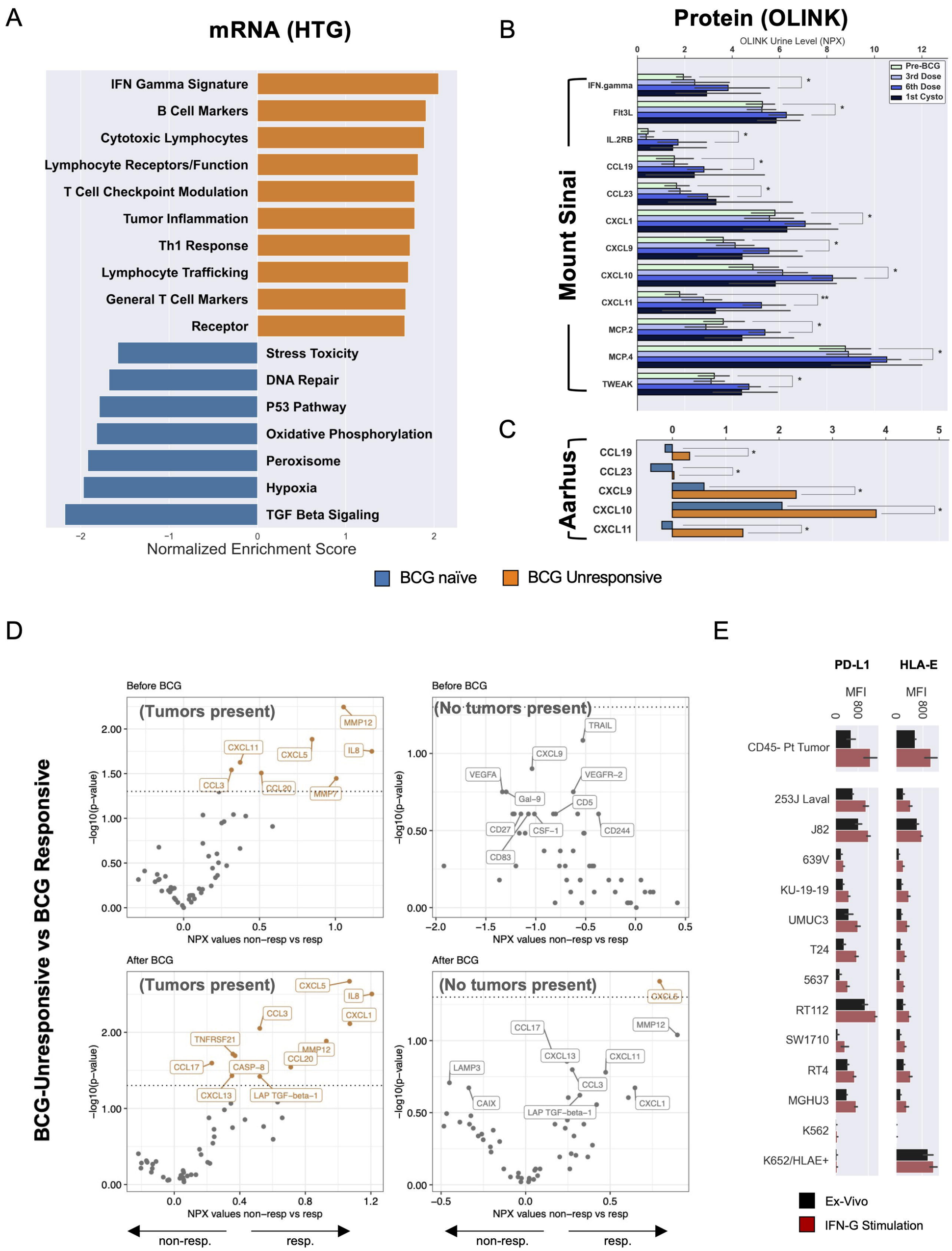
A
mRNA (HTG)
IFN Gamma Signature
B Cell Markers
Cytotoxic Lymphocytes
Lymphocyte Receptors/Function
T Cell Checkpoint Modulation
Tumor Inflammation
Th1 Response
Lymphocyte Trafficking
General T Cell Markers
Receptor
Stress Toxicity
DNA Repair
P53 Pathway
Oxidative Phosphorylation
Peroxisome
Hypoxia
TGF Beta Sigaling
Normalized Enrichment Score
BCG naïve
BCG Unresponsive
B
Protein (OLINK)
OLINK Urine Level (NPX)
Pre-BCG
3rd Dose
6th Dose
1st Cysto
Mount Sinai
IFN.gamma
Flt3L
IL.2RB
CCL19
CCL23
CXCL1
CXCL9
CXCL10
CXCL11
MCP.2
MCP.4
TWEAK
C
Aarhus
CCL19
CCL23
CXCL9
CXCL10
CXCL11
D
BCG-Unresponsive vs BCG Responsive
Before BCG
(Tumors present)
(No tumors present)
After BCG
NPX values non–resp vs resp
−log10(p−value)
MMP12
CXCL11
CXCL5
IL8
CCL3
CCL20
MMP7
TRAIL
CXCL9
VEGFA
VEGFR−2
Gal−9
CD5
CD27
CSF−1
CD244
CD83
TNFRSF21
CCL17
CASP−8
CXCL13
LAP TGF−beta−1
CXCL1
LAMP3
CAIX
non-resp.
resp.
E
PD-L1
HLA-E
MFI
CD45- Pt Tumor
253J Laval
J82
639V
KU-19-19
UMUC3
T24
5637
RT112
SW1710
RT4
MGHU3
K562
K652/HLAE+
Ex-Vivo
IFN-G Stimulation

Figure 1.

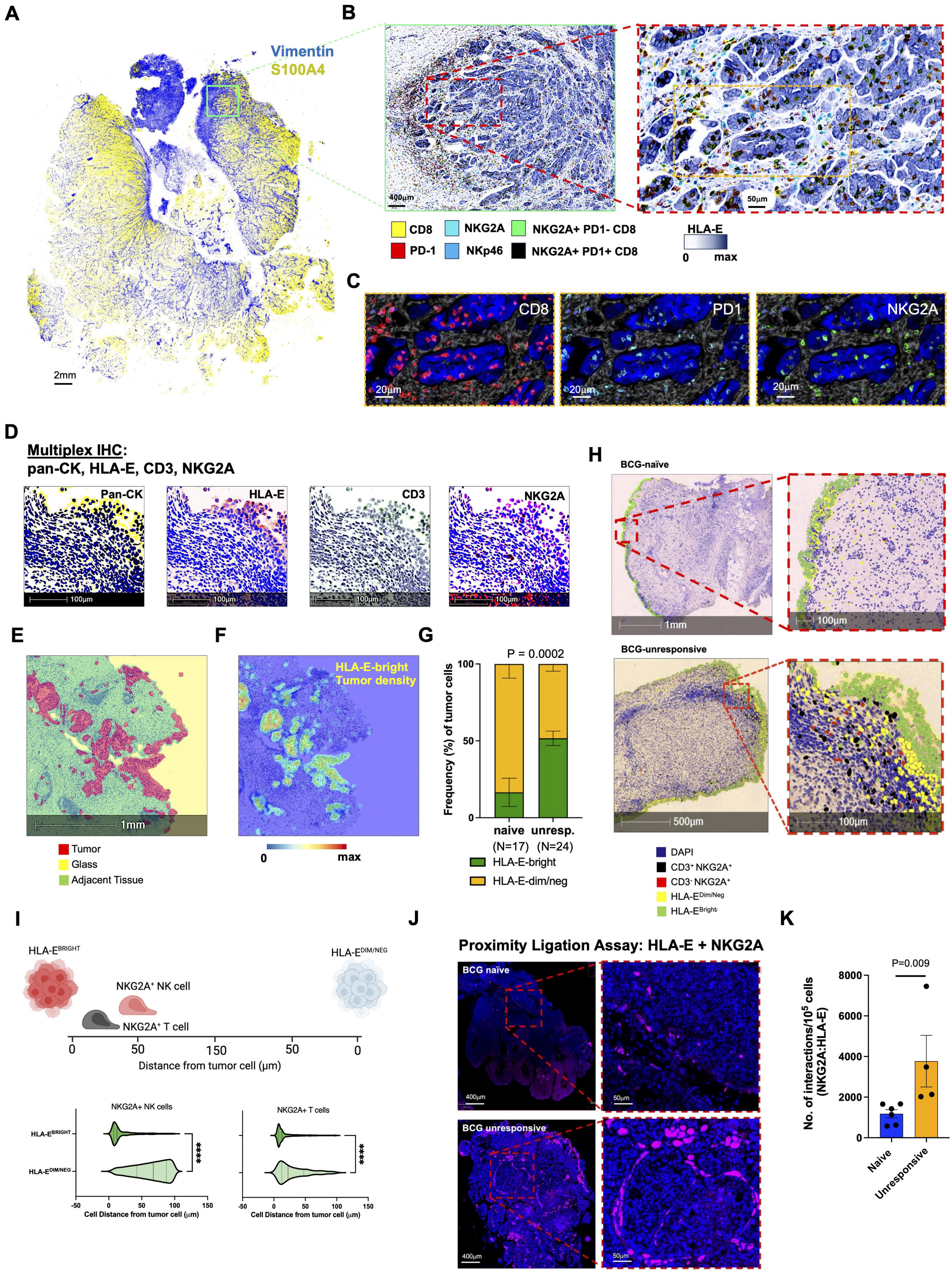
A
Vimentin
S100A4
2mm
B
400µm
50µm
CD8
NKG2A
NKG2A+ PD1- CD8
PD-1
NKp46
NKG2A+ PD1+ CD8
HLA-E
0
max
C
CD8
PD1
NKG2A
20µm
D
Multiplex IHC:
pan-CK, HLA-E, CD3, NKG2A
Pan-CK
HLA-E
CD3
NKG2A
100µm
E
1mm
Tumor
Glass
Adjacent Tissue
F
HLA-E-bright
Tumor density
0
max
G
P = 0.0002
Frequency (%) of tumor cells
100
50
0
naive
unresp.
(N=17)
(N=24)
HLA-E-bright
HLA-E-dim/neg
H
BCG-naïve
1mm
100µm
BCG-unresponsive
500µm
DAPI
CD3+ NKG2A+
CD3- NKG2A+
HLA-EDim/Neg
HLA-EBright/
I
HLA-EBRIGHT
HLA-EDIM/NEG
NKG2A+ NK cell
NKG2A+ T cell
0
50
150
50
0
Distance from tumor cell (µm)
NKG2A+ NK cells
NKG2A+ T cells
HLA-EBRIGHT
HLA-EDIM/NEG
****
-50
0
50
100
150
Cell Distance from tumor cell (µm)
J
Proximity Ligation Assay: HLA-E + NKG2A
BCG naïve
BCG unresponsive
400µm
50µm
K
P=0.009
No. of interactions/10^5 cells
(NKG2A:HLA-E)
8000
6000
4000
2000
0
Naive
Unresponsive

Figure 2.

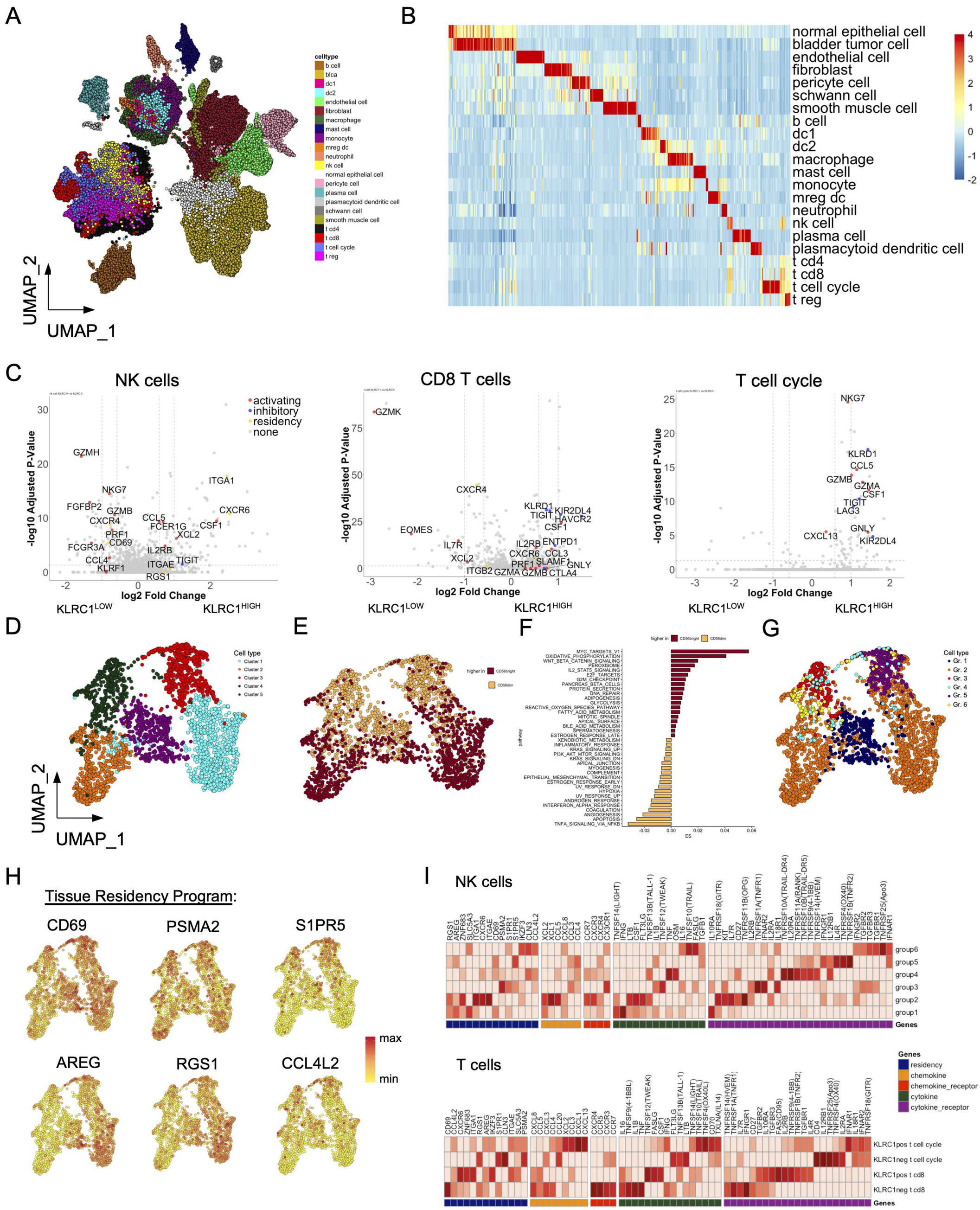
A
UMAP_2
UMAP_1
celltype
b cell
blca
dc1
dc2
endothelial cell
fibroblast
macrophage
mast cell
monocyte
mreg dc
neutrophil
nk cell
normal epithelial cell
pericyte cell
plasma cell
plasmacytoid dendritic cell
schwann cell
smooth muscle cell
t cd4
t cd8
t cell cycle
t reg
B
normal epithelial cell
bladder tumor cell
endothelial cell
fibroblast
pericyte cell
schwann cell
smooth muscle cell
b cell
dc1
dc2
macrophage
mast cell
monocyte
mreg dc
neutrophil
nk cell
plasma cell
plasmacytoid dendritic cell
t cd4
t cd8
t cell cycle
t reg
C
NK cells
activating
inhibitory
residency
none
-log10 Adjusted P-Value
log2 Fold Change
KLRC1LOW
KLRC1HIGH
CD8 T cells
T cell cycle
D
Cell type
Cluster 1
Cluster 2
Cluster 3
Cluster 4
Cluster 5
E
higher in
CD56bright
CD56dim
F
G
Cell type
Gr. 1
Gr. 2
Gr. 3
Gr. 4
Gr. 5
Gr. 6
H
Tissue Residency Program:
CD69
PSMA2
S1PR5
AREG
RGS1
CCL4L2
max
min
I
NK cells
T cells
Genes
residency
chemokine
chemokine_receptor
cytokine
cytokine_receptor
KLRC1pos t cell cycle
KLRC1neg t cell cycle
KLRC1pos t cd8
KLRC1neg t cd8

Figure 3.

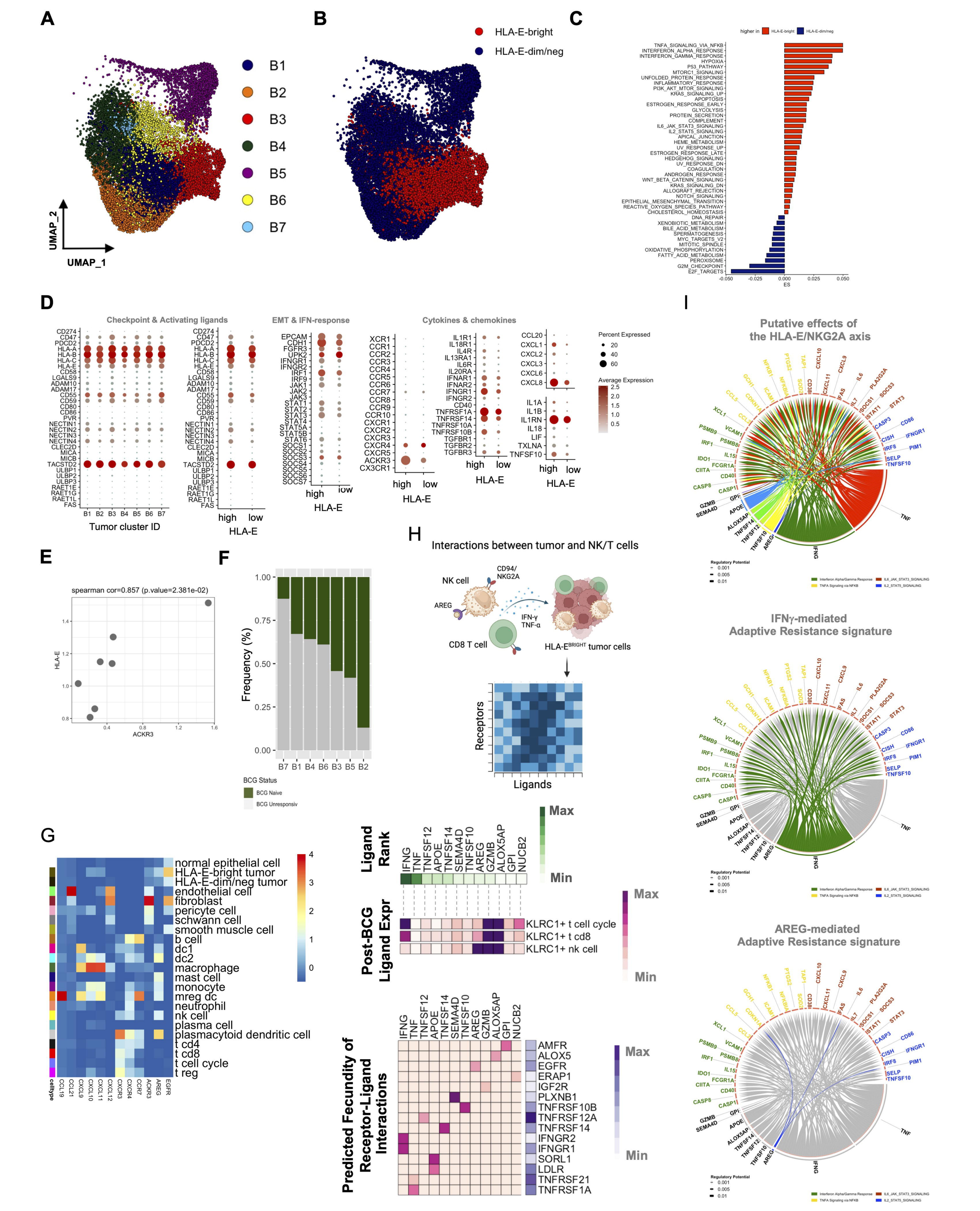
A
B1
B2
B3
B4
B5
B6
B7
UMAP_2
UMAP_1
B
HLA-E-bright
HLA-E-dim/neg
C
higher in
HLA-E-bright
HLA-E-dim/neg
TNFA_SIGNALING_VIA_NFKB
INTERFERON_ALPHA_RESPONSE
INTERFERON_GAMMA_RESPONSE
HYPOXIA
P53_PATHWAY
MTORC1_SIGNALING
UNFOLDED_PROTEIN_RESPONSE
INFLAMMATORY_RESPONSE
PI3K_AKT_MTOR_SIGNALING
KRAS_SIGNALING_UP
APOPTOSIS
ESTROGEN_RESPONSE_EARLY
GLYCOLYSIS
PROTEIN_SECRETION
COMPLEMENT
IL6_JAK_STAT3_SIGNALING
IL2_STAT5_SIGNALING
APICAL_JUNCTION
HEME_METABOLISM
UV_RESPONSE_UP
ESTROGEN_RESPONSE_LATE
HEDGEHOG_SIGNALING
UV_RESPONSE_DN
COAGULATION
ANDROGEN_RESPONSE
WNT_BETA_CATENIN_SIGNALING
KRAS_SIGNALING_DN
ALLOGRAFT_REJECTION
NOTCH_SIGNALING
EPITHELIAL_MESENCHYMAL_TRANSITION
REACTIVE_OXYGEN_SPECIES_PATHWAY
CHOLESTEROL_HOMEOSTASIS
DNA_REPAIR
XENOBIOTIC_METABOLISM
BILE_ACID_METABOLISM
SPERMATOGENESIS
MYC_TARGETS_V2
MITOTIC_SPINDLE
OXIDATIVE_PHOSPHORYLATION
FATTY_ACID_METABOLISM
PEROXISOME
G2M_CHECKPOINT
E2F_TARGETS
-0.050
-0.025
0.000
0.025
0.050
ES
D
Checkpoint & Activating ligands
EMT & IFN-response
Cytokines & chemokines
Tumor cluster ID
HLA-E
high
low
Percent Expressed
20
40
60
Average Expression
2.5
2.0
1.5
1.0
0.5
I
Putative effects of the HLA-E/NKG2A axis
Regulatory Potential
0.001
0.005
0.01
Interferon Alpha/Gamma Response
TNFA Signaling via NFKB
IL6_JAK_STAT3_SIGNALING
IL2_STAT5_SIGNALING
E
spearman cor=0.857 (p.value=2.381e-02)
HLA-E
ACKR3
F
Frequency (%)
BCG Status
BCG Naive
BCG Unresponsiv
H
Interactions between tumor and NK/T cells
NK cell
CD94/ NKG2A
AREG
IFN-γ
TNF-α
CD8 T cell
HLA-E^BRIGHT tumor cells
Receptors
Ligands
IFNγ-mediated Adaptive Resistance signature
AREG-mediated Adaptive Resistance signature
G
normal epithelial cell
HLA-E-bright tumor
HLA-E-dim/neg tumor
endothelial cell
fibroblast
pericyte cell
schwann cell
smooth muscle cell
b cell
dc1
dc2
macrophage
mast cell
monocyte
mreg dc
neutrophil
nk cell
plasma cell
plasmacytoid dendritic cell
t cd4
t cd8
t cell cycle
t reg
celltype
Ligand Rank
Max
Min
Post-BCG Ligand Expr
KLRC1+ t cell cycle
KLRC1+ t cd8
KLRC1+ nk cell
Predicted Fecundity of Receptor-Ligand Interactions
AMFR
ALOX5
EGFR
ERAP1
IGF2R
PLXNB1
TNFRSF10B
TNFRSF12A
TNFRSF14
IFNGR2
IFNGR1
SORL1
LDLR
TNFRSF21
TNFRSF1A

Figure 4.

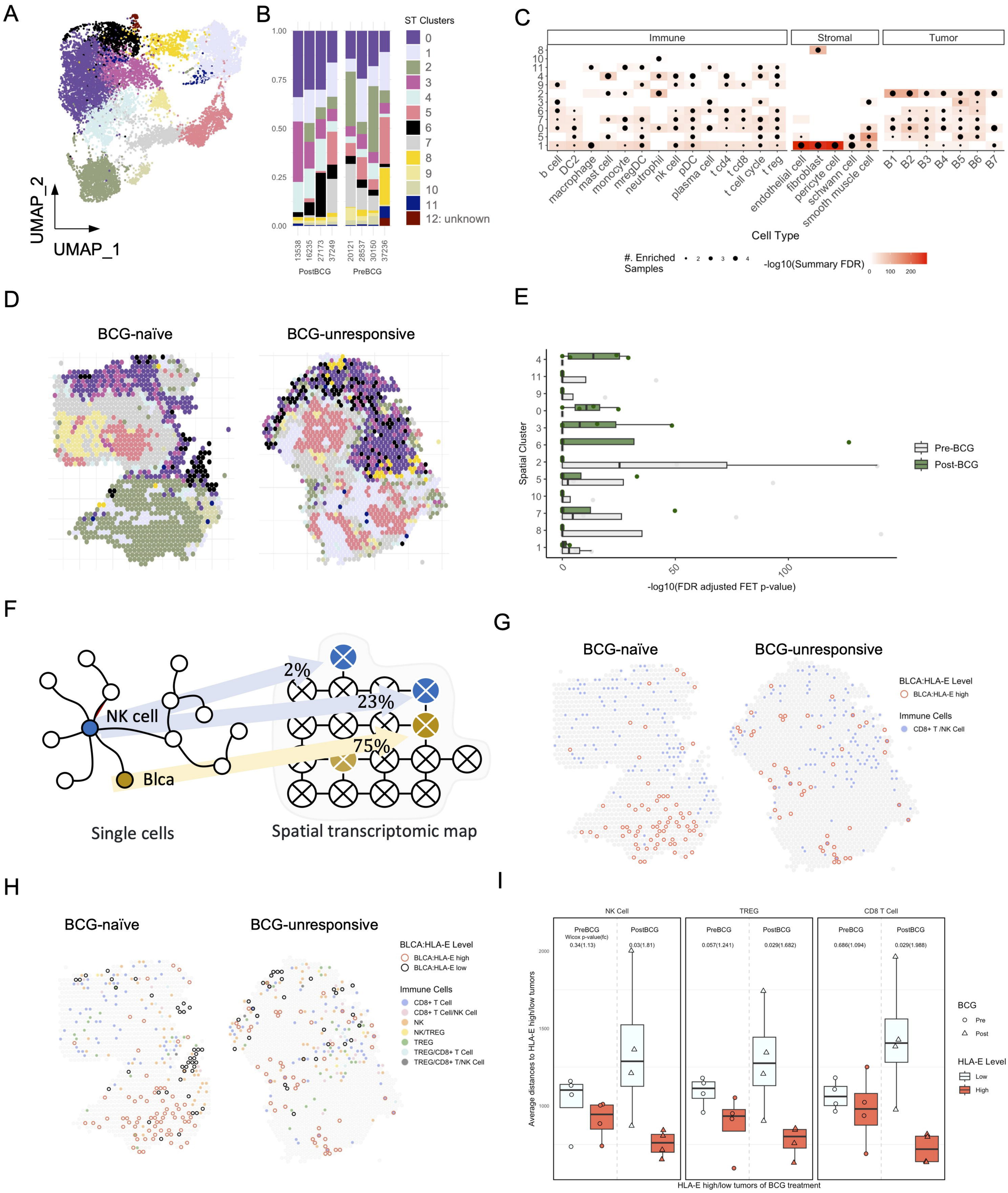
A
UMAP_2
UMAP_1
B
ST Clusters
0
1
2
3
4
5
6
7
8
9
10
11
12: unknown
PostBCG
PreBCG
C
Immune
Stromal
Tumor
Cell Type
#. Enriched Samples
-log10(Summary FDR)
D
BCG-naïve
BCG-unresponsive
E
Spatial Cluster
Pre-BCG
Post-BCG
-log10(FDR adjusted FET p-value)
F
NK cell
Blca
2%
23%
75%
Single cells
Spatial transcriptomic map
G
BCG-naïve
BCG-unresponsive
BLCA:HLA-E Level
BLCA:HLA-E high
Immune Cells
CD8+ T /NK Cell
H
BCG-naïve
BCG-unresponsive
BLCA:HLA-E Level
BLCA:HLA-E high
BLCA:HLA-E low
Immune Cells
CD8+ T Cell
CD8+ T Cell/NK Cell
NK
NK/TREG
TREG
TREG/CD8+ T Cell
TREG/CD8+ T/NK Cell
I
NK Cell
TREG
CD8 T Cell
PreBCG
PostBCG
Wicox p-value(fc)
0.34(1.13)
0.03(1.81)
0.057(1.241)
0.029(1.682)
0.686(1.094)
0.029(1.988)
Average distances to HLA-E high/low tumors
HLA-E high/low tumors of BCG treatment
BCG
Pre
Post
HLA-E Level
Low
High

Figure 5.

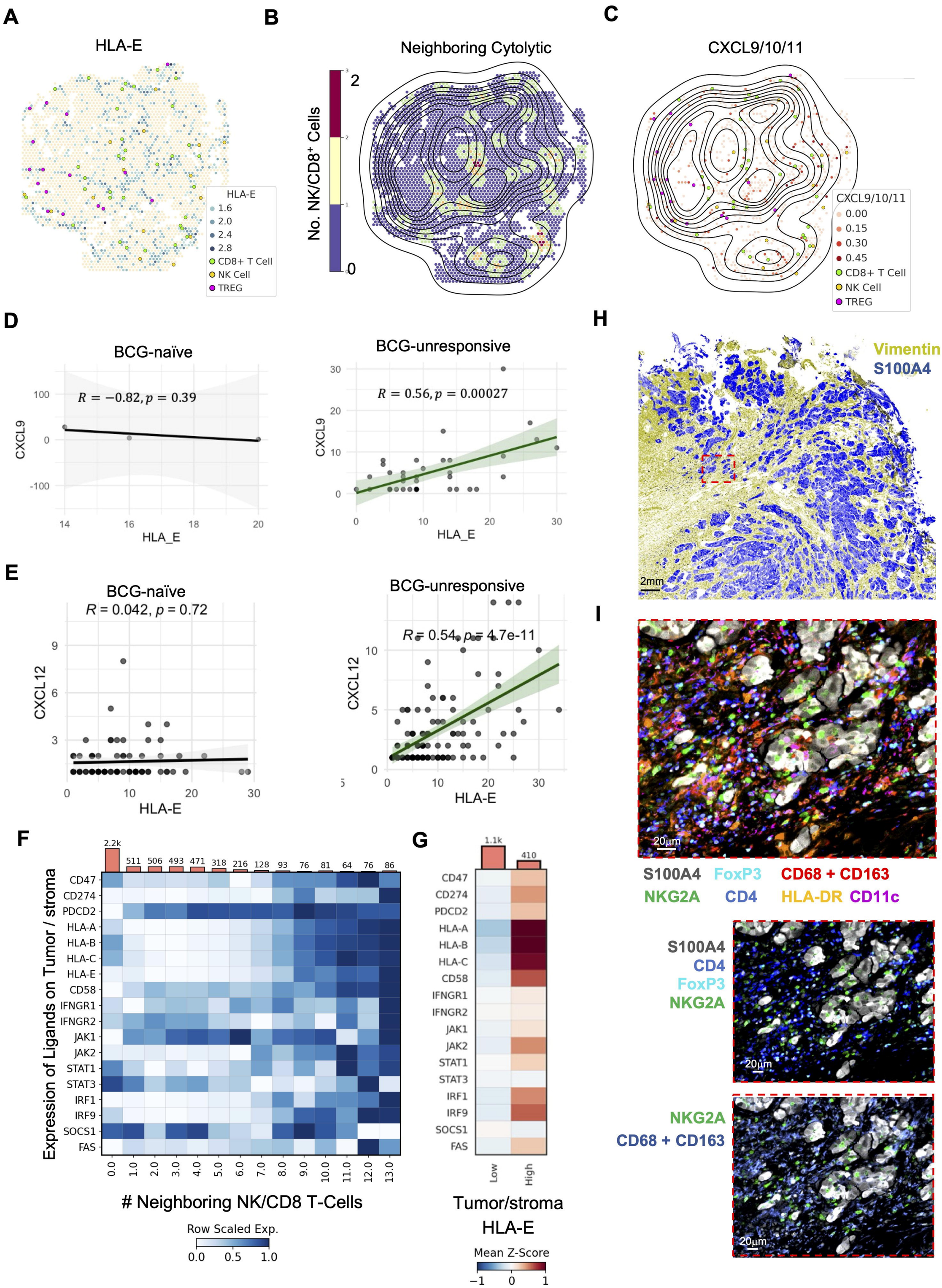
A
HLA-E
HLA-E
1.6
2.0
2.4
2.8
CD8+ T Cell
NK Cell
TREG
B
Neighboring Cytolytic
No. NK/CD8+ Cells
2
0
C
CXCL9/10/11
CXCL9/10/11
0.00
0.15
0.30
0.45
CD8+ T Cell
NK Cell
TREG
D
BCG-naïve
R = −0.82, p = 0.39
CXCL9
HLA_E
BCG-unresponsive
R = 0.56, p = 0.00027
CXCL9
HLA_E
E
BCG-naïve
R = 0.042, p = 0.72
CXCL12
HLA-E
BCG-unresponsive
R = 0.54, p = 4.7e-11
CXCL12
HLA-E
F
2.2k
511 506 493 471 318 216 128 93 76 81 64 76 86
Expression of Ligands on Tumor / stroma
CD47
CD274
PDCD2
HLA-A
HLA-B
HLA-C
HLA-E
CD58
IFNGR1
IFNGR2
JAK1
JAK2
STAT1
STAT3
IRF1
IRF9
SOCS1
FAS
0.0 1.0 2.0 3.0 4.0 5.0 6.0 7.0 8.0 9.0 10.0 11.0 12.0 13.0
# Neighboring NK/CD8 T-Cells
Row Scaled Exp.
0.0 0.5 1.0
G
1.1k
410
CD47
CD274
PDCD2
HLA-A
HLA-B
HLA-C
CD58
IFNGR1
IFNGR2
JAK1
JAK2
STAT1
STAT3
IRF1
IRF9
SOCS1
FAS
Low
High
Tumor/stroma
HLA-E
Mean Z-Score
−1 0 1
H
Vimentin
S100A4
2mm
I
20μm
S100A4 FoxP3 CD68 + CD163
NKG2A CD4 HLA-DR CD11c
S100A4
CD4
FoxP3
NKG2A
20μm
NKG2A
CD68 + CD163
20μm

Figure 6.

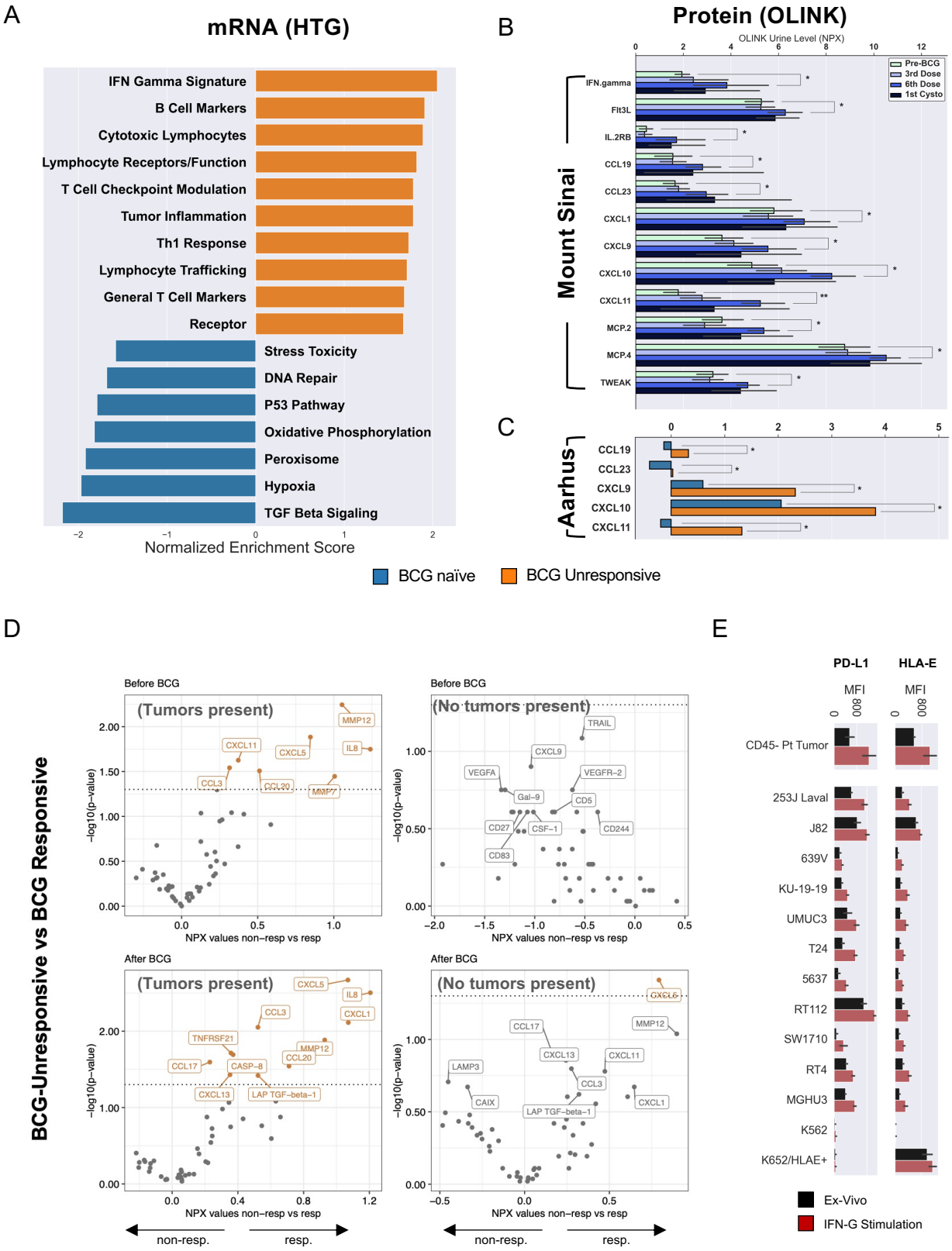
A
mRNA (HTG)
IFN Gamma Signature
B Cell Markers
Cytotoxic Lymphocytes
Lymphocyte Receptors/Function
T Cell Checkpoint Modulation
Tumor Inflammation
Th1 Response
Lymphocyte Trafficking
General T Cell Markers
Receptor
Stress Toxicity
DNA Repair
P53 Pathway
Oxidative Phosphorylation
Peroxisome
Hypoxia
TGF Beta Sigaling
Normalized Enrichment Score
B
Protein (OLINK)
OLINK Urine Level (NPX)
Pre-BCG
3rd Dose
6th Dose
1st Cysto
Mount Sinai
IFN.gamma
Flt3L
IL.2RB
CCL19
CCL23
CXCL1
CXCL9
CXCL10
CXCL11
MCP.2
MCP.4
TWEAK
C
Aarhus
CCL19
CCL23
CXCL9
CXCL10
CXCL11
BCG naïve
BCG Unresponsive
D
BCG-Unresponsive vs BCG Responsive
Before BCG
(Tumors present)
(No tumors present)
After BCG
NPX values non−resp vs resp
−log10(p−value)
non-resp.
resp.
E
PD-L1
HLA-E
MFI
CD45- Pt Tumor
253J Laval
J82
639V
KU-19-19
UMUC3
T24
5637
RT112
SW1710
RT4
MGHU3
K562
K652/HLAE+
Ex-Vivo
IFN-G Stimulation

Figure 1.

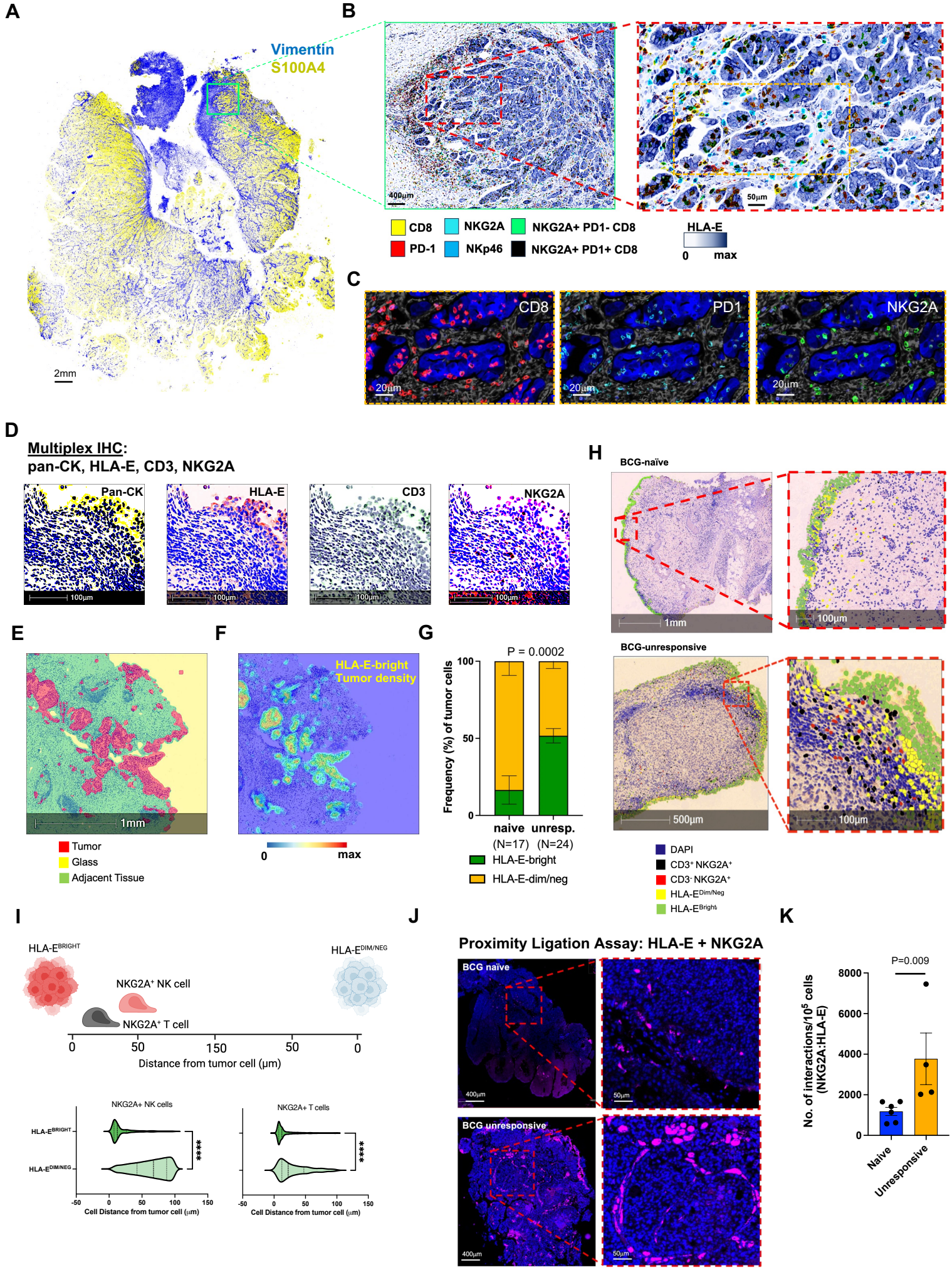
A
Vimentin
S100A4
2mm
B
400µm
50µm
CD8
NKG2A
NKG2A+ PD1- CD8
PD-1
NKp46
NKG2A+ PD1+ CD8
HLA-E
0
max
C
CD8
PD1
NKG2A
20µm
D
Multiplex IHC:
pan-CK, HLA-E, CD3, NKG2A
Pan-CK
HLA-E
CD3
NKG2A
100µm
E
1mm
Tumor
Glass
Adjacent Tissue
F
HLA-E-bright
Tumor density
0
max
G
P = 0.0002
Frequency (%) of tumor cells
100
50
0
naive
unresp.
(N=17)
(N=24)
HLA-E-bright
HLA-E-dim/neg
H
BCG-naïve
1mm
100µm
BCG-unresponsive
500µm
100µm
DAPI
CD3+ NKG2A+
CD3- NKG2A+
HLA-EDim/Neg
HLA-EBright
I
HLA-EBRIGHT
HLA-EDIM/NEG
NKG2A+ NK cell
NKG2A+ T cell
0
50
150
50
0
Distance from tumor cell (µm)
NKG2A+ NK cells
NKG2A+ T cells
HLA-EBRIGHT
HLA-EDIM/NEG
****
****
-50
0
50
100
150
Cell Distance from tumor cell (µm)
J
Proximity Ligation Assay: HLA-E + NKG2A
BCG naïve
BCG unresponsive
400µm
50µm
K
P=0.009
No. of interactions/10^5 cells
(NKG2A:HLA-E)
8000
6000
4000
2000
0
Naive
Unresponsive

Figure 2.

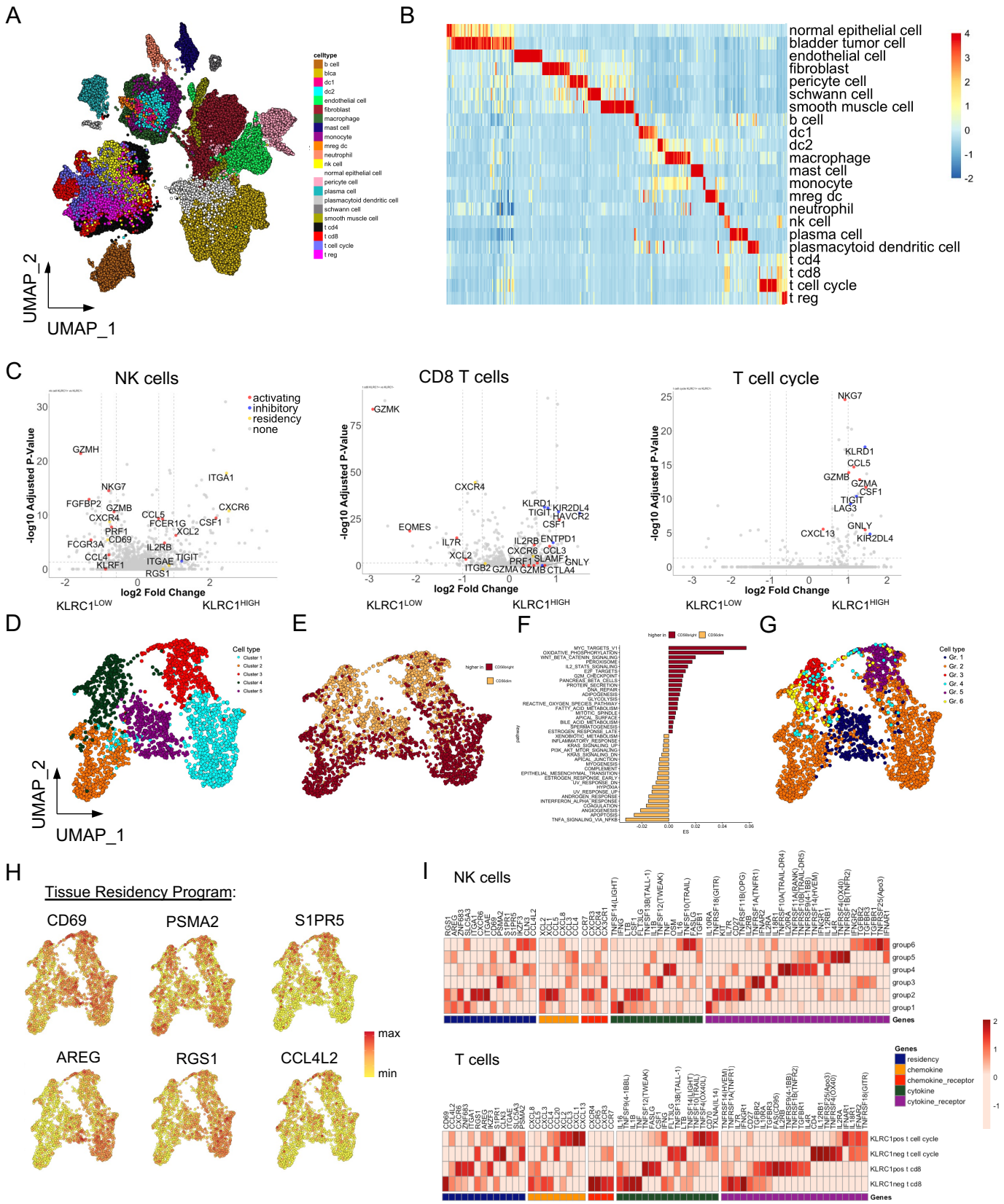
A
UMAP_2
UMAP_1
celltype
b cell
blca
dc1
dc2
endothelial cell
fibroblast
macrophage
mast cell
monocyte
mreg dc
neutrophil
nk cell
normal epithelial cell
pericyte cell
plasma cell
plasmacytoid dendritic cell
schwann cell
smooth muscle cell
t cd4
t cd8
t cell cycle
t reg
B
normal epithelial cell
bladder tumor cell
endothelial cell
fibroblast
pericyte cell
schwann cell
smooth muscle cell
b cell
dc1
dc2
macrophage
mast cell
monocyte
mreg dc
neutrophil
nk cell
plasma cell
plasmacytoid dendritic cell
t cd4
t cd8
t cell cycle
t reg
C
NK cells
CD8 T cells
T cell cycle
activating
inhibitory
residency
none
-log10 Adjusted P-Value
log2 Fold Change
KLRC1LOW
KLRC1HIGH
GZMH
NKG7
ITGA1
FGFBP2
GZMB
CXCR6
CXCR4
CCL5
FCER1G
CSF1
PRF1
XCL2
CD69
FCGR3A
IL2RB
CCL4
TIGIT
KLRF1
ITGAE
RGS1
GZMK
CXCR4
KLRD1
TIGIT
KIR2DL4
HAVCR2
CSF1
EQMES
IL7R
IL2RB
ENTPD1
CXCR6
CCL3
XCL2
PRF1
SLAMF1
GNLY
ITGB2
GZMA
GZMB
CTLA4
NKG7
KLRD1
CCL5
GZMB
GZMA
CSF1
TIGIT
LAG3
GNLY
CXCL13
KIR2DL4
D
Cell type
Cluster 1
Cluster 2
Cluster 3
Cluster 4
Cluster 5
UMAP_2
UMAP_1
E
higher in
CD56bright
CD56dim
F
higher in
CD56bright
CD56dim
pathway
ES
G
Cell type
Gr. 1
Gr. 2
Gr. 3
Gr. 4
Gr. 5
Gr. 6
H
Tissue Residency Program:
CD69
PSMA2
S1PR5
AREG
RGS1
CCL4L2
max
min
I
NK cells
group6
group5
group4
group3
group2
group1
Genes
T cells
KLRC1pos t cell cycle
KLRC1neg t cell cycle
KLRC1pos t cd8
KLRC1neg t cd8
Genes
Genes
residency
chemokine
chemokine_receptor
cytokine
cytokine_receptor

Figure 3.

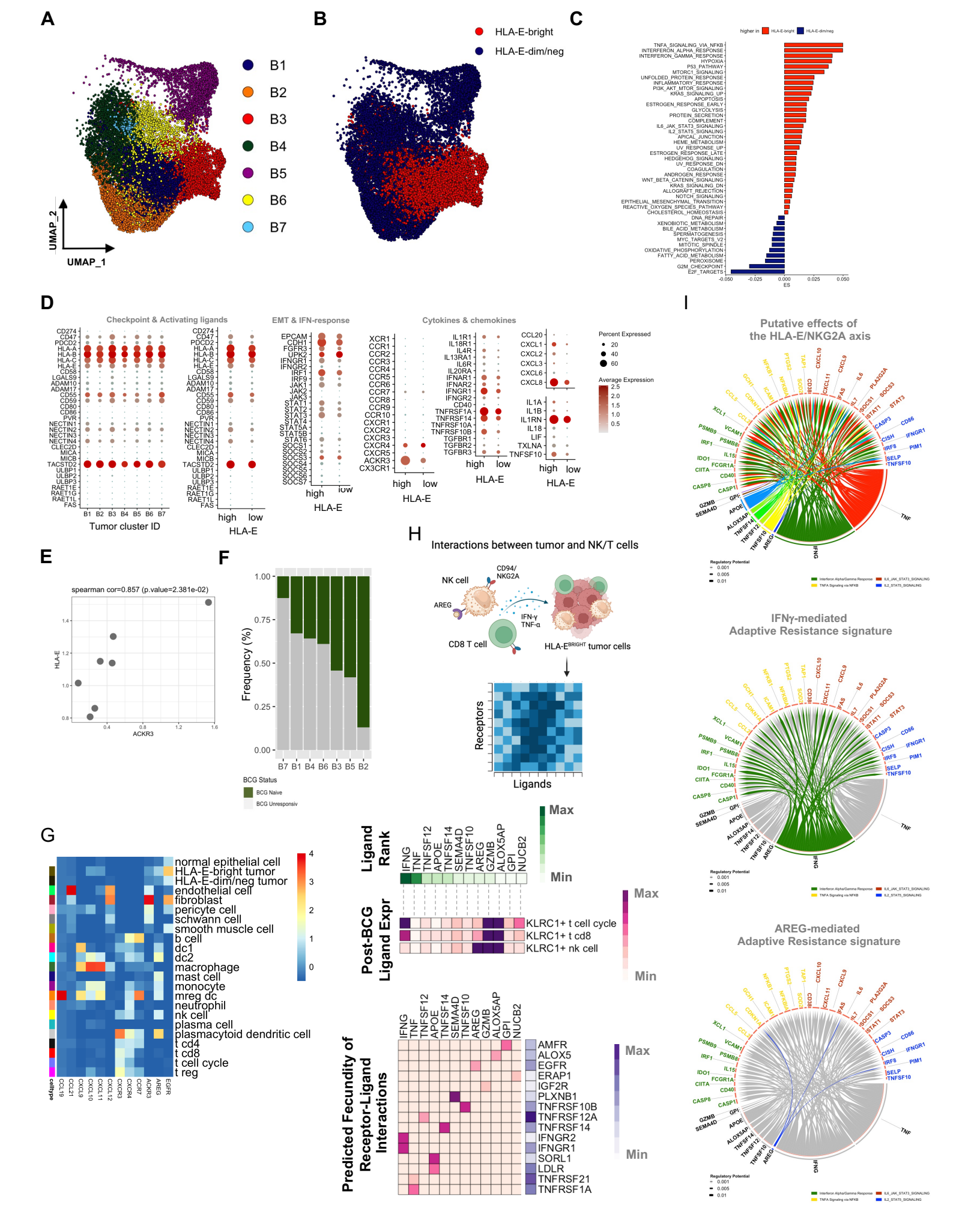
A
B1
B2
B3
B4
B5
B6
B7
UMAP_2
UMAP_1
B
HLA-E-bright
HLA-E-dim/neg
C
higher in
HLA-E-bright
HLA-E-dim/neg
ES
D
Checkpoint & Activating ligands
EMT & IFN-response
Cytokines & chemokines
Tumor cluster ID
HLA-E
Percent Expressed
Average Expression
E
spearman cor=0.857 (p.value=2.381e-02)
HLA-E
ACKR3
F
Frequency (%)
BCG Status
BCG Naive
BCG Unresponsiv
G
normal epithelial cell
HLA-E-bright tumor
HLA-E-dim/neg tumor
endothelial cell
fibroblast
pericyte cell
schwann cell
smooth muscle cell
b cell
dc1
dc2
macrophage
mast cell
monocyte
mreg dc
neutrophil
nk cell
plasma cell
plasmacytoid dendritic cell
t cd4
t cd8
t cell cycle
t reg
celltype
H
Interactions between tumor and NK/T cells
NK cell
CD94/
NKG2A
AREG
IFN-γ
TNF-α
CD8 T cell
HLA-E^BRIGHT tumor cells
Receptors
Ligands
Ligand Rank
Max
Min
Post-BCG Ligand Expr
KLRC1+ t cell cycle
KLRC1+ t cd8
KLRC1+ nk cell
Predicted Fecundity of Receptor-Ligand Interactions
AMFR
ALOX5
EGFR
ERAP1
IGF2R
PLXNB1
TNFRSF10B
TNFRSF12A
TNFRSF14
IFNGR2
IFNGR1
SORL1
LDLR
TNFRSF21
TNFRSF1A
I
Putative effects of
the HLA-E/NKG2A axis
IFNγ-mediated
Adaptive Resistance signature
AREG-mediated
Adaptive Resistance signature
Regulatory Potential

Figure 4.

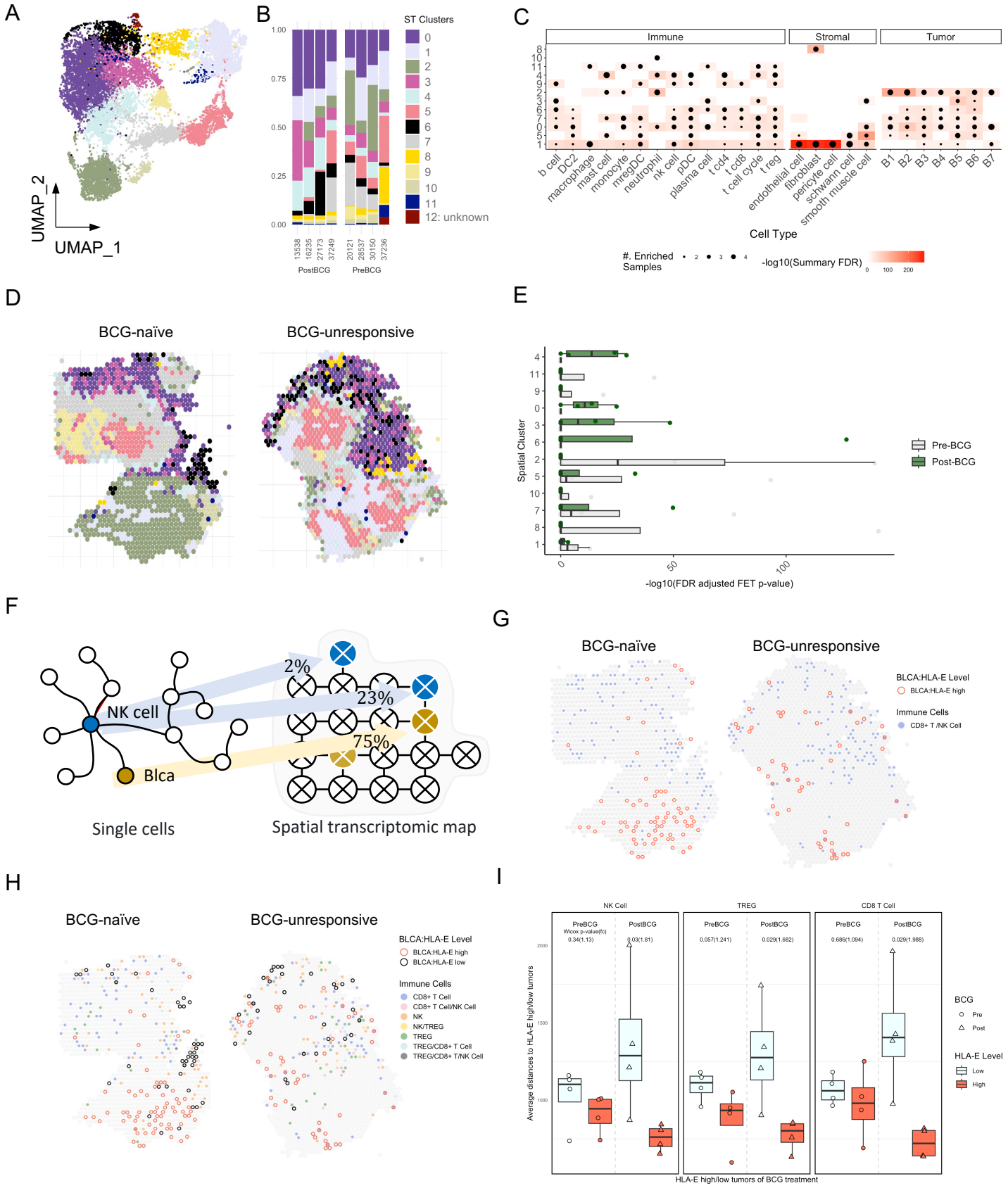
A
UMAP_2
UMAP_1
B
ST Clusters
0
1
2
3
4
5
6
7
8
9
10
11
12: unknown
PostBCG
PreBCG
C
Immune
Stromal
Tumor
b cell
DC2
macrophage
mast cell
monocyte
mregDC
neutrophil
nk cell
pDC
plasma cell
t cd4
t cd8
t cell cycle
t reg
endothelial cell
fibroblast
pericyte cell
schwann cell
smooth muscle cell
B1
B2
B3
B4
B5
B6
B7
Cell Type
#. Enriched Samples
-log10(Summary FDR)
D
BCG-naïve
BCG-unresponsive
E
Spatial Cluster
Pre-BCG
Post-BCG
-log10(FDR adjusted FET p-value)
F
NK cell
Blca
2%
23%
75%
Single cells
Spatial transcriptomic map
G
BCG-naïve
BCG-unresponsive
BLCA:HLA-E Level
BLCA:HLA-E high
Immune Cells
CD8+ T /NK Cell
H
BCG-naïve
BCG-unresponsive
BLCA:HLA-E Level
BLCA:HLA-E high
BLCA:HLA-E low
Immune Cells
CD8+ T Cell
CD8+ T Cell/NK Cell
NK
NK/TREG
TREG
TREG/CD8+ T Cell
TREG/CD8+ T/NK Cell
I
NK Cell
TREG
CD8 T Cell
PreBCG
PostBCG
Wicox p-value(fc)
0.34(1.13)
0.03(1.81)
0.057(1.241)
0.029(1.682)
0.686(1.094)
0.029(1.988)
Average distances to HLA-E high/low tumors
HLA-E high/low tumors of BCG treatment
BCG
Pre
Post
HLA-E Level
Low
High

Figure 5.

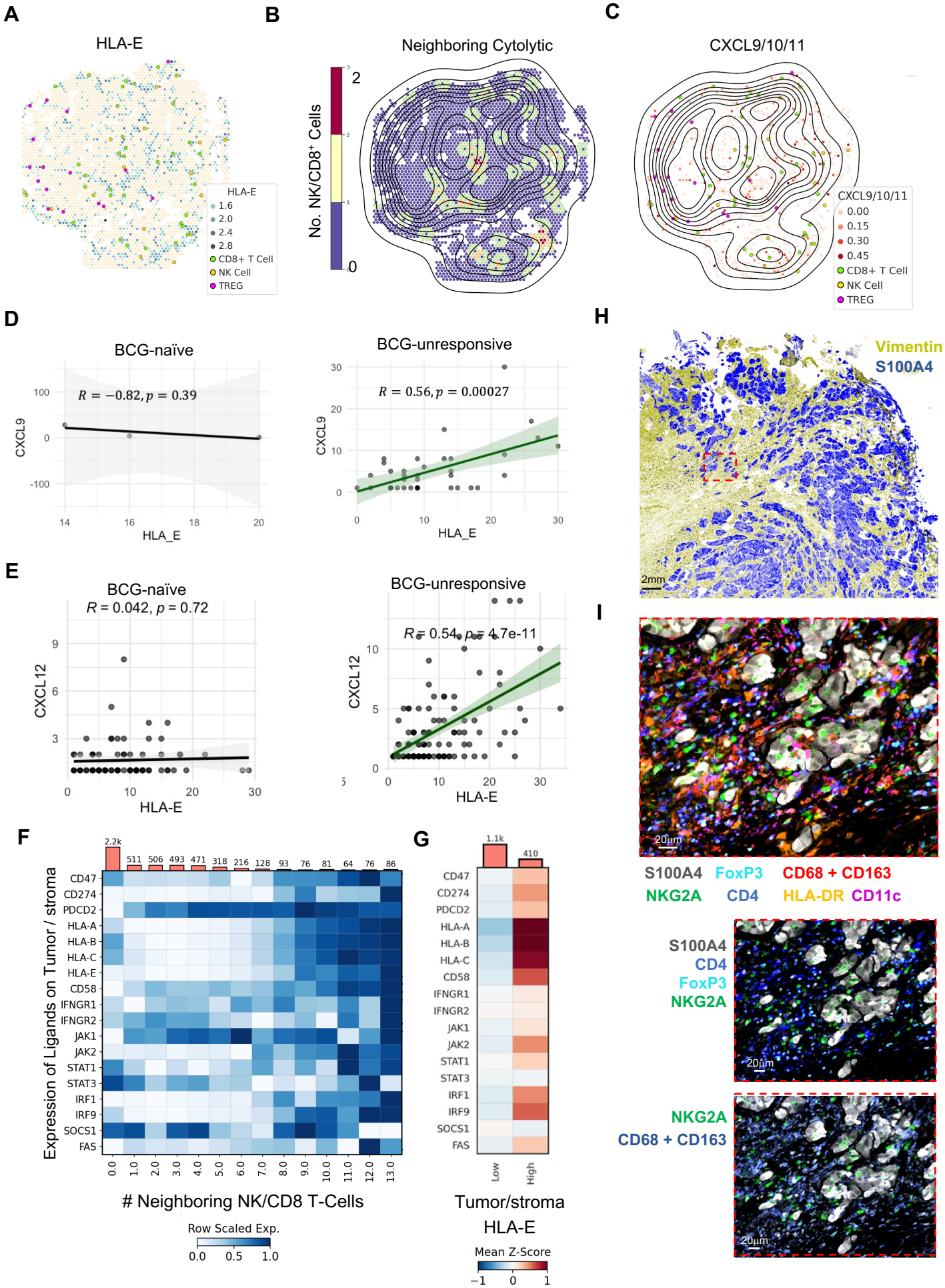
A
HLA-E
HLA-E
1.6
2.0
2.4
2.8
CD8+ T Cell
NK Cell
TREG
B
Neighboring Cytolytic
No. NK/CD8+ Cells
2
0
C
CXCL9/10/11
CXCL9/10/11
0.00
0.15
0.30
0.45
CD8+ T Cell
NK Cell
TREG
D
BCG-naïve
R = −0.82, p = 0.39
CXCL9
HLA_E
BCG-unresponsive
R = 0.56, p = 0.00027
CXCL9
HLA_E
E
BCG-naïve
R = 0.042, p = 0.72
CXCL12
HLA-E
BCG-unresponsive
R = 0.54, p = 4.7e-11
CXCL12
HLA-E
F
2.2k
511 506 493 471 318 216 128 93 76 81 64 76 86
Expression of Ligands on Tumor / stroma
CD47
CD274
PDCD2
HLA-A
HLA-B
HLA-C
HLA-E
CD58
IFNGR1
IFNGR2
JAK1
JAK2
STAT1
STAT3
IRF1
IRF9
SOCS1
FAS
0.0 1.0 2.0 3.0 4.0 5.0 6.0 7.0 8.0 9.0 10.0 11.0 12.0 13.0
# Neighboring NK/CD8 T-Cells
Row Scaled Exp.
0.0 0.5 1.0
G
1.1k
410
Low
High
Tumor/stroma
HLA-E
Mean Z-Score
−1 0 1
H
Vimentin
S100A4
2mm
I
20μm
S100A4 FoxP3 CD68 + CD163
NKG2A CD4 HLA-DR CD11c
S100A4
CD4
FoxP3
NKG2A
20μm
NKG2A
CD68 + CD163
20μm

Figure 6.

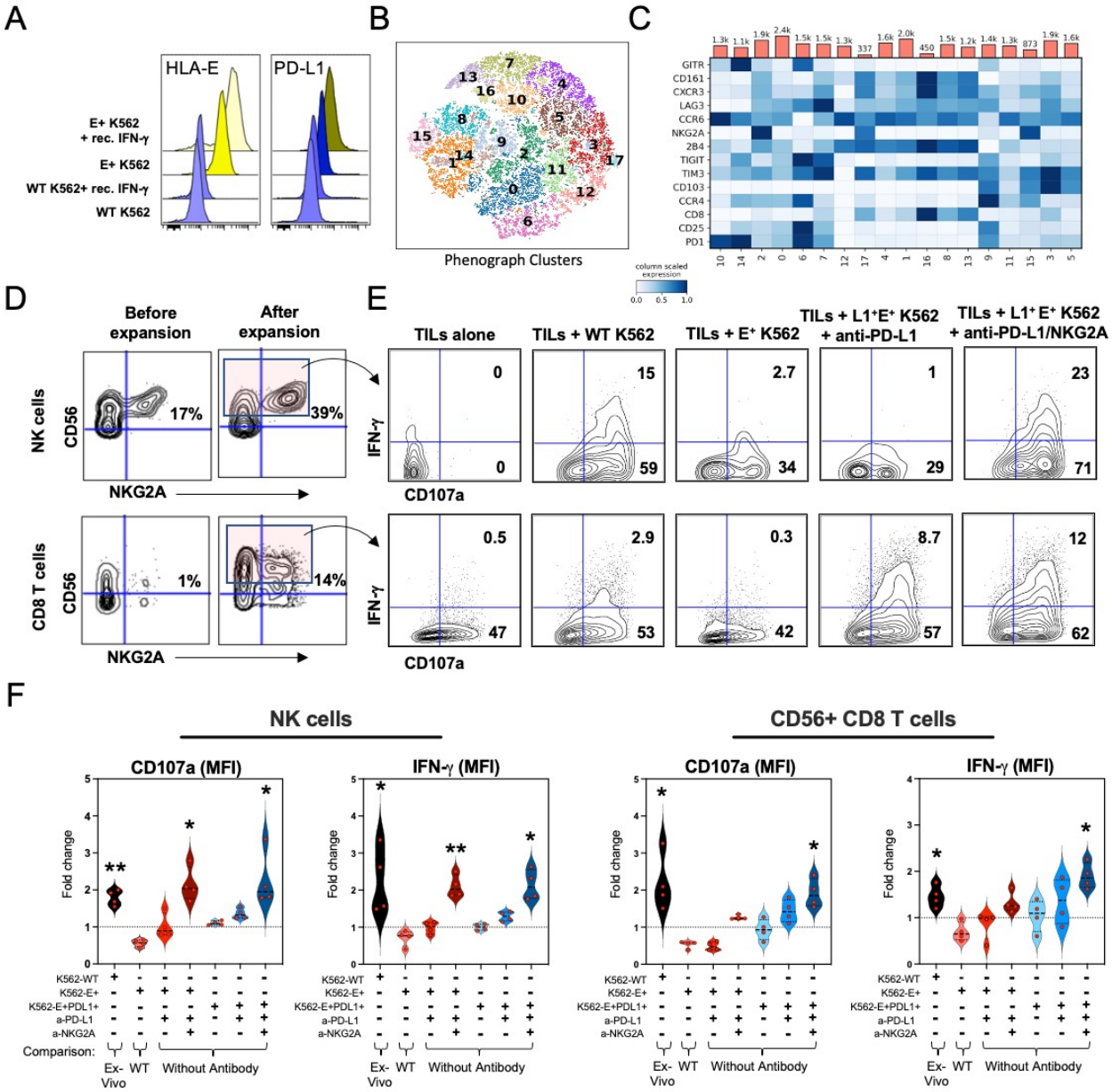
A
HLA-E
PD-L1
E+ K562 + rec. IFN-γ
E+ K562
WT K562+ rec. IFN-γ
WT K562
B
Phenograph Clusters
C
GITR
CD161
CXCR3
LAG3
CCR6
NKG2A
2B4
TIGIT
TIM3
CD103
CCR4
CD8
CD25
PD1
column scaled expression
D
Before expansion
After expansion
NK cells
CD56
NKG2A
17%
39%
CD8 T cells
1%
14%
E
TILs alone
TILs + WT K562
TILs + E+ K562
TILs + L1+E+ K562 + anti-PD-L1
TILs + L1+ E+ K562 + anti-PD-L1/NKG2A
IFN-γ
CD107a
0
0
15
59
2.7
34
1
29
23
71
0.5
47
2.9
53
0.3
42
8.7
57
12
62
F
NK cells
CD56+ CD8 T cells
CD107a (MFI)
IFN-γ (MFI)
Fold change
K562-WT
K562-E+
K562-E+PDL1+
a-PD-L1
a-NKG2A
Comparison:
Ex-Vivo
WT
Without Antibody

Figure 7.

| | Clinical Cohort Characteristics | | | | |
|---|---|---|---|---|---|
| | HTG | OLINK Urine (Sinai) | Single Cell | Spatial | Cytof |
| n samples, patients | 36, 27 | 42, 26 | 7, 6 | 20, 9 | 16, 16 |
| Female | 4 | 2 | 0 | 0 | 1 |
| BCG Naïve | 19 | 26 | 2 | 4 | 0 |
| BCG Unresponsive | 17 | - | 4 | 5 | 16 |
| Median Age | 64 | 69.5 | 66.9 | 70.6 | 68.5 |
| Median Months to Recurrence | 2.9 | 2.1 | 2.3 | 1.7 | 2.73 |
| Median Months to Progression | 6.7 | - | 14.3 | 23.28 | 4.43 |
| Stage at Collection | | | | | |
| CIS | 4 | - | - | - | - |
| Tis/Ta | 5 | 13 | - | 2 | 8 |
| T1 | 10 | 14 | 4 | 6 | 5 |
| T2 | - | - | - | - | 2 |
| T3 | - | - | 2 | - | 0 |
| T4 | - | - | - | - | 1 |

Table 1.

| Gene Set Names | Defining Genes |
|---|---|
| Interferon Gamma Response Signature | *CCL5, CD3D, CXCL10, IL2RB, LAG3, IDO1, IL2RG, STAT1, PRF1, PDCD1, GZMA, GZMB, CD8A, CXCL9, TBX21, CD27, CD4, CD74, IFNG, CCR5, CXCL11, CXCL13, CXCR6, PTPRC* |
| B Cell Markers | *CD79A, BLNK, CD79B, CCR9, CD19, PNOC, BLK, CD22, HLA-DOB, TCL1A, CR2, SPIB, CD72, TNFRSF17, HLA-DQA1, PAX5, MS4A1, MEF2C, FCRL2* |
| Cytotoxic CD8 T-Cells | *GZMK, FLT3LG, KLRK1, KLRD1, PRF1, GZMA, CD3G, CD8B, SIGIRR, GZMB, KLRB1, CD8A, GZMH, PF4, TBX21, CD3E, NKG7, CD27, IFNG, GNLY, EOMES, GZMM, KLRF1, KLRC1, RUNX3* |
| Cytotoxic Receptors and Function | *ZNF683, SLAMF6, KLRK1, KLRD1, SLAMF7, NCR1, SH2D1B, GZMA, TYROBP, SH2D1A, GZMB, KLRB1, KIR3DL3, CLEC4C, CLEC4D, KLRC1, GZMH, NKG7, NCR3, GNLY, GZMM, KLRF1* |
| T-Cell Checkpoint Modulation | *HLA-DQA2, CD274, TNFRSF14, CD86, CARD11, CD40, AKT1, CD3D, TNFRSF9, KLRK1, LAG3, CSK, TNFRSF13C, CD276, CD80, PDCD1, CD40LG, CD3G, PDCD1LG2, PTPN6, HLA-DQB2, ADORA2A, HLA-DPB1, TNFSF4, TIGIT, HLA-DRB1, CCL19, HAVCR2, CD3E, CD27, CD5, CCL21, CD4, HLA-DQA1, VAV1, CD70, CD24, GRB2, SRC, HLA-DRA, CD28, TNFSF13B, HLA-DPA1, TNFRSF4, CTLA4, ICOS, LYN, BTLA* |
| Tumor Inflammation | *PRF1, GZMA, GZMK, CCL5, CXCL10, IFNG, CXCL9, STAT1* |
| Th1 Polarization and Response | *NFKB1, RELA, IL12B, TBX21, IL2, IFNGR1, IL12RB1, RBPJ, JAK2, TYK2, JAK1, DLL1, IFNG, STAT1, STAT4, IL12A* |
| Lymphocyte Trafficking | *CD274, FAM129C, CDH2, CXCR4, CD68, PDCD1, PDCD1LG2, PLCG2, CD40LG, HLA-DOB, MAPK11, ITGAL, CD52, HLA-DPB1, HLA-DRB1, PVR, CD4, ITGA5, HLA-DQA1, VAV1, NCAM1, HLA-C, LILRB3, CTLA4, CD83, CD86, LILRB1, HLA-DOA, LILRA3, CXCL12, ROCK2, LILRA5, ITGAX, CD8A, PLCG1, TIGIT, HLA-DMB, ITGA4, MMP9, CD28, CYBB, SELE, ICOS, CLEC4E, ICAM1, HLA-DQA2, SDC1, CEACAM3, CD96, CD80, CD22, CD84, SELL, CD209, PDPN, SIGLEC5, HLA-DRA, SIGLEC1, ITGB2, S1PR4, CD7, CD177, ITGAM, HLA-A, ITK, CD40, ITGB7, CD34, MSN, HLA-F, CD276, PTK2B, RASSF5, CD6, S1PR1, MAPK14, VCAM1, HLA-E, TREM1, HLA-DMA, HLA-DPA1* |
| General T Cell Markers | *LCK, CD247, CD2, CD3E, CD3G, CD5, SH2D1A, TNFRSF25, TRAT1, CD96, CD6, LAMP1, CD3D, IL2RB, CD14, ZAP70* |
| Receptor | *PDCD1, HAVCR2, TNFRSF14, CD27, CD40, TLR4, KIR2DL1, ICOS, BTLA, TNFRSF9, ADORA2A, LAG3, TNFRSF4, CTLA4, TIGIT, IL2RA, TNFRSF18* |
| Stress Toxicity | *RAD17, DDIT3, TLR4, ATR, ADM, BID, CHEK2, HSP90B1, IL1B, RIPK1, CCL2, IL6, HSPA5, CD40LG, CRP, GADD45A, VEGFA, DDB2, HSP90AA1, CASP1, TNFRSF10A, PARP1, PVR, CDKN1A, TP53, TNFRSF10B, NBN, EDN1, FAS, SERPINE1, RAD51, NFAT5, ATG7, CA9, IFNG, ATG5, ATG12, XPC, CALR, GRB2, RAD9A, HMOX1, MMP9, HUS1, EPO, IL1A, CHEK1, ATM, TNF* |
| DNA Repair (Hallmark) | *TYMS, POLR1D, GTF2H1, ITPA, TAF6, TK2, SDCBP, GPX4, SMAD5, SAC3D1, UMPS, NUDT9, NME3, RPA3, NFX1, DGUOK, GTF2H3, DGCR8, DCTN4, ERCC2, TAF9, POLR2H, NME4, XPC, BOLA2_2B, DAD1, VPS37D, TMED2, NCBP2, RAE1, NUDT21, CCNO, GTF3C5, ERCC4, SUPT5H, ARL6IP1, EIF1B, ZNF707, AK3, VPS28, RAD52, TAF10, ERCC3, FEN1, SUPT4H1, PCNA, POLR2A, POLH, BCAP31, POLB, NT5C, HCLS1, SRSF6, POLR2J, REV3L, USP11, VPS37B, POLR2K, GTF2H5, ADCY6, HPRT1, TP53, PRIM1, RALA, BCAM, POLD1, CLP1, SURF1, POLD4, GMPR2, MPG, PNP, DDB1, POLR2D, RBX1, SF3A3, RFC4, ZWINT, IMPDH2, POLR2C, ADRM1, PDE6G, POLR2G, POLR1C, POLR2F, LIG1, DUT, CMPK2, SEC61A1, RFC3, GUK1, PDE4B, RAD51, GTF2F1, POLA2, STX3, TARBP2, CDA, APRT, ELL, RFC5, POM121, RPA2, POLR3C, NME1, POLR2E, AK1, NPR2, ERCC1, GSDME, TAF12, POLR2I, POLA1, CETN2, POLL, ZNRD1, POLD3, RNMT, TSG101, ELOA, DDB2, UPF3B, SNAPC5, CANT1, ADA, POLR3GL, TAF13, COX17, ERCC8, AAAS, BRF2, POLE4, SSRP1, TAF1C, RFC2, SNAPC4, EDF1, ERCC5, CSTF3, GTF2B, GTF2A2, NELFCD, MRPL40, RRM2B* |
| P53 Pathway (Hallmark) | *LRMP, IRAK1, DDIT3, AK1, BAK1, ACVR1B, RGS16, ITGB4, IFI30, HBEGF, SDC1, APAF1, MXD1, SOCS1, TXNIP, VWA5A, TRAFD1, BTG2, RAD51C, CEBPA, SPHK1, DGKA, HRAS, BAX, DDB2, GADD45A, CD82, TGFB1, RRAD, ELP1, FBXW7, CYFIP2, TCHH, PTPRE, ADA, PCNA, CDH13, CD81, CASP1, POLH, AEN, SLC3A2, SEC61A1, CDKN1A, LIF, TP53, PHLDA3, FAS, NINJ1, DEF6, FOS, TSPYL2, XPC, PROCR, HDAC3, RAD9A, HMOX1, ERCC5, CCND2, POM121, FOXO3, IL1A, CCND3, TNFSF9, TRAF4, TAP1, APP, HIST1H1C, PPP1R15A, NOTCH1, BTG1* |
| Oxidative Phosphorylation | *VDAC1, ALAS1, HSD17B10, SDHA, ALDH6A1, ATP5F1, PHB2, BAX, TCIRG1, GPX4, CASP7, NDUFA5, POLR2F, COX17, HTRA2, SURF1, OAT, SLC25A3, DLAT, GPI* |
| (Hallmark) Peroxisome (Hallmark) | *HSD11B2, ABCD2, ABCB1, ERCC1, ERCC3, HRAS, CDK7, CADM1, FDPS, BCL10, ACSL1, MSH2* |
| Hypoxia | *NFKB1, VDAC1, ADORA2B, ATR, NAMPT, ADM, TXNIP, MAP3K1, F3, VEGFA, EGR1, RBPJ, MIF, IGFBP3, NCOA1, HIF1A, PLAU, TP53, EDN1, SERPINE1, FOS, CA9, PER1, NOS3, MMP9, HMOX1, LGALS3, MET, EPO, APEX1, BLM, GPI, PIM1* |
| TGF Beta Signaling | *CBL, CREBBP, LTBP1, ID1, TGFB1, SMAD5, MYC, PARP1, TGFBR3, EP300, IFNG, TGFBR1, SMAD2, TGFBR2, THBS1, SMAD3, TGFB3, MAPK3, TNF* |

**Extended data Table S1:** Genes defining gene-set enrichment pathways

| Channel | Marker | Clone |
|---|---|---|
| 1 | DAPI | NA |
| 2 | CD45RO | T200/797 |
| 3 | HLA-A | EP1395Y |
| 4 | CD4 | EPR6855 |
| 5 | Podoplanin | 18H5 |
| 6 | CD20 | SP32 |
| 7 | CD68 | RM1031 |
| 8 | CD8 | EPR26538-16 |
| 9 | SMA | EPR5368 |
| 10 | CD11c | FK24 |
| 11 | HLA-E | MEM-E/02 |
| 12 | CD31 | WM59 |
| 13 | HLA-DR | EPR6148 |
| 14 | Granzyme B | EPR20129-217 |
| 15 | Vimentin | LN-6 |
| 16 | CD3e | EPR5361(2) |
| 17 | CD56 | EP2567Y |
| 18 | CD34 | 4H11 |
| 19 | PD-L1 | 28-8 |
| 20 | ICOS | HK53 |
| 21 | CD57 | HNK1 |
| 22 | FOXP3 | 2A11G9 |
| 23 | NKG2D | polyclonal |
| 24 | Pan-Cytokeratin | AE1+AE3 |
| 25 | CD163 | RM1114 |
| 26 | PAX-5 | EPR3730(2) |
| 27 | ASCT2 | CAL33 |
| 28 | PD-1 | CAL20 |
| 29 | CD21 | EP3093 |
| 30 | GLUT1 | EPR3915 |
| 31 | CD11b | M1/70 |
| 32 | Ki67 | EPR3610 |
| 33 | S100A4 | 1F12-1G7 |
| 34 | Collagen IV | HL1351 |
| 35 | CD14 | 1H5D8 |
| 36 | LC3B | EPR21234 |
| 37 | CD45 | EPR27167-58 |
| 38 | IFNG | IFNG/466 |
| 39 | CD79a | EP3618 |
| 40 | IDO1 | EPR20374 |
| 41 | CD44 | IM7.8.1 |
| 42 | NKG2A | ab96319 |
| 43 | GATA3 | EPR16651 |
| 44 | CD66b | polyclonal |
| 45 | CD138 | polyclonal |
| 46 | HIF1A | EPR16897 |
| 47 | MPO | EPR20257 |
| 48 | DNAM-1 | EPR23641-137 |
| 49 | NKp46 | Innate Pharma |
| 50 | CXCR3 | ab71864 |
| 51 | CD38 | EPR22691-219 |
| 52 | CD16 | EPR22409-124 |
| 53 | ATPA5 | polyclonal |
| 54 | CTST | polyclonal |
| 55 | LDHA | EP1563Y |
| 56 | HK1 | EPR10134(B) |
| 57 | MMP9 | EP1254 |
| 58 | PHHH3 | polyclonal |
| 59 | BAX | ab53154 |

**Extended data Table S2:** Antibody panel for CODEX multiplexed immunofluorescence staining

| cell cluster | signature genes |
|---|---|
| normal epithelial cell | C19orf33, SNCG, MIR205HG, KRT19, KRT17, FXYD3, SYT8, SMIM22, ELF3, KRT18, CLDN4 |
| blca | KRT8, CD24, KRT18, TACSTD2, MGST1, FXYD3, ELF3, CLDN4, SMIM22, KLF5, KRT7, KRT19, DHRS2, S100P, GDF15, PSCA, AGR2, SERINC2, S100A14, SDC1, GATA3, KRT20, CLDN7, FOXQ1, CYB5A, AKR1C3, C19orf33, TMEM54, MDK, RARRES1, RAB25, NQO1, TMEM97, SDC4, VSIG2, RALBP1, EFNA1, CDH1, EHF, JUP, CAPS, IDH1, SPTSSB, HEBP2, SPINT2, CAMK2N1, AL158206.1, MGST2, TSTD1, MAL2, S100A13, ADIRF, HES1, PTPRF, ERBB2, TBX3, PHLDA2, RAB11FIP1, SFN, ID1, ATP1B1, GNL3, CYP4B1, TXNDC17, MARCKSL1, LSR, NR2F6, ABHD11, PLPP2, TNFRSF21, S100A16, SLPI, TSPAN13, TNFAIP2, SPINT1, NEDD4L, STAP2, KRTCAP3, CD9, BEX3, AKR1C2, EPCAM, RAB11A, PPARG, FOXA1, CTTN, GIPC1, ALAS1, AHR, SH3YL1, EMP2, TCEAL4, GGCT, PAFAH1B3, FBP1, NDUFS6, IGFBP3, SNHG18, GPRC5A, AP1S1, CISD3, ECHS1, TIMM13, RBM47, UQCC2, POLR2I, TSPAN6, OCIAD2, GRHL3, ARPC1A, KRT10, CENPX, CRABP2, MRPL14, DCXR, PRDX2 |
| endothelial cell | PCAT19, SPARCL1, RAMP2, VWF, EGFL7, ECSCR, PLVAP, AQP1, TM4SF1, CLDN5, ADGRL4, CLEC14A, CAV1, CRIP2, IGFBP7, EPAS1, RAMP3, EMP1, IFI27, KLF2, SPRY1, EMCN, A2M, ENG, NPDC1, STC1, HYAL2, CAVIN1, TCF4, BCAM, IFITM2, STOM, MMRN2, ESAM, CALCRL, IFITM3, CNN3, CAVIN2, TGFBR2, IGFBP4, CD34, S1PR1, SOCS3, PECAM1, ACKR1, GJA1, CD59, SLC9A3R2, ITGA6, NNMT, PDLIM1, APP, MTUS1, TSPAN7, ADAMTS9, C2CD4B, CDH5, ADAMTS1, APOLD1, MEF2C, LMO2, YBX3, ELK3, TIMP3, CYYR1, CD93, TFPI, THBD, RNASE1, SPTBN1, HLA-DRB5, ITGA5, SOX18, GRASP, CLU, ID3 |
| fibroblast | DCN, CCDC80, IGFBP6, COL1A2, MGP, COL6A2, C1R, PLAC9, FBLN1, CFD, PCOLCE2, SERPING1, LUM, SERPINF1, C1S, MFAP5, MFAP4, SOD3, COL6A1, PI16, OGN, GSN, CLU, SPARCL1, LTBP4, COL6A3, MMP2, EFEMP1, C3, SFRP2, SCARA5, ADH1B, GPX3, SLIT2, CALD1, TIMP2, COL3A1, SPARC, CTSK, FBN1, SPON2, PMP22, PCOLCE, CCN1, PLPP3, OLFML3, EGR1, TFPI, FBLN5, ACKR3, CD34, FBLN2, DPT, RARRES2, APOD, IGFBP5, LRP1, CCN2, ABI3BP, FGFR1, ISLR, GPNMB, AEBP1, CCN5, TIMP1, MXRA8, SOCS3, MFGE8, NNMT, IGFBP7, CEBPD, EMP1, CD248, MYC, C11orf96, AC080038.1, NFIA, FSTL1, TIMP3 |
| pericyte cell | RGS5, PPP1R14A, BGN, TPM2, MYL9, IGFBP7, CALD1, MFGE8, COL4A1, NDUFA4L2, COL4A2, C11orf96, ACTA2, MGP, CAV1, PDGFRB, COX7A1, SOD3, COL18A1, CPE, SPARC, COL3A1, COL6A2, CAVIN3, CSRP2, CRIP2, LHFPL6, COX4I2, WFDC1, COL1A2, A2M, TPM1, PDGFA, TGFB1I1, COL6A1, SPARCL1, MEF2C, FAM162B, HIGD1B, HES4, SELENOM, IGFBP2, CNN3, FN1, FILIP1L, MAP1B, LBH, EHD2, CRYAB, TPPP3, EPS8, IFITM3, PCOLCE, GJA4, CCDC102B, PTP4A3, MYO1B, NR2F2, TINAGL1, PLAC9, RRAS, CYGB, NREP, MYH11, RAMP1, AP002956.1, PLXDC1, RBPMS, SERPING1, ITGA1, LAMA4, PTMS, ACTN1, DSTN |
| schwann cell | NRXN1, CRYAB, GPM6B, S100B, CDH19, SCN7A, MAL, ANGPTL7, LGI4, CHL1, MPZ, GFRA3, PLP1, CADM1, MATN2, SEMA3B, ZEB2-AS1, ANK3, PMP22, AC005747.1, TMEM176B, SPARC, VWA1, PDGFA, CD9, IGFBP7, CLU, SPARCL1, FGL2, RHOB, PRNP, EPB41L2, NDRG2, CNN3, SAMHD1, PDK4, ZEB2 |
| smooth muscle cell | CNN1, ACTG2, PCP4, DES, MYH11, PPP1R14A, TPM2, ACTA2, MYL9, SMTN, FHL1, CSRP1, MYLK, CKB, ECRG4, RAMP1, ACTC1, SORBS1, TPM1, TGFB1I1, SPARCL1, PALLD, TAGLN, PDLIM3, CRYAB, CAV1, SYNPO2, SYNM, SORBS2, TNS1, HSPB6, SLMAP, RBPMS, FERMT2, SELENOM, PSD, NEXN, COX7A1, LIMS2, PTGS1, PDLIM7, CARMN, ACTN1, FN1, AC022868.1, VWA1, CALD1, AF001548.1, MAP1B, COL6A1, LPP, LMOD1, SVIL, FLNA, PGM5, NIBAN1, PKIG, DSTN, FXYD6, CFL2, PITX1, CAVIN1, DMD, PGM5-AS1, FLNC, SLC25A4, ALDH1B1, FBXO32, RBPMS2, HSPB8, LMO3, TNNT2, RBFOX3, DIXDC1, KANK2, TGM2, RRAS, RARRES2, COL4A2, ILK, VCL, CLU, IGFBP7, NFIA, PPP1R12A, COL6A2, NME4, NUPR1, TCEAL4, PLEKHO1, AD000090.1 |
| b cell | IGHM, CD79A, CXCR4, IGKC, CCR7, CD37, VPREB3, ARHGAP24 |
| dc1 | LGALS2, CLEC9A, DNASE1L3, WDFY4, IDO1, XCR1, HLA-DOB, RAB7B, SERPINF2, S100B, NAPSB, BATF3, P2RY6, WFDC21P, C1orf54, SLAMF8, CPVL, CADM1, ASB2, IRF8, SHTN1, PADI2, LYZ, C1orf162, NAAA, HCK, SPI1, SLAMF7, LY86, VMO1, HLA-DQB1, PLEK, ANPEP, FGD2, HLA-DQA1, MPEG1, AIF1, MNDA, CLEC7A, HLA-DRB6, HLA-DPB1, PTPRE, HLA-DPA1, LGALS9, RGS10, HLA-DMB, HLA-DRA, FGL2, HLA-DRB1, HLA-DMA, CD86, CPNE3, SMCO4, SNX3, RAB32, CXCL16, BCL2A1, PPT1, BASP1, LST1, GCA, ITGAX, RNASE6, AP1S2, ADA2, TAP1, RGCC, TGFBI, ITGB2, PARVG, AC004687.1, SELPLG, LSP1, COTL1, SERPINB9, CD40, CD83, CTSZ, BID, SEMA4A, GNA15, ASAP1, C20orf27, SAMHD1, UNC119, CCDC88A, PLEKHO1, RGS19, PYCARD, PDLIM7, SERPINB1, ATG3, LIMD2, LCP1, EVI2B, SEPTIN6, TYMP, HLA-DRB5, LSM6, FNBP1, CCND1, PAK1, FAM49B, TNFAIP8, WAS, HCLS1, CD48, NFKBID, TMEM14A, PRCP, PSMB9, SNX10, PPA1, UCP2, DUSP4, DNAJC4, ICAM3, CST7, RNH1, ANXA6, PSME2, NET1, SERPINF1, AC010618.1, GLIPR1, NME4, RNASET2, SGK1, DBNL, MRPL23, VASP, TPP1, FMNL1, ACTN1, CKLF, CFL1, CYB5R3, RHOG, CORO1A, SYNGR2, GPR183, LTB, MZT2A, CAP1, CDK2AP2, GNG5, SERPINB6, GMFG, GPSM3, CRIP1, GABARAP, PLAUR, AP2S1, DUSP2, CTSS, HLA-F, FCGRT, NR4A2, LAPTM5, CD53, RGS2, GTF3C6, BUD23, CD37, MSN, CD52 |
| dc2 | LST1, AIF1, HLA-DQB1, TYROBP, FCER1A, HLA-DQA1, CD1C, FCER1G, HLA-DMB, MS4A6A, C1orf162, SPI1, CLEC10A, GPR183, CD86, NAPSB, JAML, HLA-DPB1, HLA-DMA, HLA-DRB6, LYZ, CD1E, PKIB, LY86, HLA-DRB1, HLA-DPA1, CPVL, RNASE6, MNDA, LGALS2, IGSF6, HCK, HLA-DRA, HLA-DQA2, HLA-DQB2, PLD4, FCGR2B, CALHM6, CXCL16, COTL1, NR4A3, OLR1, CLEC7A, ITGB2, AXL, RGS10, BCL2A1, LGALS9, PAK1, PLAUR, AP1S2, TYMP, CD83, LSP1, ALOX5AP, YWHAH, EVI2B, FAM49B, RGS1, PLSCR1, RGS2, PYCARD, CST7, GPSM3, MACROH2A1, RNASET2, HCLS1, BASP1, CD53, SAMSN1, CORO1A, LAPTM5, CXCR4, GMFG |
| macrophage | AIF1, C1QC, C1QA, C1QB, TYROBP, FCER1G, FCGR2A, MS4A7, MS4A6A, CD14, APOE, SPI1, APOC1, MSR1, FCGR3A, MS4A4A, TGFBI, CSF1R, LST1, CTSZ, HLA-DQA1, SPP1, CD163, CTSB, DAB2, HLA-DPB1, ADAP2, HLA-DMB, TREM2, ITGB2, LAPTM5, LGMN, CD4, CCL3, RNF130, HLA-DQB1, C1orf162, OLR1, |
| mast cell | TPSB2, TPSAB1, CPA3, IL1RL1, RHEX, LTC4S, GATA2, FCER1G, CTSG, HDC, VWA5A, KIT, MS4A2, CLU, ALOX5AP |
| monocyte | AIF1, TYROBP, FCER1G, LST1, LYZ, S100A8, S100A9, SERPINA1, BCL2A1, PLAUR, IL1B, C5AR1, CTSS, G0S2, FCN2, MNDA, SPI1, OLR1, SOD2, TYMP, COTL1, MS4A6A, CSTA, SAMSN1, MS4A7, EREG, CD14, C1orf162, CLEC7A, ITGB2, SRGN, LAPTM5 |
| mreg dc | LAMP3, CCL22, CCL19, NCCRP1, EBI3, CCL17, TVP23A, AOC1, IDO1, CD200, FSCN1, CFP, CCR7, WFDC21P, RASSF4, TMEM176A, CD86, POGLUT1, BIRC3, CD40, IL4I1, TMEM176B, BCL2A1, TBC1D4, RAMP1, NRP2, CD83, MIR155HG, GPR183, LSP1, HLA-DQA1, SAMSN1, IRF4, BASP1, TYROBP, HLA-DQB1, LAD1, IL7R, TXN, KDM2B, HLA-DPB1, MARCKSL1, HLA-DQA2, KYNU, HLA-DRA, NUB1, RFTN1, DUSP5, SYNGR2, ANXA6, RELB, MTHFD2, MGLL, RGS1, LGALS9, HLA-DPA1, TYMP, ERICH1, CSTA, ID2, GRSF1, SPI1, NABP1, CRIP1, KIF2A, HLA-DRB1, PPA1, VOPP1, CFLAR, SOCS1, NFKB1, HMGN3, TNFAIP8, COTL1, CTSH, STK4 |
| neutrophil | G0S2, CSF3R, TREM1, LUCAT1, S100A8, IL1R2, SLC11A1, NAMPT, CXCL8, BCL2A1, S100A9, IVNS1ABP, TPI1, ZFAS1 |
| nk cell | NKG7, GNLY, CCL5, CTSW, CST7, GZMB, TYROBP, PRF1, CD7, GZMA, HCST, KLRD1, CD247, TRDC, PTPRC, KLRC1, CCL4 |
| plasma cell | MZB1, DERL3, CD79A, FKBP11, JCHAIN, IGHG3, TNFRSF17, IGLC2, ITM2C, CD27, PIM2, IGHA1, SEC11C, ANKRD28, SLAMF7, PRDX4, IGHG1, JSRP1, XBP1, IGLC3, IGKC, POU2AF1, CD38, IGHG2, ST6GAL1, TPD52, SPCS3, SDF2L1, ANKRD36BP2, DNAJB9, SPAG4, EAF2, ERLEC1, IGHA2, CRELD2, RNU2-63P, TXNDC15, DTNB, TXNDC5, HERPUD1, KLF13, IGHGP, PRDM1, IGHG4, IGLV3-1, PDE4B, PLPP5, ISG20, GLRX, SSR3, RN7SL2, RN7SL1, NUCB2, MANF, CYTOR, ICAM3, CFLAR, SELENOS |
| plasmacytoid dendritic cell | PLAC8, PLD4, SCT, LILRA4, LRRC26, PTCRA, SPIB, TCL1A, SMPD3, IRF4, NAPSB, LILRB4, DERL3, GZMB, MZB1, IRF7, BCL11A, JCHAIN, MYBL2, IRF8, C12orf75, GPR183, CLIC3, LDLRAD4, SELL, EGLN3, ITM2C, NR4A3, ALOX5AP, THEMIS2, CXCR3, RNASE6, TSPAN13, OPN3, CCDC50, SLC15A4, PPP1R14B, SEC61B, AC004687.1, AREG, FCER1G, DUSP5, SLC7A5, TYROBP, CXCR4, HERPUD1, NR3C1, GNA15, CREM, SERPINF1, ZC3HAV1, N4BP2L1, RGS1, RGS2, TCF4, MS4A6A, HLA-DRB1, PIM2, HLA-DRA, NPC2, LTB, PLP2, HLA-DPB1, ZNF331, CD83, RNASET2, HLA-DMA, SRGN, YPEL5, CTSB, HLA-DPA1, CD37, RPL7, UCP2, NR4A2, HLA-DQB1, LSP1 |
| t cd4 | CD2, CD3D, LTB, IL7R, IL32, CD52, TRAC, TRBC2, CD3E |
| t cd8 | NKG7, CD3D, CCL5, GZMA, TRBC2, CD2, TRAC, CD3G, CD8A, CTSW, LINC01871, HCST, CD3E, CST7, CD52, CD7, IL32, GZMB, PTPRC, CCL4, CORO1A, TRGC2, IL2RG, ALOX5AP, LCK, RGS1, TRBV28, RAC2, KLRD1 |
| t cell cycle | PCLAF, TYMS, CD2, TRBC2, LINC01871, CD3G, NUSAP1, STMN1, CD3D, SMC4, CD7, PTTG1, HMGB2, TOP2A, APOBEC3G, TMPO, CENPM, CENPK, ZWINT, UBE2C, CKS1B, MAD2L1, TIGIT, TK1, LMNB1, SMC2, MKI67, CENPF, SIT1, CDKN3, CLEC2D, CD8A, CDK1, PHF19, PRC1, AURKB, TRGC2, TACC3, KLRC1, CENPU, HELLS, CXCL13, UBE2T, RRM2, ASF1B, H2AC12, LAG3, CTLA4, BIRC5, LINC02195, TUBB, HMGN2, TRAC, RAB27A, PTPN7, GZMB, CORO1A, CENPW, RAC2, CD3E, NKG7, IFNG, AL035456.1, EZH2, GZMA, H2AX, LCK, IL2RB, PCNA, DTYMK, TUBA1B, H2AZ2, CD96, C12orf75, CTSW, PSMB9, CD247, CRIP1, MCM7, HMGB1P5, NUDT1, DUT, ANP32E, TNFRSF18, TBC1D10C, SKA2, DEK, PTPN22, DDX39A, PCED1B-AS1, IL2RG, GNG2, CKLF, CALM3, CBX5, SLA, CCL5, LCP1, BUB3, PSMB8, OXNAD1, DNMT1, CCDC167, ANP32B, TUBBP1, PSIP1, IL32, RPA3, HCST, CYTOR, PTPRC, LSP1, GMFG, SEPTIN1, CD52, ANXA6, RANBP1, HOPX, PAXX, CST7, LBH, ICAM3, ITM2A, IFI16, HLA-F, EVL, ACAP1, ALOX5AP, CKS2, LIMD2, FYN, CBX3, NAP1L4, MZT2A, MT2A, IFI27L2, COTL1, CD53, HCLS1, STK17B, ID2, RGS1, SAMSN1, FXYD5, LAPTM5 |
| t reg | LTB, CD3D, TIGIT, IL32, TNFRSF4, TRAC, CD2, TNFRSF18, TRBC2, SPOCK2, CTLA4, CD27, CD3E, FOXP3, CD7, BATF, IL2RG, TRBC1, IL2RA, CARD16, TBC1D4, CORO1A, LCK, RGS1, IL7R, PTPRC, CD3G, ICOS, RAC2, PCED1B-AS1, CYTOR, CD52 |

**Extended data Table S3:** Annotated clusters with list of significantly defining genes for major clusters defined by scRNAseq

| Cluster ID | Cell count: |
|---|---|
| normal epithelial | 3458 |
| HLA-E-bright tumor | 5461 |
| HLA-E-dim/neg tumor | 9256 |
| endothelial cell | 3135 |
| fibroblast | 7630 |
| pericyte cell | 1963 |
| schwann cell | 186 |
| smooth muscle cell | 660 |
| b cell | 3675 |
| dc1 | 80 |
| dc2 | 599 |
| macrophage | 5271 |
| mast cell | 1015 |
| monocyte | 1871 |
| mreg dc | 150 |
| neutrophil | 519 |
| nk cell | 2580 |
| plasma cell | 1301 |
| plasmacytoid dendritic cell | 171 |
| t cd4 | 8548 |
| t cd8 | 5491 |
| t cell cycle | 629 |
| t reg | 1675 |
| | 65,324 |

**Extended data Table S4:** Annotated scRNAseq clusters with numbers of cells

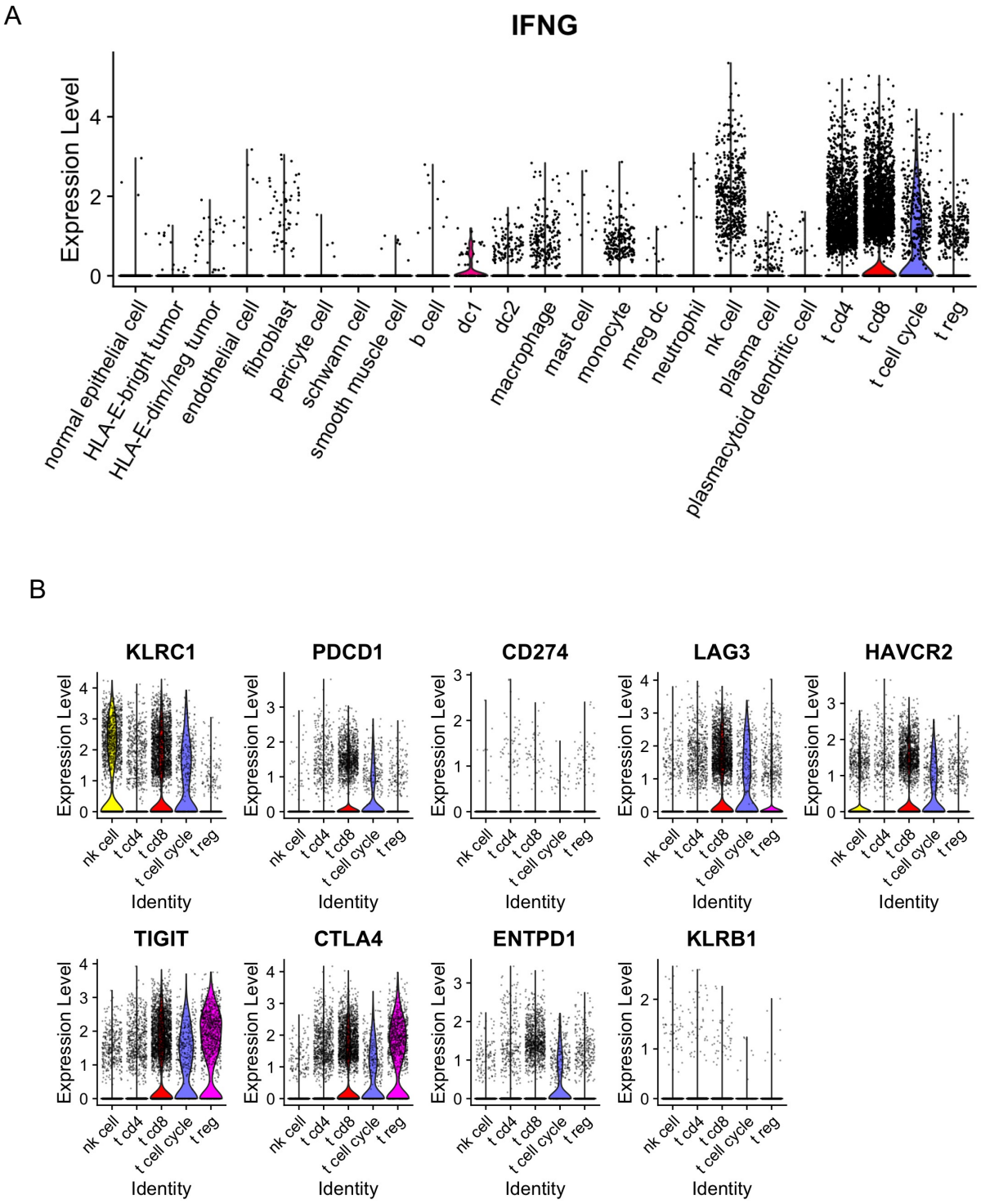


**Extended data Figure S1:** Cellular sources of IFN-γ in NMIBC by scRNAseq

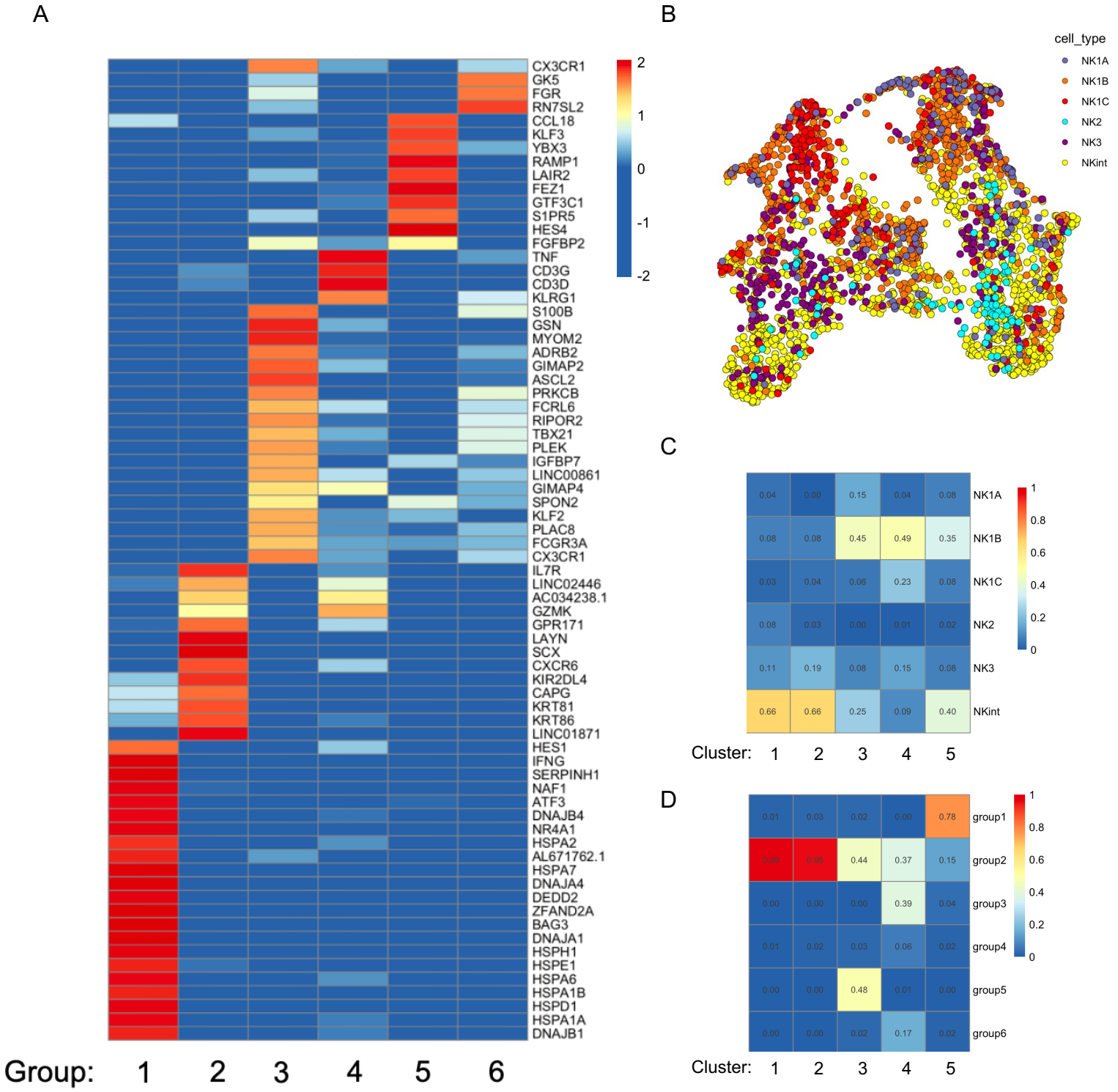


**Extended data Figure S2**

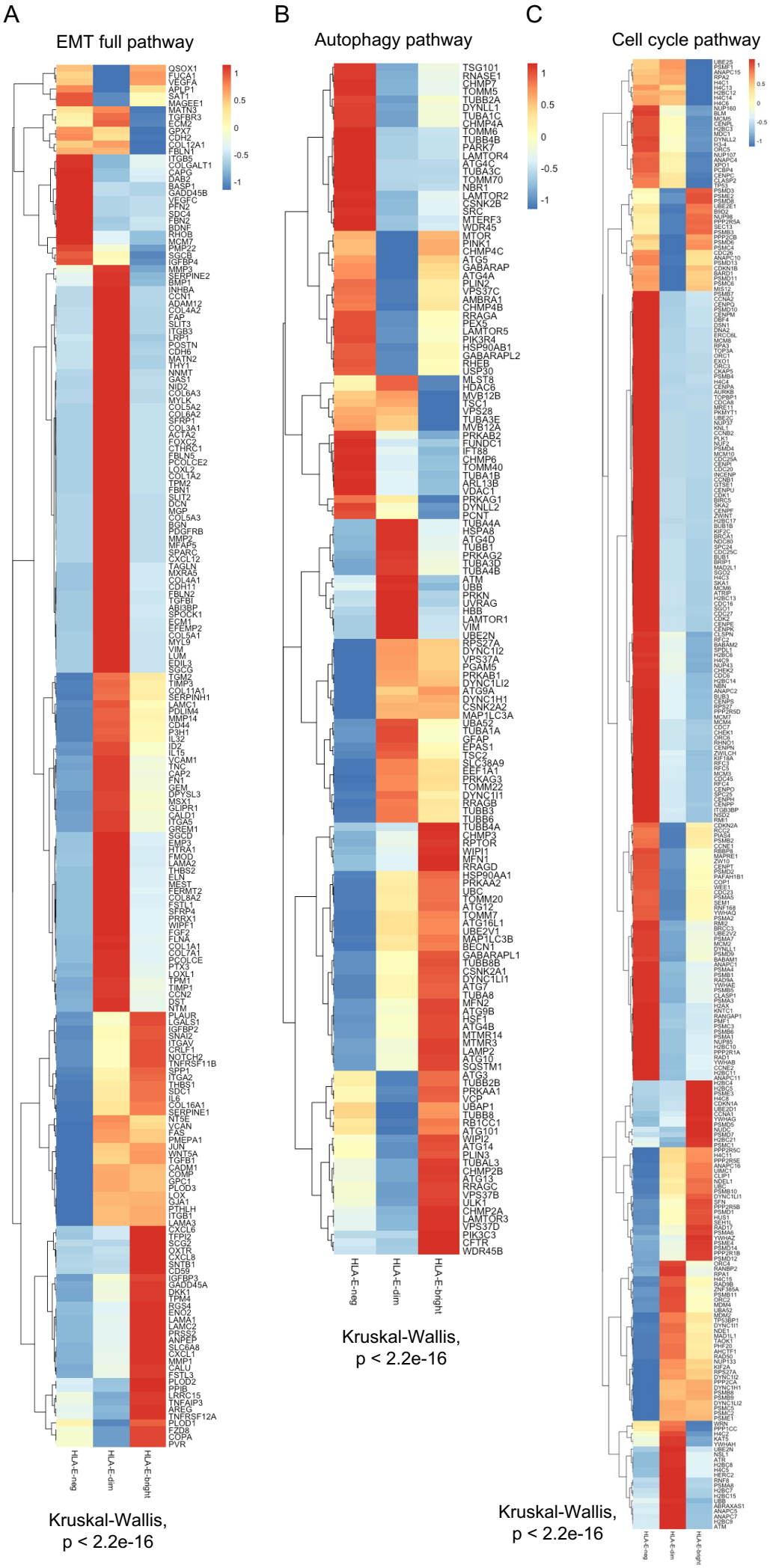


Extended Data Fig. S3

A

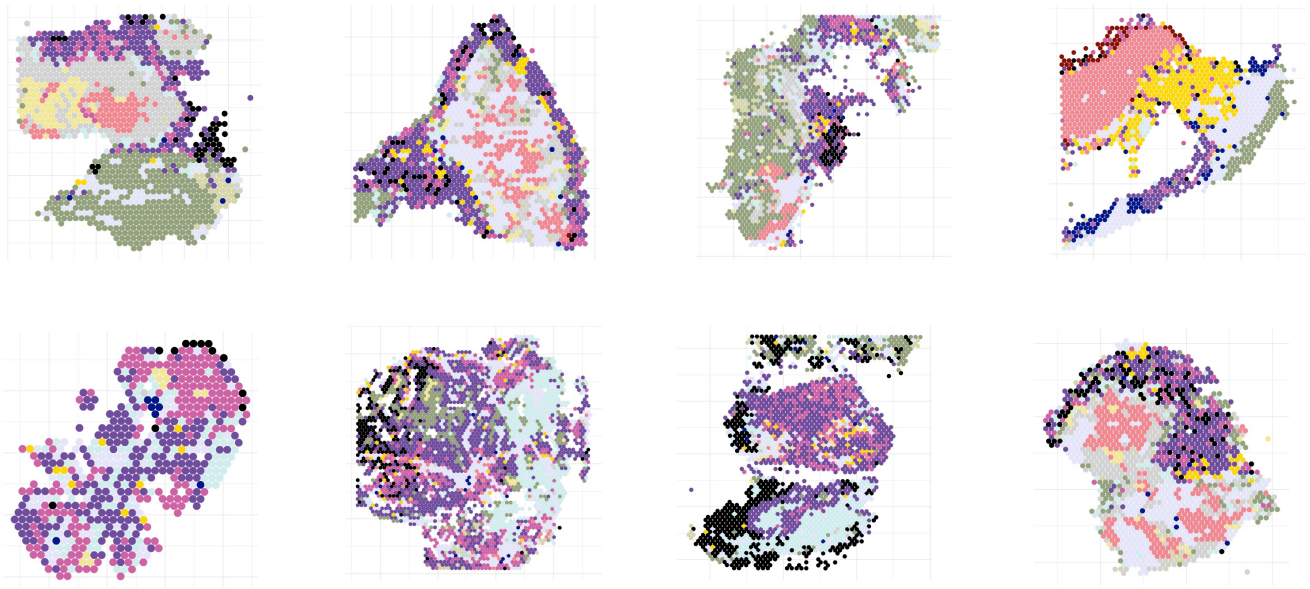

B

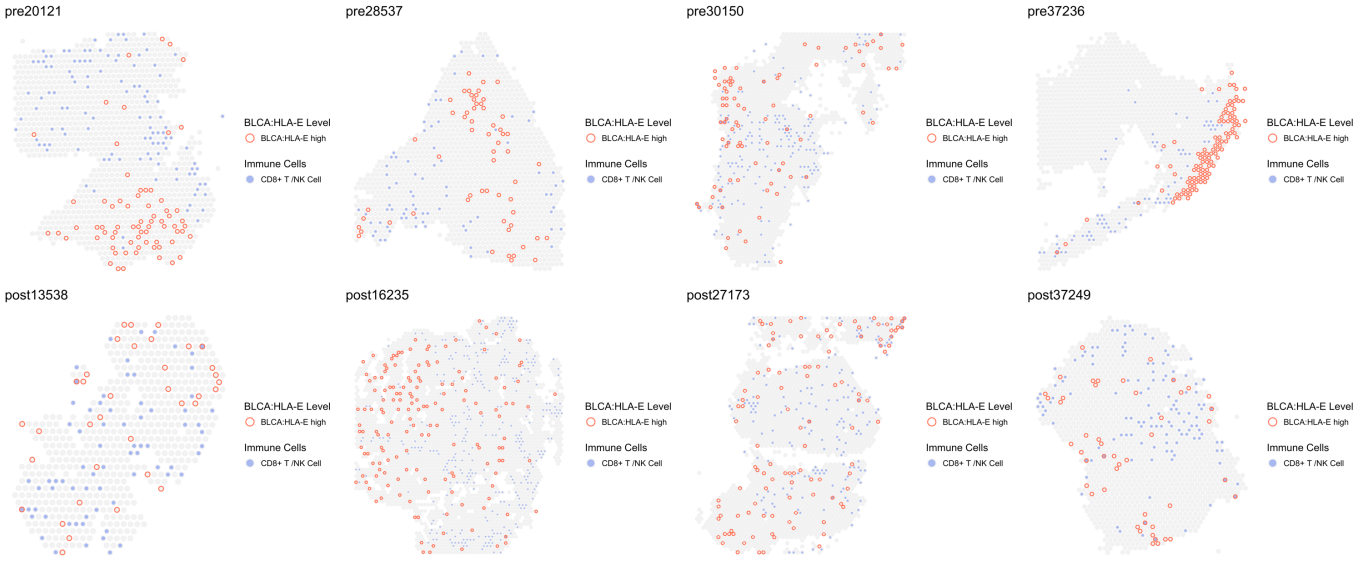


C

Extended Data Fig. S4

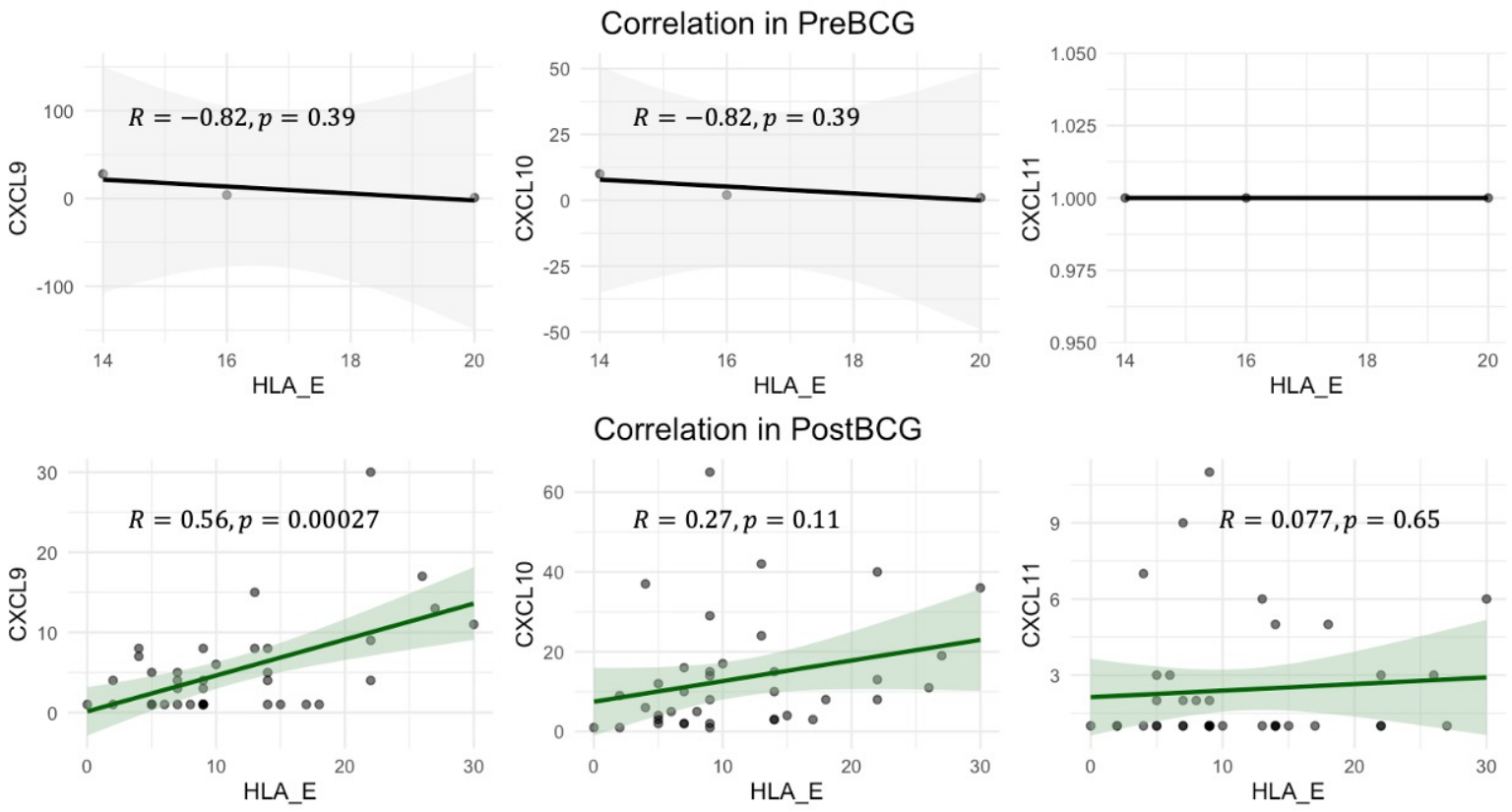


Extended
Data Fig. S5

| | Clinical Cohort Characteristics | | | | |
|---|---|---|---|---|---|
| | HTG | OLINK Urine (Sinai) | Single Cell | Spatial | Cytof |
| n samples, patients | 36, 27 | 42, 26 | 7, 6 | 20, 9 | 16, 16 |
| Female | 4 | 2 | 0 | 0 | 1 |
| BCG Naïve | 19 | 26 | 2 | 4 | 0 |
| BCG Unresponsive | 17 | - | 4 | 5 | 16 |
| Median Age | 64 | 69.5 | 66.9 | 70.6 | 68.5 |
| Median Months to Recurrence | 2.9 | 2.1 | 2.3 | 1.7 | 2.73 |
| Median Months to Progression | 6.7 | - | 14.3 | 23.28 | 4.43 |
| Stage at Collection | | | | | |
| CIS | 4 | - | - | - | - |
| Tis/Ta | 5 | 13 | - | 2 | 8 |
| T1 | 10 | 14 | 4 | 6 | 5 |
| T2 | - | - | - | - | 2 |
| T3 | - | - | 2 | - | 0 |
| T4 | - | - | - | - | 1 |

Table 1.